TIRVolcH: Thermal Infrared Recognition of Volcanic Hotspots. A single band TIR-based algorithm to detect low-to-high thermal anomalies in volcanic regions.

S. Aveni [a,b,*], M. Laiolo [b,c], A. Campus [b], F. Massimetti [b], D. Coppola [b,c]

[a] Department of Civil, Constructional and Environmental Engineering (DICEA), Sapienza University of Rome, Via Eudossiana 18, 00184 Rome, Italy
[b] Department of Earth Sciences, University of Turin, Via Valperga Caluso 35, 10125 Turin, Italy
[c] NATRISK: Centro Interdipartimentale sui Rischi Naturali in Ambiente Montano e Collinare, Università di Torino, Largo Paolo Braccini, 2, 10095 Grugliasco, Italy

ARTICLE INFO

ABSTRACT

Detecting early signs of impending eruptions and monitoring the evolution of volcanic phenomena are fundamental objectives of applied volcanology, both essential for timely assessment of associated hazards. Thermal remote sensing proves to be a cost-effective, yet reliable, information source for these purposes, especially for the hundreds of volcanoes still lacking conventional ground-based monitoring networks. In this work, we present an innovative and effective single band TIR-based (11.45 μm) algorithm (TIRVolcH), capable of detecting thermal anomalies in a broad range of volcanic settings, from low-temperature hydrothermal systems to high-temperature effusive events. Based on the processing of Visible Infrared Imaging Radiometer Suite (VIIRS) scenes, the algorithm offers an unprecedented trade-off between spatial (375 m) and temporal resolution (multiple acquisitions per day), having the potential to detect thermal anomalies for pixel-integrated temperatures as low as 0.5 K above the background, while maintaining a false positive rate of ~1.8 %. The analysis of decadal time series of VIIRS data (2012−2023), acquired at three different volcanoes, reveals how the algorithm can: (i) detect hydrothermal crises at fumarolic fields (Vulcano, Italy), (ii) unveil thermal unrest preceding dome extrusions and explosive eruptions (Agung, Indonesia), and (iii) spatially trace lava flows extent and quantify their advancement rate, as well as track their long-term cooling behaviour (La Palma, Spain).

We envisage that the algorithm will prove instrumental for detecting early signs of volcanic activity and following the evolution of eruptive phenomena, providing a useful tool for hazard management and risk reduction applications. Furthermore, the compilation of statistically robust multidecadal thermal datasets will provide novel insights and new perspectives into volcano monitoring, laying the ground for forthcoming higher-resolution TIR missions.

1. Introduction

Volcanic eruptions and associated or cascading hazards pose a threat to at least 800 million people living within a 100 km radius of one of the ~1400, potentially active, subaerial Holocene volcanoes on Earth (Small and Naumann, 2001, Brown et al., 2015a, Lara et al., 2021). Between 1600 and 2010, more than 270,000 fatalities were associated with volcanic activity (Auker et al., 2013). Furthermore, these events have the potential to cause widespread damage to infrastructures, disrupt global aviation, lead to socio-economic losses, and cause adverse effects on human health (Hansell et al., 2006, Horwell and Baxter, 2006, Gudmundsson, 2011, Brown et al., 2015b, Brown et al. 2015c, Loughlin et al., 2015). Given the transient nature of volcanic phenomena, the capability of detecting, with early notice, variations in the equilibrium of volcanic systems often draws the line between survival and fatality rate (Garcia and Fearnley, 2012, Auker et al., 2013, Poland and Anderson, 2020, Lowenstern and Ramsey, 2017).Even after an eruption begins, the ability to monitor its progression (i.e., identifying active vents, establishing directions and velocities of advancing lava flows, etc.), remains essential for stakeholders and competent bodies to timely review expected scenarios, update hazard maps, and issue exclusion and/or evacuation orders (Ganci et al., 2012a; Harris et al., 2016; Harris et al., 2017; Harris et al., 2019; Coppola et al., 2016a; Coppola et al., 2020; Ganci et al., 2020).

Forefront instruments for detecting early signs of volcanic unrest, as well as advancements in tracking eruptive episodes, play a major role in reducing the risk associated with volcanic events, lowering the overall vulnerability of those exposed to volcanic hazards (Sparks et al., 2012; Donovan et al., 2012). Studies suggested that advancements in volcanology likely saved as many as 50,000 lives in the twentieth century alone (Auker et al., 2013). On the other hand, recent works also revealed that ~50 % of the ~1400 potentially active volcanoes still lack conventional ground-based instruments capable of detecting impending volcanic resurgence (Brown et al., 2015a, Pritchard et al., 2018, Delgado et al., 2019).

In this context, satellite data proves to be a cost-effective, yet reliable, information source for detecting early signs of volcanic activity and monitoring the evolution of eruptive events at remote, poorly monitored, volcanoes. Yet, even at well-monitored volcanoes, remotely sensed data provides a spatiotemporal perspective of eruptive phenomena, mitigating for the gaps in information left by ground-based monitoring networks (Ebmeier et al., 2018; Reath et al., 2019b; Coppola et al., 2020).

Spaceborne data have been employed with a range of techniques to monitor various parameters, encompassing volcanic gas/ash emissions (e.g., Carn et al., 2017; Prata, 2009), deformation (i.e., Pritchard and Simons, 2004a, 2004b; Biggs et al., 2014; Pritchard et al., 2018), and thermal output (i.e., Wright et al., 2015; Wright, 2016; Coppola et al., 2023). Amongst them, the investigation of volcanic phenomena through thermal infrared observations has been a central focus in remote sensing studies for decades, leading to the establishment of a dedicated discipline since the 1960s (Ramsey and Harris, 2013, Harris, 2013, Blackett, 2017).

The progress made in recent decades has allowed the development of the first automatic volcano hotspot-detection systems such as MODVOLC (Wright et al., 2002; Wright et al., 2004) and MIROVA (Coppola et al., 2016b; see Steffke and Harris (2011) for a comprehensive review). These systems, based on the joint availability of Thermal InfraRed (TIR) and Mid-InfraRed (MIR) data acquired by the MODerate resolution Imaging Spectroradiometer (MODIS) mounted aboard Terra (since 1999) and Aqua (since 2002) satellites are still used to detect eruptive activity all over the world, exploiting the high sensitivity of MIR channels to high (i.e., magmatic) temperatures. With a resolution of 1 km and a revisit time of approximately 12 h, MODIS sensors constitute an important volcanic monitoring tool to support volcanological observatories (Coppola et al., 2020).

However, due to the moderate spatial resolution and given that they exploit the different spectral response of the MIR and TIR bands to hot surfaces $\gtrsim$ 600 K (i.e., Normalised Thermal Index (NTI); see Wright et al., 2002 for details), these algorithms are not designed to detect low-temperature ($\lesssim$ 600 K) volcanic phenomena (Zhukov and Oertel, 2001, Briess et al., 2003). Hydrothermal systems, crater lakes, and fumarolic fields, for instance, as well as cooling lava bodies and cooler dome carapaces, are often characterised by temperatures well below the MIR-method-operational threshold (i.e., $\gtrsim$ 600 K) and, as such, the thermal energy sourced by these volcanic features remains undetected and/or unquantified. To track and quantify thermal radiations sourced from these low-temperature volcanic features, scholars employed TIR channels, these better suited to track subtle thermal variations (Reath et al., 2016; Ramsey et al., 2023). Yet, even in a high-temperature domain, TIR observations typically prove more effective in accurately determining the geometrical characteristics of emplaced and advancing lava flows. In fact, the spectral response of MIR channels to hot surfaces is far greater than that of TIR bands, meaning that, even a metrical subpixel hot component lets the overall pixel-integrated temperature rise exponentially (Steffke and Harris, 2011), following a power-law relationship (Wooster et al., 2003). The substantial energy radiated from a relatively small subpixel component causes the thermal signal to spread across several adjacent pixels, following the convolution scheme dictated by the sensor's Point Spread Function (PSF) (Markham, 1985;

Schowengerdt, 2007; Calle et al., 2009; Zakšek et al., 2015a; Zakšek et al., 2015). Blurring artefacts in the hotspot-contaminated MIR scenes imply that even a small lava flow, factually contained within a few pixels, may spread over a considerably larger area, thus significantly affecting the estimation and accuracy of length, width, and shape of the volcanic products (Harris, 1996; Harris, 2013; Harris et al., 2017; Ramsey et al., 2019). On the other hand, TIR acquisitions do retain sensitivity to hot surfaces (Aveni and Blackett, 2022; Verdurme et al., 2022), reducing PSF-related distortions and, in turn, allowing a more detailed interpretation of the eruptive scenario.

In this regard, together with MODIS, the Advanced Spaceborne Thermal Emission and Reflection Radiometer (ASTER), aboard the Terra satellite marked a transformative phase in the thermal remote sensing of volcanic activity. With five TIR (8–12 μm) bands, and a spatial resolution of 90 m ASTER has been instrumental in detecting early (or precursory) signs of volcanic activity (Pieri and Abrams, 2005; Reath et al., 2016), track the evolution of volcanic unrest (Corradino et al., 2023; Pailot-Bonnétat et al., 2023), assess the progression of effusive episodes (Harris et al., 2019; Genzano et al., 2021; Ramsey and Flynn, 2020; Ramsey et al., 2023), quantify the thermal energy sourced by volcanic and hydrothermal targets (Mia et al., 2018; Mannini et al., 2019; Ramsey et al., 2023), locate thermal anomalies in volcanic regions, fumarolic fields, geothermal areas, and hydrothermal systems (Genzano et al., 2021, Taryn et al., 2018, Uchôa et al., 2023, Hellman and Ramsey, 2004, Vaughan et al., 2012a, Vaughan et al., 2020, Chalik et al., 2019, Braddock et al., 2017, Silvestri et al., 2019, Hilman et al., 2020, Caputo et al., 2019, and references therein), and creating comprehensive multidecadal database of volcanic thermal behaviour (Reath et al., 2019a, Urai and Pieri, 2011a, 2011b [https://gbank.gsj.jp/vsidb/image/Agung/volinfo.html]). Previous authors employed TIR bands to monitor low-energy fumarolic fields (Vaughan et al., 2012b; Braddock et al., 2017; Caputo et al., 2019; Reath et al., 2019a; Silvestri et al., 2019; Ramsey and Flynn, 2020; Way et al., 2022), whilst others were successful in quantifying the heat flux sourced by hydrothermal systems (Harris and Stevenson, 1997a, 1997b; Mannini et al., 2019). Furthermore, TIR-based retrospective studies conducted on selected targets revealed early evidence of variations in the thermal activity associated with impending eruptions (e.g., Dehn et al., 2002; Pieri and Abrams, 2005; Reath et al., 2016). These studies revealed how TIR radiation analyses are effective in measuring the heat sourced from volcanic targets. However, despite ASTER's high spatial resolution, its low temporal resolution (1 image every 16 days, at nadir over the equator) poses a major limitation for volcano monitoring. This is further exacerbated by the irregular acquisitions of ASTER scenes over several volcanic targets (Reath et al., 2019b; Ramsey and Flynn, 2020) which makes it quasi-impossible to timely detect potential manifestation of subtle thermal anomalies. Even during eruptive crises, despite the off-nadir pointing capabilities of the instrument and the Urgent Request Protocol (URP) program (see Ramsey, 2016 for details) can be invoked to increase the acquisition frequency up to 1 image every 4 days (depending on target latitude), the revisit time of ASTER impedes a timely assessment of the progression and variations in the eruptive dynamics, especially at volcanoes exhibiting short-living episodes (i.e., Waythomas et al., 2017; Letourneur, 2008; Coppola et al., 2005; Coppola et al., 2021; Bonaccorso and Aloisi, 2021; Marquez et al., 2022; Proietti et al., 2023; Calvari and Nunnari, 2022; Guerrieri et al., 2023; Ganci et al., 2023; Bignami et al., 2020; Werner et al., 2017) or those characterised by persistently unfavourable meteorological conditions where the likelihood of acquiring a cloud-free scene is lowered by more than 65 % (i.e., Mannini et al., 2019, Coppola et al., 2022, Blackett and Wooster, 2011, Reath et al., 2019a, 2019b, Henney, 2012, Carter and Ramsey, 2010, Gray et al., 2019).

The limitations described above have meant that, at present, there is no automatic satellite-based system for detecting low-to-high temperature anomalies using a single approach. To address the numerical challenges related to the automatic or supervised recognition and

detection of anomalous pixels using a single TIR band, previous studies applied in-scene contextual and/or statistical thresholding (Murphy et al., 2011; Blackett, 2014; Rabuffi et al., 2022; Pailot-Bonnétat et al., 2023), long-term change-point detection (Tramutoli, 1998; Tramutoli, 2005; Genzano et al., 2021), combination of image processing and statistical techniques (Ramsey et al., 2023), Machine Learning (ML) approaches (Corradino et al., 2023), and supervised inspection and selection routines (Reath et al., 2019a).

Yet, these studies and/or algorithms were exclusively based on the processing and elaboration of ASTER-like scenes, thus constrained by the temporal availability of these acquisitions. Furthermore, the designated lifetime of TERRA (6 years) has long passed, and its forthcoming disposal must be taken into account (Wright et al., 2015). In this regard and supporting the continuity of satellite-based volcano monitoring, Corradino et al. (2019) and Campus et al. (2022), revealed how the Visible Infrared Imaging Radiometer Suite (VIIRS) sensor aboard Suomi-NPP and NOAA-20 platforms is an excellent candidate to mitigate for the decommissioning of TERRA (and AQUA) platform.

Amongst the comprehensive spectral range embraced by VIIRS sensors, the I-5 band, occupying the TIR portion of the spectrum with the central peak placed at 11.45 μm, is of most interest (Table 1). The intriguing compromise between the spatial (375 m) and temporal resolution (up to 4 acquisitions of the same target per day (in constellation; at the equator)) of this sensor might provide innovative, yet crucial advancements for the systematic monitoring of low-temperature volcanic settings and, in turn, might be key for detecting subtle thermal anomalies associated with early evidence of volcanic unrest.

In this work, we present an innovative and effective single band TIR-based algorithm, devised to elaborate VIIRS scenes to detect volcanogenic thermal anomalies at specific volcanic targets. The algorithm, at its current stage, is conceived to work solely on nighttime acquisitions, to prevent contamination from solar irradiance and reflectance which may affect both the number of alerts and the quality of the retrieved measures (Pieri and Abrams, 2004; Reath et al., 2019a; Pailot-Bonnétat et al., 2023). The algorithm can detect thermally anomalous pixel(s) as low as 0.5 K above the surrounding background pixels, located as far as 25 km from the volcano's summit.

We present the results obtained from the analysis of more than 10 years of data acquired at three different volcanoes (Fig. 1a) that have experienced various types of volcanic activity: (i) Vulcano Island (Italy) which underwent a hydrothermal crisis in 2021–2022 (Fig. 1b), (ii) Mount Agung (Indonesia) that erupted, explosively, on November 21st, 2017 preceded by mid-term thermal precursors (Fig. 1c), and (iii), La Palma (Spain) which produced a large lava flow during the 85-day long effusive eruption begun on September 19th 2021 (Fig. 1d). To determine the reliability of our results, we first conducted a visual selection of the hotspot-contaminated scenes during the whole 10-year period, and then compared the algorithm detections against the supervised outputs. To further validate the results, we performed a cross-correlation against the same parameters obtained from the higher-resolution ASTER scenes and

with independent measures collected via ground-truth instruments. Finally, we demonstrate the benefits of operating a single band TIR based hotspot detection system for volcano monitoring.

2. Case studies

2.1. Vulcano

Vulcano Island, Italy (38.39°N, 14.97°E), is the southernmost emerged volcano of the Aeolian Archipelago (Fig. 1b). The island was formed in the geodynamical context of the Aeolian Arc, originating from the subduction of the African plate underneath the European Plate (Keller, 1980; Ellam et al., 1989). In this subduction regime, the volcanism of Vulcano began ~130 ka (Keller, 1980, De Astis et al., 2013). The last magmatic eruption occurred from 1888 to 1890 (Selva et al., 2020). Following this event, a fumarolic field reaching temperatures up to 700 °C was established within the Gran Cratere area (Fig. 1b; Diliberto, 2017 and Diliberto et al., 2021, Barberi et al., 1991, Capasso et al., 1994, Chiodini et al., 1995). In 1987, after almost a century of low and relatively stable activity, a 6-year-long period of unrest led to a significant increase in the fumarolic activity (Barberi et al., 1991, Chiodini et al., 1996, Montalto, 1996), later followed by minor unrests in 2004–2005, 2009, and 2017 (Granieri et al., 2006, Paonita et al., 2013, Ricci et al., 2015, Selva et al., 2020).

In September 2021, variations in micro-seismicity associated with hydrothermal fluid circulations, ground deformation, increased fumaroles temperatures, and alteration in geochemical composition of ground-exhaling gasses at La Fossa cone (Fig. 1b; Federico et al., 2023), prompted the Italian Department of Civil Protection (DPC) to raise the alert level from green to yellow, effectively announcing the beginning of a new period of unrest (DPC, 2021).
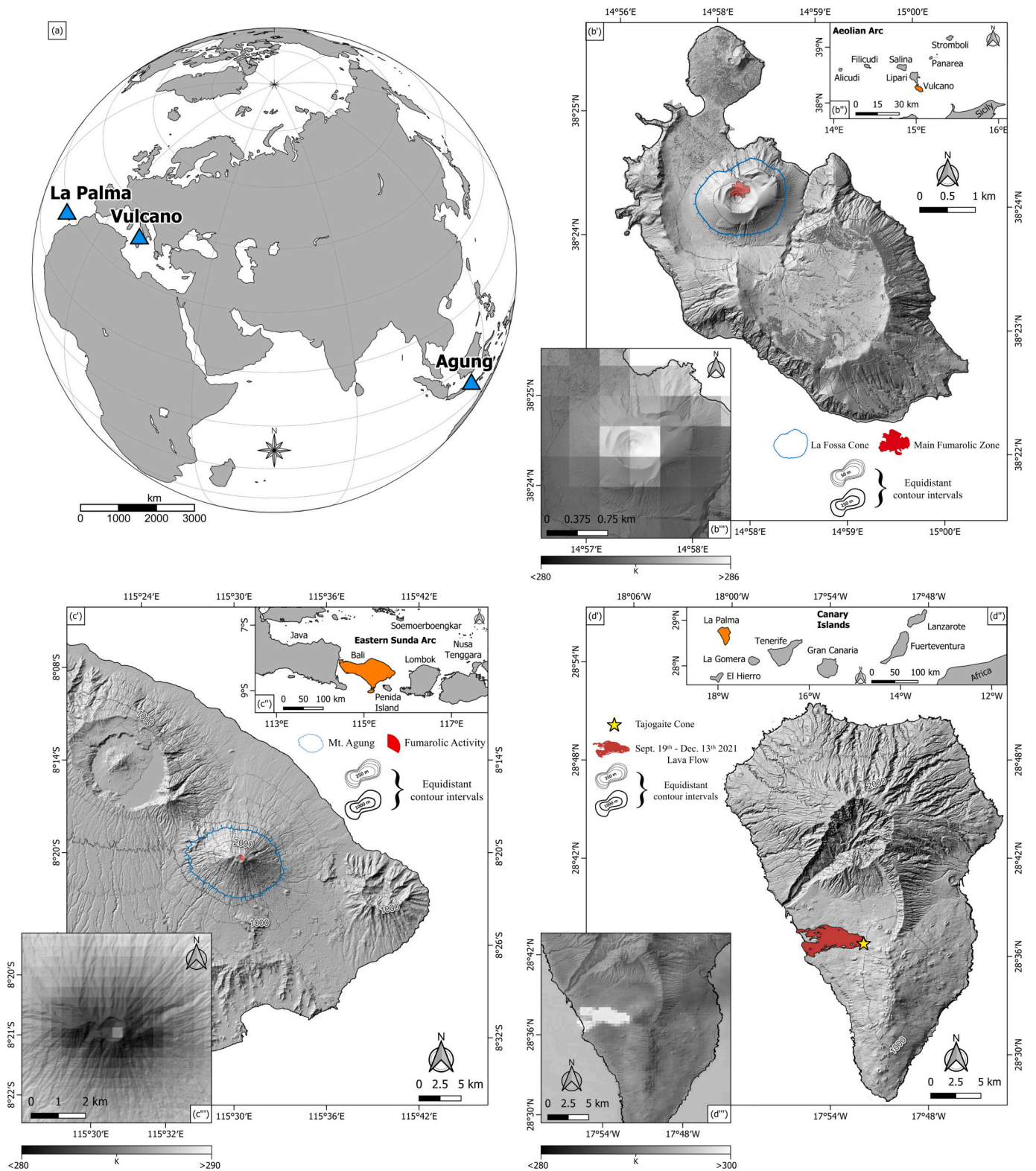
2.2. Mount Agung

Mount Agung, located on the island of Bali, Indonesia (8.34°S, 115.51°E) (Fig. 1c), is considered one of the highest-risk volcanoes in the country (Ardianto et al., 2021). The stratovolcano, located within the Sunda arc, is the superficial manifestation of the geodynamic processes characterising the subduction zone between the Indo-Australian plate and the Sunda block (Syafitri et al., 2022). Extending for 3142 m above sea level, Mt. Agung is renowned for its explosive activity and, given its proximity to populated areas, for the human, social, and economic impact its eruptions have had on the inhabitants of rural villages located along its slopes (Gunawan et al., 2020). According to the Center for Volcanology and Disaster Hazard Mitigation of Indonesia (CVGHM), Mount Agung has erupted four times in the last two centuries: in 1808, 1821, 1843, and 1963 (Gunawan et al., 2020). The 1963 – VEI 5 – eruption claimed 1148 lives and injured 296 people (Zen and Hadikusumo, 1964). The elevated death toll was mainly related to far-reaching (10 to 14 km) pyroclastic flows, ejection of large ballistics up to ~6.5 km from the summit, and ensuing lahars (Kusumadinata, 1964; Surjo, 1965; Self and Rampino, 2012).

After a 53-year interval of dormancy, the volcano underwent an eruptive phase between November 21, 2017, and June 13, 2019, reinvigorating the scientific focus on the Indonesian volcano (Andaru et al., 2021). The most recent eruptive phase could have been anticipated based on significant ground deformation, occurrence of seismic swarms, and increasing intra-crater thermal activity since 2017 (Ardianto et al., 2021, Gunawan et al., 2020, Syahbana et al., 2019, Bemelmans et al., 2023).

2.3. La Palma

La Palma, Canary Islands, Spain (28.71°N, 17.91°W) (Fig. 1d), is one of the most active volcanoes of the intraplate hot-spot archipelago (Romero et al., 2022; Montesinos et al., 2013). Subsurface volcanism at

Table 1

Main characteristics of VIIRS sensors. [1]Cao et al. (2014), [2]Cao et al. (2013b), [3]Schroeder and Giglio (2017), [4]Oudrari et al. (2016).

	VIIRS (S-NPP/N20) / VIIRS (S-NPP/N20)
Orbit altitude (km)	824
Swath (km)	3060
Equator crossing time	12:40 LT / 13:30 LT
Pixel resolution at nadir (km)	0.375
Pixel resolution at the edge (km)	0.75
ID TIR Band	I-5
Spectral range (μm)	10.560–12.428 [1]
Central Wavelength (μm)	11.45
T Min (K)	~ 205 [2]
T Max (K)	~ 380 [2]
NEΔT (K) @ 210	~ 0.40 [3]
NEΔT (K) @ 267	~ 0.05 [4]

(caption on next page)

Fig. 1. a) Orthographic World projection (M_Map package; Pawlowicz, 2020) showing the location of the three studied volcanoes. **b')** Digital Surface Model (DSM) of Vulcano Island at 1 m spatial resolution, adopted from Ministero dell'Ambiente e della Tutela del Territorio e del Mare (MATTM under Creative Commons License CC-BY-SA 3.0 IT). The red shape depicts the Main Fumarolic Zone (MFZ) as described by Mannini et al. (2019). The blue line approximates the perimeter of La Fossa cone. Bold and regular black lines represent equidistant contour intervals at 250 m and 50 m, respectively. **b'')** Location map of Vulcano island and the Aeolian Arc. **b''')** VIIRS I5 band at 375 m resolution acquired on May 8th, 2014, at 00:48 (UTC), superimposed the DSM and centred over Gran Cratere area. **c')** Digital Elevation Model (DEM; Demnas) of Bali island at ~8.25 m spatial resolution, adopted from the Geospatial Information Agency (Badan Informasi Geospasial—BIG). Available from: https://tanahair.indonesia.go.id/demnas/#/ (Accessed July 4th, 2022). The red shape depicts the fumarolic and solfataric zone as inferred from (Syahbana et al., 2019; Andaru and Rau, 2019; Bemelmans et al., 2023). The blue line approximates the perimeter of the main volcanic edifice. Bold and regular black lines represent equidistant contour intervals at 1000 m and 250 m, respectively. **c'')** Location map of Bali Island and the central portion of the Indonesian archipelago. **c''')** VIIRS I5 band at 375 m resolution acquired on May 19th, 2016, at 17:36 (UTC) superimposed the DEM, centred over Mount Agung. **d')** Digital Terrain Model (DTM) of La Palma island at 2 m spatial resolution, adopted from the Autonomous body National Center for Geographic Information (CNIG) under Creative Commons License CC-BY 4.0 (Accessed January 31st, 2023). Available from: https://centrodedescargas.cnig.es/CentroDescargas/busquedaSerie.do?codSerie=MDT02. Bold and regular black lines represent equidistant contour intervals at 1000 m and 250 m, respectively. The yellow star depicts the location of the Tajogaite cone. The red shape demarks the extent of the lava flow (September 19th-December 13th, 2021) as provided by Copernicus Emergency Management Service (2024). Available from: https://emergency.copernicus.eu/mapping/ems-product-component/EMSR546_AOI01_GRA_MONIT63_r1_VECTORS/1 (Accessed January 31st, 2023). **d'')** Location map of La Palma Island and the Canarian archipelago. **d''')** VIIRS I5 band at 375 m resolution acquired on October 17th, 2021, at 02:48 (UTC) superimposed the DTM and centred over the Cumbre Vieja ridge. (For interpretation of the references to colour in this figure legend, the reader is referred to the web version of this article.)

La Palma started ~4–3 Ma ago (Carracedo et al., 2001). In the last 125 ka activity was mainly located in the southern part of the emerged island, known as the Cumbre Vieja volcanic complex (Cabrera-Pérez et al., 2023). In the last ~500 years, at least 6 eruptions took place within the Cumbre Vieja ridge, in 1585, 1646, 1677–1678, 1712, 1949, and 1971 (Guillou et al., 1998; Carracedo et al., 1998; Klügel et al., 2000; Carracedo et al., 2001; Casillas Ruiz et al., 2020).

On September 19th, 2021, after a 2-year long period of unrest characterised by seismic swarms, geochemical anomalies, and ground inflation (e.g., Torres-González et al., 2020, Padrón et al., 2021, Carracedo et al., 2022, Civico et al., 2022, D'Auria et al., 2022, Pankhurst et al., 2022), a new eruption began. The event was characterised by the simultaneous emission of lava flows and tephra plumes from multiple vents located along a NW-SE-orientated fissure (Bonadonna et al., 2022; Birnbaum et al., 2023). After 85 days of fluctuating activity, the eruption was officially announced to have ended on December 13th, 2021 (Plank et al., 2023). Subaerial lava flows covered an area of ~11.8 km^2, affected a total of 3126 buildings (of which 2800 were eventually destroyed), and led to the evacuation of ~7500 inhabitants (JRC, 2021; Amonte et al., 2022; Civico et al., 2022). The effused lava volume was estimated to be 177.6 ± 5.8 Mm^3, with a Mean Output Rate (MOR) of ~24.1 m^3/s, and a maximum and average lava flow thickness of 65 m and 15.2 m, respectively (Civico et al., 2022; Bonadonna et al., 2022; Plank et al., 2023).

3. VIIRS sensor and input data

3.1. Visible Infrared Imaging Radiometer Suite (VIIRS) sensors

The Suomi National Polar-Orbiting Partnership (SNPP) and the Joint Polar Satellite System's (JPSS) JPSS-1 (NOAA-20 or N20) have been in orbit since October 2011 and November 2017, respectively (Goldberg, 2018; Xiong et al., 2018). Both Suomi-NPP and JPSS-1 satellites are placed in a polar orbit at a nominal altitude of 824 km (Cao et al., 2017). Boasting a cross-track field-of-view (FOV) of 112.56°, and a swath width of 3060 km, each VIIRS sensor provides full coverage of the globe daily (Cao et al., 2013a). The sensors gather information across 22 spectral bands, encompassing the electromagnetic spectrum from 0.412 μm to 12.01 μm. This includes 16 moderate-resolution bands (M-bands), a panchromatic Day-Night Band (DNB) characterised by a spatial resolution of 750 m, and 5 imaging resolution bands (I-bands) with a spatial resolution of 375 m. Amongst the comprehensive spectral range of VIIRS instruments, the I-5 TIR band centred at 11.45 μm (Table 1), is the one used in this work to detect thermal anomalies of volcanic origin.

3.2. Input data

The proposed algorithm is currently based on VIIRS I-5 nighttime scenes elaborated by the MIROVA system (Campus et al., 2022). The datasets are made of daily acquisitions from both Suomi-NPP and NOAA-20 VIIRS Level 1B radiances (VNP02IMG and VJ102IMG 6-Min L1B Swath 375 m, respectively; atmospherically uncorrected) and associated geolocation data products (VNP03IMG and VJ103IMG Imagery Resolution Terrain-Corrected Geolocation 6-Min L1 Swath 375 m, respectively), covering a period of more than 10 years (since January 2012). These are freely distributed by NASA's Level-1 and Atmosphere Archive & Distribution System–Distributed Active Archive Center (LAADS-DAAC) in netCDF4/HDF5 format. The original granules, as per MIROVA workflow, are resampled to a regular 134 × 134 UTM grid centred on the volcano summit according to the coordinates provided by the Global Volcanism Program (2023). This step ensures consistency across all the scenes that now cover an area of ~2500 km^2. Once the scenes are processed, these are stored in a local database, together with information regarding date and acquisition time, zenith angle, geolocation information, etc., thus ready for further processing (see Coppola et al., 2016b for details).

4. TIRVolcH algorithm

4.1. Overview

When satellite scenes of the same region are stacked together, at-pixel resolution long-term statistics can be obtained and, in turn, anomalous variations from the long-term behaviour can be detected both in time and space (Tramutoli, 1998). To embrace both conditions, this algorithm combines spatial and temporal checks to determine the occurrence of anomalous pixels within the scene.

In the following paragraphs, the different steps of the algorithm will be detailed. These are (i) initialisation, where the ancillary data and the pre-processing phase necessary for identifying hotspot-contaminated pixels (i.e., *Confirmed Alerts*) are created, (ii) hotspot detection, detailing the distinction between *land-* and *water-dominated* scenes, together with the higher sensitivity statistics applied to high-interest volcano-specific features (i.e., VS_{ROI}) and (iii), outputs, where the volcanologically relevant parameters are retrieved. The whole process is scripted in a MATLAB environment, following the workflow summarised in Fig. 2.

4.2. Step 1 – Initialization

4.2.1. Ancillary data

To identify hotspot candidate pixels (i.e., *Candidate Alerts*) and minimise the number of false alerts the hotspot detection phase requires
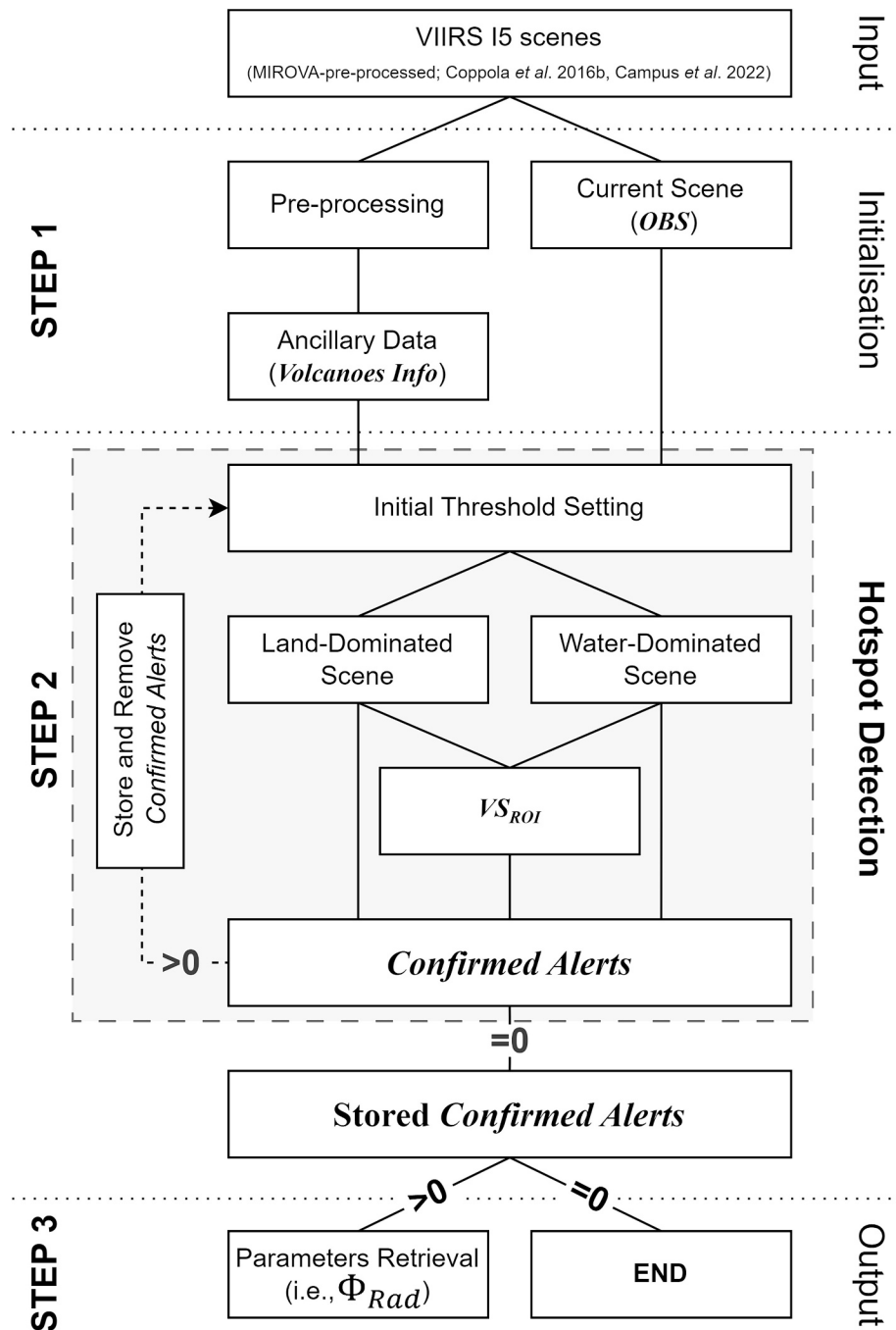
Fig. 2. Workflow of TIRVolcH. The top panel shows input data, followed by (**Step 1**) Initialisation, (**Step 2**) Hotspot Detection, and (**Step 3**) Outputs (i.e., parameters retrieval). Note, the dashed and grey shaded box in **Step 2** indicates iteration of the loop (dashed arrow) until no (further) Candidate Alerts are detected (see text for details). (For interpretation of the references to color in this figure legend, the reader is referred to the web version of this article.)

some ancillary parameters that must be provided before running the whole workflow. These parameters, stored in a structure named *Volcanoes Info*, are:

- *Coordinates of Interest*: the revised location of the volcano's summit (or active vent) to compensate for any offset in the GVP list (Latitude and Longitude coordinates, in degrees; GVP, 2023). These corrections, where needed, ensure that coordinates are representative of the active vents and/or thermal target locations, where higher sensitivity statistics are applied (see Section 4.3).
- *Land/Water Mask* (*LW Mask*): Land/Water mask of the region (binary matrix 134×134 pixels) as provided with L1B VIIRS products.

- *Monthly Reference Scenes* (*REF*): mostly cloud-free scenes of the investigated region (one per each month of the year; 12 REF per volcano), representing the average temperature conditions of the area. These scenes are compared against the observed ones (i.e., satellite acquisitions) to detect variations from the normal behaviour (see Section 4.2.2 and 4.3).
- *Regions of Interest* (*ROIs*): Four regions are defined as ROI_1, extending for ~1 km from the volcano's summit, ROI_2, from ~1 to ~5 km, ROI_3, from ~5 to ~12.5 km, and ROI_4, beyond 12.5 km.
- *Volcano-Specific Region of Interest* (*VS_{ROI}*): an ad hoc mask within which higher sensitivity statistics are applied for volcanoes

exhibiting persistent activity such as crater lakes, fumarolic fields, etc. (x,y coordinates; see Section 4.3.4).

- *Volcano-specific exclusion Region of Interest (VS_{ExcROI})*: to reduce the number of false alerts (binary matrix 134×134 pixels); This, similarly to the data-removal mask previously applied by Tramutoli (1998), is generated for each volcano based on the type of volcanism and on the distance from the summit reached by lava flows and/or magmatic products within the last 2 decades. This is established by evaluating the volcano's long-term behaviour observed by the MIROVA system together with ground-based volcanological observations outlined in bulletins issued by volcanic observatories and available literature. With that in mind, VS_{ExcROI} are generated following the conditions outlined below:

(i) For targets featuring quasi-exclusively confined activity (i.e., crater lakes, lava lakes, fumarolic fields, etc.), anomalous pixels are searched within a 2 km radius from the summit area;
(ii) For targets featuring effusive and/or explosive episodes confined within the summit area, anomalous pixels are searched within a 5 km radius from the volcano's summit;
(iii) For targets featuring far-reaching lava flows (> 5 km) or for those where no thermal activity was detected in the past two decades, no spatial restrictions apply.

It must be noted that a VS_{ExcROI}, where needed, can be promptly resized to accommodate the ongoing eruptive dynamics.

4.2.2. Pre-processing and generation of monthly reference scenes (REF)

The pre-processing phase enables retrieval of monthly reference matrices (REF), these representing the average, monthly-based, Brightness Temperature (BT) for each investigated region. The first time a new target is processed, the initial step consists of extracting and stacking together all VIIRS nighttime TIR acquisitions for the designated volcano from the MIROVA database. The resampled I-5 radiance scenes (134×134 pixels) are converted into BT and then stored in a single cubic matrix (Fig. 3a), accompanied by temporal and spatial information. A first reference image is then generated by averaging all the stacked scenes, to obtain a time-averaged BT matrix of the investigated region (Fig. 3b). Notably this reference image, although obtained by averaging several images contaminated by clouds, has the property of maintaining the texture and pattern of the cloud-free scene and can be used as a first, temporary reference matrix. Hence, each scene is compared against this reference image and a coefficient of determination (R^2) is computed. This coefficient is empirically assumed to be a proxy of the cloud fraction, since the mostly cloud-free images show high R^2 values, while poor correlation is found for cloudy scenes (Fig. 3c). Images with an R^2 coefficient < 0.5 are discarded and a new reference scene, containing mostly cloud-free acquisitions, is generated following the stacking approach discussed above. The process is repeated a second time to further reduce the number of unsuitable scenes in the stacked compilation. The remaining acquisitions are divided into months (Fig. 3d) and the BT time series of each pixel is retrieved. Datapoints (pixels) exceeding three scaled Median Absolute Deviation (MAD) from the monthly median BT (i.e., outliers; Leys et al., 2013) are removed from the matrix and replaced by interpolating the remaining values along the third dimension (Fig. 3e). This step ensures that most of the remaining, if any, sparse clouds, wildfires, or anomalous pixels are removed. The final reference package includes a cubic matrix of 12 scenes, one per every month of the year (REF; Fig. 3f), and it is stored locally, ready to be used when recalled within the hotspot detection step described below.

For volcanoes characterised by persistent activity, such as those related to fumarolic activity (i.e., Mt. Agung or Vulcano) or crater lakes, the construction of monthly reference matrices requires a further step. For these targets, the hotspot-contaminated pixels are visually identified and removed from the matrix; the gaps are filled by assigning the BT value of the surrounding, non-thermally anomalous pixels, using a bi-cubic interpolation (Fig. 4).

4.3. Step 2 – Hotspot detection

Within this step, each observed image (OBS, in K) is compared against its associated reference scene (REF, in K), to detect the presence of hotspots-contaminated pixels (*Confirmed Alerts*). This is made through a series of tests to identify potentially hotspots-contaminated pixels (*Candidate Alerts*). The same approach is employed to detect cloud-contaminated pixels (*Cloud Pixels*). After the initial set of tests (*Initial thresholding setting*; see Section 4.3.1) the algorithm splits the processing into two separate workflows, one for *Land-dominated scenes* and one for *Water-dominated scenes*. The algorithm checks the percentage of land in the scene using the information contained in the LW Mask file (see Section 4.2.1). Scenes containing more than 20 % of land pixels (~500 km^2) are flagged as '*Land-dominated*', whilst those showing less than 20 % are flagged as '*Water-dominated*. This main distinction is necessary because of the very different temperature distribution in the two settings. In particular, while in *Land-dominated* contexts the algorithm exploits clustering analysis of the heterogeneous temperature distribution within the investigated region, this is not possible in *Water-dominated* scenes, as water surfaces are mainly characterised by a homogenous temperature distribution. Furthermore, at volcanoes exhibiting persistent, yet subtle, thermal activity confined within a well-defined area such as fumarolic fields or crater lakes, the algorithm employs a volcano-specific ROI (VS_{ROI}). These features are characterised by considerably lower temperatures as compared to those of magmatic bodies, so that clustering or thresholding approaches usually fail to detect these subtle volcanic features.

4.3.1. Initial thresholds setting

In this initial step, *OBS* is analysed and pixels exceeding a fixed threshold (ABS_{BT}) are considered *Candidate Alerts*:

$$OBS \geq ABS_{BT} \qquad \text{[test 1]}$$

where ABS_{BT} is equal to 313.15 K, this being consistent with the maximum nighttime temperature recorded on Earth, not contaminated by a hotspot (NOAA, 2024).

Then, a scene of residues (RES, in K; Fig. 5c,f,i) is computed by subtracting the monthly REF scene (Fig. 5a,d,g) from the BT of the observed image (Fig. 5b,e,h), so that:

$$RES = OBS - REF \qquad (1)$$

The 99.5 percentile of RES ($pRES_{99.5}$) is used to label *Candidate Alerts* and *Cloud Pixels* according to test 2 and test 3, respectively:

$$RES > ABS_{DT} \qquad \text{[test 2]}$$

$$RES < ABS_{CL} \qquad \text{[test 3]}$$

where ABS_{DT} and ABS_{CL} result from the following conditions:

$$\text{if } pRES_{99.5} > 10 \text{ then } \begin{cases} ABS_{DT} = 20 \\ ABS_{CL} = 0 \end{cases}, else$$

$$\text{if } 5 < pRES_{99.5} < 10 \text{ then } \begin{cases} ABS_{DT} = 15 \\ ABS_{CL} = -5 \end{cases}, else$$

$$\text{if } pRES_{99.5} < 5 \text{ then } \begin{cases} ABS_{DT} = 10 \\ ABS_{CL} = -10 \end{cases}$$

Once tests 1, 2, and 3 are executed, the *Cloud Pixels* are removed from *RES* and, a *Z-Score matrix* ($Z - RES$) is computed as:
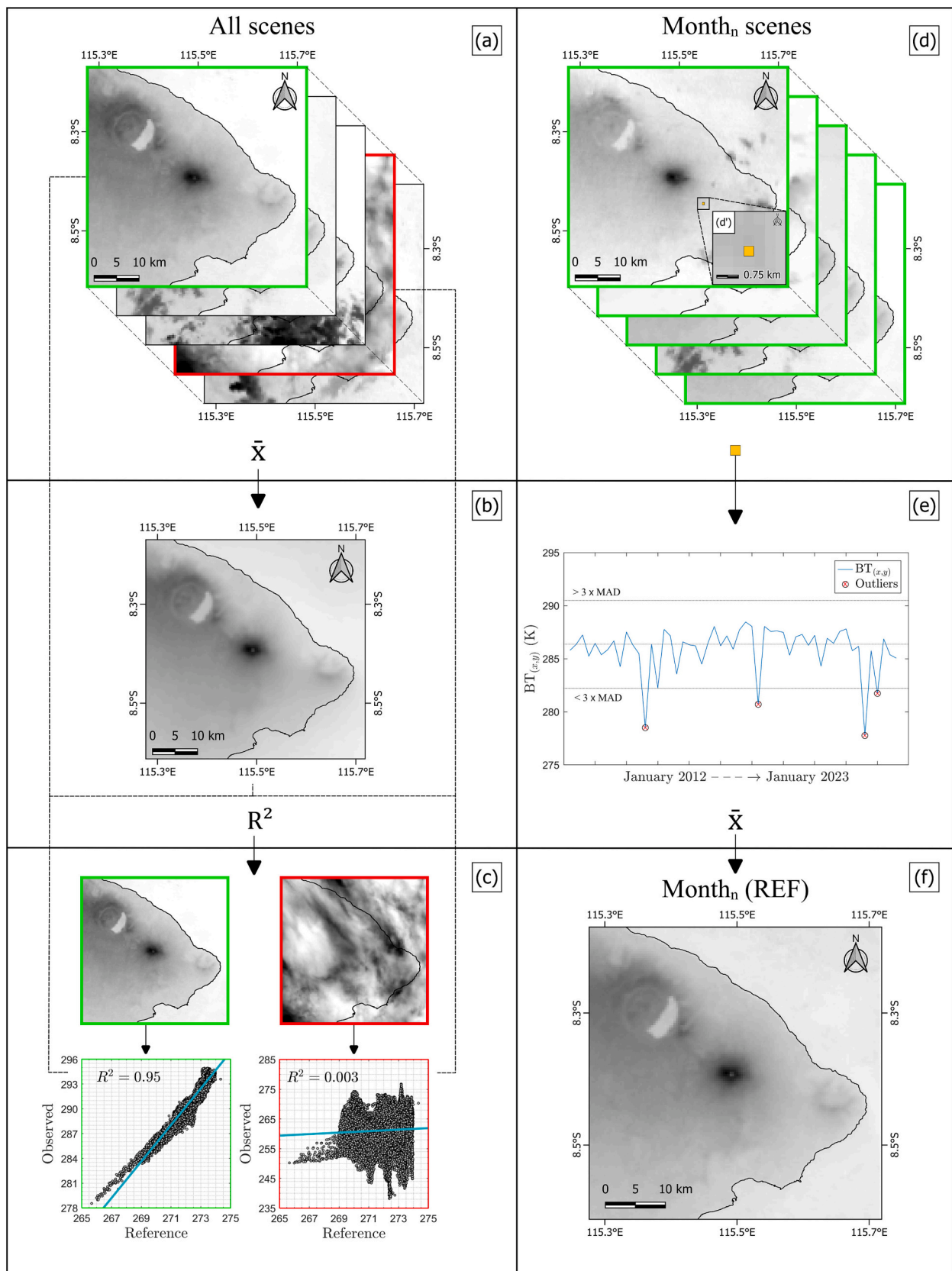
Fig. 3. Workflow for generating REF matrices (Mount Agung example). **a)** All scenes stacking **b)** Temporary REF scene **c)** Scatter plot showing the typical relationship between cloud-free and cloud-contaminated scenes. Note that scenes with $R^2 < 0.5$ are discarded. **d)** Monthly division (only scenes with $R^2 > 0.5$). **e)** Pixel-by-pixel outlier removal in monthly REF matrices. **f)** REF output. See text for details. (For interpretation of the references to colour in this figure legend, the reader is referred to the web version of this article.)
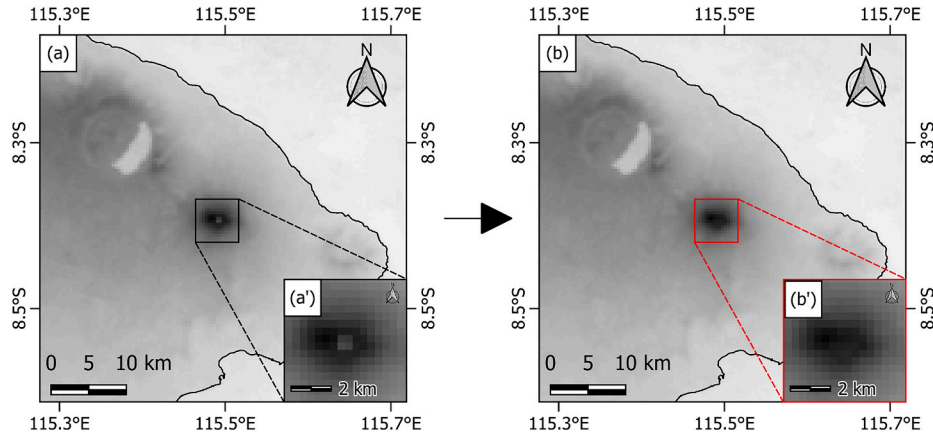
Fig. 4. Mount Agung. **a)** REF scene as resulting from Fig. 3f. Note how a thermal anomaly persists within Agung's crater (**a'**). **b)** REF scene with the persistent thermal anomaly visually identified and removed (**b'**). (For interpretation of the references to colour in this figure legend, the reader is referred to the web version of this article.)

$$Z - RES = \frac{RES - \overline{RES}}{\sigma_{RES}} \tag{2}$$

where $\overline{RES}$ and σ_{RES} are the mean and the standard deviation of RES, respectively. Accordingly, pixels not detected by previous test but satisfying test 4 are added to the *Candidate Alerts*:

$$Z - RES > 7 \tag{test 4}$$

4.3.2. Hotspot detection for Land-dominated scenes

Within the hotspot detection for *Land-dominated scenes*, two distinct blocks are executed. The first operates on a cartesian domain by investigating the temperature distribution in a scatter plot to identify anomalous (i.e., outliers) pixels (i.e., datapoints). The second block works on the images anew, performing contextual statistics on the scenes.

First Block: On the assumption that an approximately linear relationship exists between clear sky and hotspot-free OBS and REF, if we plot these two variables in a scatter plot, most of the data should lie around the 1:1 ratio. In contrast, scattered and low-density data points (i.e., outliers) located above the main cluster should represent hot anomalies (i.e., volcanic surfaces). Datapoints representing clearly contaminated pixels are usually comprised between the ~0.005 % and the ~1 % of the whole scene (i.e., 1 to 200 pixels or ~ 0.1 to ~30 km^2) and significantly deviate from the main cluster of uncontaminated data. This implies that their density distribution is much lower than pixels representing average conditions.

At first, REF and OBS matrices are reshaped into vectors and are plotted on a scatterplot in the x and y axis, respectively (Fig. 6). Any pixel(s) previously flagged as *Candidate Alerts* or *Cloud Pixels* are removed. Then, for each pair of data (x, y) in the scatterplot, the Euclidean Distance (ED_{xy}) with respect to the eight smallest distances (i. e., the eight nearest datapoints in the plot with respect to the examined x, y pair) is calculated as:

$$ED_{xy} = \sqrt{\left(OBS_x - REF_x\right)^2 + \left(OBS_y - REF_y\right)^2} \tag{3}$$

The choice of selecting eight neighbouring datapoints was made to resemble the in-scene conditions, namely the number of pixels surrounding any given pixel. Datapoints with $ED_{xy} < 1$ are considered part of the Main Cluster (MC; non-anomalous data), and a polygon, hereafter named $Poly_{ED}$, is automatically drawn around them (Fig. 6). At this point, four concentric envelopes ($Poly_{ROIn}$) are drawn around $Poly_{ED}$ by adding a ROI-dependent buffer (bΔT$_{ROIn}$) so that:

$$Poly_{ROIn} = Poly_{ED} + b\Delta T_{ROIn} \tag{4}$$

with bΔT$_{ROIn}$ equal to 0.5, 1, 2 and 4 K for ROI$_1$, ROI$_2$, ROI$_3$, and ROI$_4$, respectively (Fig. 6).

Any datapoint in the scatterplot is also associated with its specific ROI_n in the spatial domain (matrix; see Fig. 7a,b,c). Hence, any datapoint $(x, y)_{ROIn}$ in the scatterplot (or its corresponding pixel in the matrix), is considered a *Candidate Alert* if the following condition is satisfied:

$$(x, y)_{ROIn} \notin Poly_{ROIn} \tag{test 5}$$

where $(x, y)_{ROIn}$ is a datapoint of a specific ROI and $Poly_{ROIn}$ is the associated envelope. Graphically this test is used to identify the data points located outside the polygon defined for each ROI ($Poly_{ROIn}$).

Second Block: This block operates on the spatial domain (matrix) anew, to detect remaining, or missed anomalous pixels within ROI$_1$. This test increases the capability to detect subtle thermal anomalies within ROI$_1$, the region where there is the highest likelihood of encountering volcanogenic anomalies. To do this, after temporarily removing any detected *Candidate Alert* resulting from all previous tests (Test 1 to 5), the mean and standard deviation of the non-alerted pixels within ROI$_1$ are computed both for the OBS ($\overline{OBS_{ROI1}}$ and σOBS_{ROI1}, respectively) and for the RES images ($\overline{RES_{ROI1}}$ and σRES_{ROI1}, respectively). Pixels of OBS_{ROI1} satisfying the following test are flagged as *Candidate Alerts*:

$$OBS_{ROI1} \geq \overline{OBS_{ROI1}} + 3\sigma OBS_{ROI1} \ \& \ OBS_{ROI1} \geq \overline{RES_{ROI1}} + 3\sigma RES_{ROI1} \tag{test 6}$$

The *Candidate Alerts* are therefore those that have passed at least one of the tests 1 to 6.

4.3.3. Hotspot detection for Water-dominated scenes

Over *Water-dominated* scenes the normal temperature distribution implies that clustering approach described above (Section 4.3.2) fails because of the homogeneous temperature distribution over sea and/or water bodies. Hence, we only apply a contextual approach based on the statistical analysis of the investigated region. The average temperature ($\overline{OBS}$) of the observed scene and its standard deviation (σOBS) are computed and the following test is performed to detect new *Candidate Alerts*:

$$OBS \geq \overline{OBS} + 10\sigma OBS \ or \ OBS \geq pOBS_{99.5} \tag{test 7}$$

where $pOBS_{99.5}$ is the 99.95th percentile of the whole scene.

Candidate Alerts are removed from the scene, and a new ROI (ROI_{Island}) of ~2 km centred on the volcano's summit is defined. Hence, the mean ($\overline{OBS_{ROI_{Island}}}$) and standard deviation ($\sigma OBS_{ROI_{Island}}$) of ROI_{Island} are computed to perform the last test:
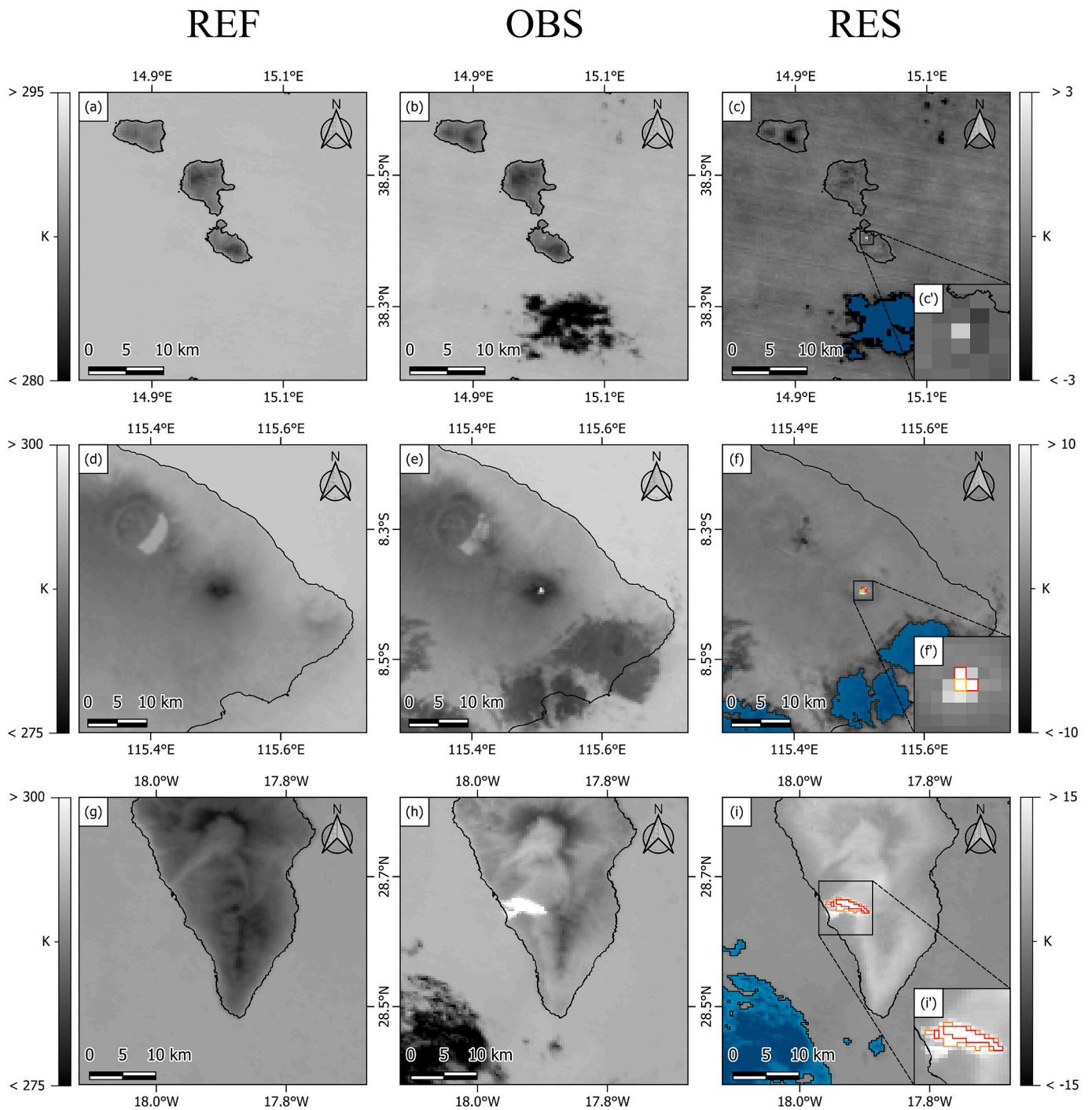
Fig. 5. Reference (REF), Observed (OBS), and Residual (RES) scenes for Vulcano (**a,b,c**), Agung (**d,e,f**), and La Palma (**g,h,i**), respectively. Blue patches represent cloudy pixels resulting from Test 3. Red and orange shapes in **f** (and **f'**) and **i** (and **i'**) depict the anomalous pixels detected after Test 1 and 2, and after Test 4, respectively. Note how, in figure **c** (and **c'**), tests based on fixed thresholds (i.e., tests 1, 2, and 4), failed to detect the thermal anomaly, although a thermally anomalous pixel can be visually identified. **b**) acquired on August 17th, 2019, at 01:00 (UTC). **e**) acquired on June 15th, 2018, at 17:42 (UTC). **h**) acquired on October 21st, 2018, at 03:12 (UTC). (For interpretation of the references to colour in this figure legend, the reader is referred to the web version of this article.)

$$OBS_{ROI} \geq \overline{OBS_{ROI}} + 3\sigma OBS_{ROI} \qquad \text{[test 8]}$$

The *Candidate Alerts* are therefore those that have passed at least one test amongst tests 1 to 4 and/or 7 to 8.

4.3.4. Hotspot detection within Volcano-Specific ROIs (VS_{ROI})

If a persistent thermal anomaly can be distinguished, a VS_{ROI} – usually extending for ~1 × 1 or ~ 2 × 2 km depending on the size of the thermal feature(s) – is centred on the hottest pixel (Fig. 8). To detect

Candidate Alerts within the VS_{ROI} region(s), a similar approach to that presented in tests 4 and 6 is applied, yet thresholds are lowered to increase the detection sensitivity exclusively within the VS_{ROI}:

$$Z - RES_{VS_{ROI}} \geq 5 \qquad \text{[test 9]}$$

The already detected *Candidate Alerts* (tests 1 to 9), if any, are temporary removed from the scene, and the mean and standard deviation of both observed ($\overline{OBS_{VS_{ROI}}}$ and $\sigma OBS_{VS_{ROI}}$, respectively) and *RES* ($\overline{RES_{VS_{ROI}}}$ and $\sigma RES_{VS_{ROI}}$, respectively) scenes are computed. Hence:
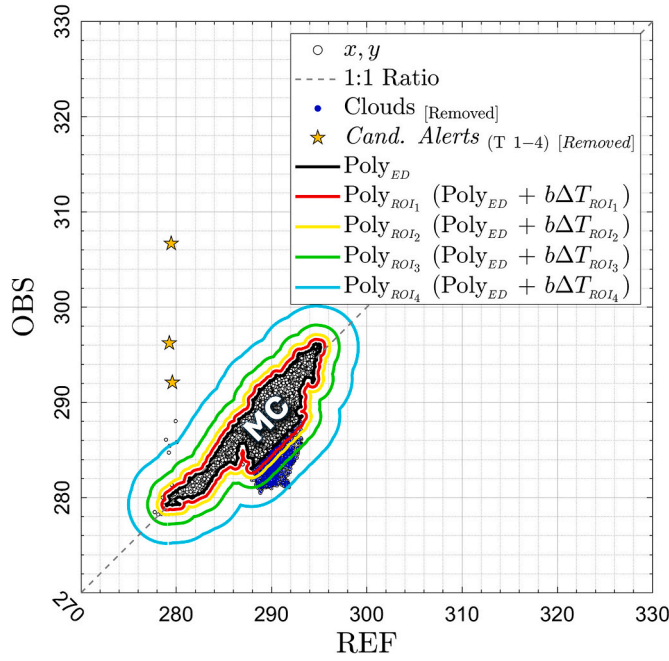
Fig. 6. Scatter plot showing the relationship between the vectorised REF (x-axis) and OBS (y-axis) matrices presented in Fig. 5d and 5e, respectively. The grey dashed line shows the 1:1 ratio. Note how most of the datapoints (i.e., Main Cluster - MC) lie around this line. Orange stars depict the pixels already flagged as candidate alerts during tests 1–4 (see Fig. 5f; Note, these pixels are factually excluded from the ED clustering approach (the same applies to cloudy pixels; see text) but have been included in the figure to show their typical distribution). The black line (Poly$_{ED}$) shows the result of the ED-clustering approach, delimiting the MC of non-anomalous data. Red, yellow, green, and cyan envelopes depict the buffer (Poly$_{ROIn}$) added to Poly$_{ED}$ for ROI$_1$, ROI$_2$, ROI$_3$, and ROI$_4$, respectively. Note, the same plot after running Test 5 and 6 is shown in Fig. 7 (note how anomalous data points have been detected, thus added amongst the *Candidate Alerts*). (For interpretation of the references to colour in this figure legend, the reader is referred to the web version of this article.)

$$OBS_{VS_{ROI}} \geq \overline{OBS_{VS_{ROI}}} + 2\sigma OBS_{VS_{ROI}} \ or \ OBS_{VSROI} \geq \overline{RES_{VS_{ROI}}} + 2\sigma RES_{VS_{ROI}}$$
[test 10]

Where pixels satisfying test 10 are added to the *Candidate Alerts*.

It is worth it to mention that in a single scene multiple VS_{ROI} can be placed over different location, enabling a greater coverage of sparse thermal features (i.e., fumarolic fields) over the entire volcanic edifice. Detailed evidence on the role of a VS_{ROI} over low-temperature targets is provided as Supplementary Material (S1).

4.3.5. Removal of residual false alerts, background BT computation and iterations

In this final step, all *Candidate Alerts* are subjected to a series of tests to remove potential false alerts and define *Confirmed Alerts* (hotspot-contaminated pixels).

The algorithm initially verifies that the BT of *Candidate Alerts* ($BT_{candidate}$) is at least 0.5 K above the background temperature (BT_{bg}). This ensures that pixels approaching the sensor's noise limits (see Table 1) are not identified as hotspot-contaminated. To further minimise the number of distal false alerts, we test whether their BT is higher than the theoretical BT_{bg} plus a ROI-dependent threshold (ΔT_{bg}):

$$BT_{candidate} > BT_{bg} + \Delta T_{bg}$$
[test 11]

where ΔT_{bg} takes one of the following values: 0.5 K (for VS_{ROI}, ROI$_1$, ROI$_2$), 0.75 K (for ROI$_3$) and 1 K (for ROI$_4$).

The BT_{bg} is computed iteratively by removing the *Candidate Alerts* from the scene and interpolating the gaps using a bi-cubic interpolation

of the surrounding non-contaminated pixels (Fig. 9). Hence all pixels failing test 11 are unflagged and return to the original matrix. The procedure is iterated until all *Candidate Alerts* satisfy test 11.

Finally, a set of spatial conditions is applied to minimise the number of false alerts by taking into consideration the typical spatial pattern characterising volcanic phenomena. These are:

If ROI$_1$ and ROI$_2$ contain no *Candidate Alerts & there are less than 10 Candidate Alerts* within ROI$_3$ and/or ROI$_4$ & these all fail Test 1 and 2, *then* these are assumed to be false alerts and are 'unflagged'   [test 12]

If ROI$_1$, ROI$_3$, and ROI$_4$ contain no *Candidate Alerts &* ROI$_2$, contains a single *Candidate Alert, then* this is assumed to be a false alert and is 'unflagged'   [test 13]

If Candidate Alerts are located on water bodies (as per *LW Mask*) & are not connected to inland *Candidate Alerts, then* these are assumed to be false alerts and are 'unflagged'   [test 14]

If Candidate Alerts are located outside the VS_{ExcROI}, *then* these are assumed to be false alerts and are 'unflagged'   [test 15]

If Candidate Alerts are located more than ~1 km from the shoreline (as per LW Mask), *then* these are assumed to be false alerts and are 'unflagged'   [test 16]

Candidate Alerts, namely pixels satisfying at least one Test between 1 and 11 and failing Test 12 to 16 are finally labelled *Confirmed Alerts*, thus pixels most likely contaminated by hotspots of volcanic source.

If *Confirmed Alerts* are detected and, after temporarily removing these from the scene, the whole process is repeated until no further *Confirmed Alerts* are detected between two consecutive runs. At this stage, following the approach described above, *Confirmed Alerts* are removed from the scene and the final BT_{bg} is calculated to allow estimation of the volcanologically relevant parameters detailed in Section 4.4 and Supplementary Material S2.

4.4. Step 3 – Radiative power and parameters retrieval

With the *Confirmed Alerts* retrieved, a final step is dedicated to estimating and storing the volcanological relevant parameters (see Supplementary Material S2). Amongst them, the quantification of thermal energy sourced by volcanic targets is a key metric to assess the status of the volcanic system (Wang and Pang, 2023). Previous studies attempted to estimate the intensity of the volcanic events by mean of statistical and/or normalised indices (i.e., Tramutoli, 1998; Tramutoli, 2005; Rabuffi et al., 2022), others adopted the maximum temperature above the background of the alerted pixel(s) as a proxy of the energy involved (i.e., Ball and Pinkerton, 2006; Calvari et al., 2020; Ramsey and Dehn, 2004; Reath et al. 2019a and 2019b). Nonetheless, as advised by Ramsey et al. (2023), a maximum pixel temperature may not be representative of the energy associated with thermal anomalies spreading over an extensive area. As such, following the approach previously employed by others (i.e., Ramsey et al., 2023; Corradino et al., 2023; Blackett, 2014; Mia et al., 2018; Thompson et al., 2022) we estimate the radiative power (Φ_{Rad}; in watt) of each alerted scene as:

$$\Phi_{Rad} = \sum_{i=1}^{N_{pix}} \sigma \bullet \varepsilon \bullet \left(BT_{alert,i}^4 - BT_{bg,i}^4\right) \bullet A$$
(5)

where N_{pix} is the number of *Confirmed Alerts*, σ is the Stefan-Boltzmann constant (5.67×10^{-8} W m^{-2} K^{-4}), ε is the surface spectral emissivity, here assumed to be unity for sake of simplicity (i.e., Pieri and Abrams, 2005; Kervyn et al., 2008; Coppola et al., 2016b), BT_{alert} and BT_{bg} are the temperature of the alerted pixel and its corresponding background value, respectively, and A is the pixel surface area, namely 140,625 m^2 for VIIRS I5 pixels.
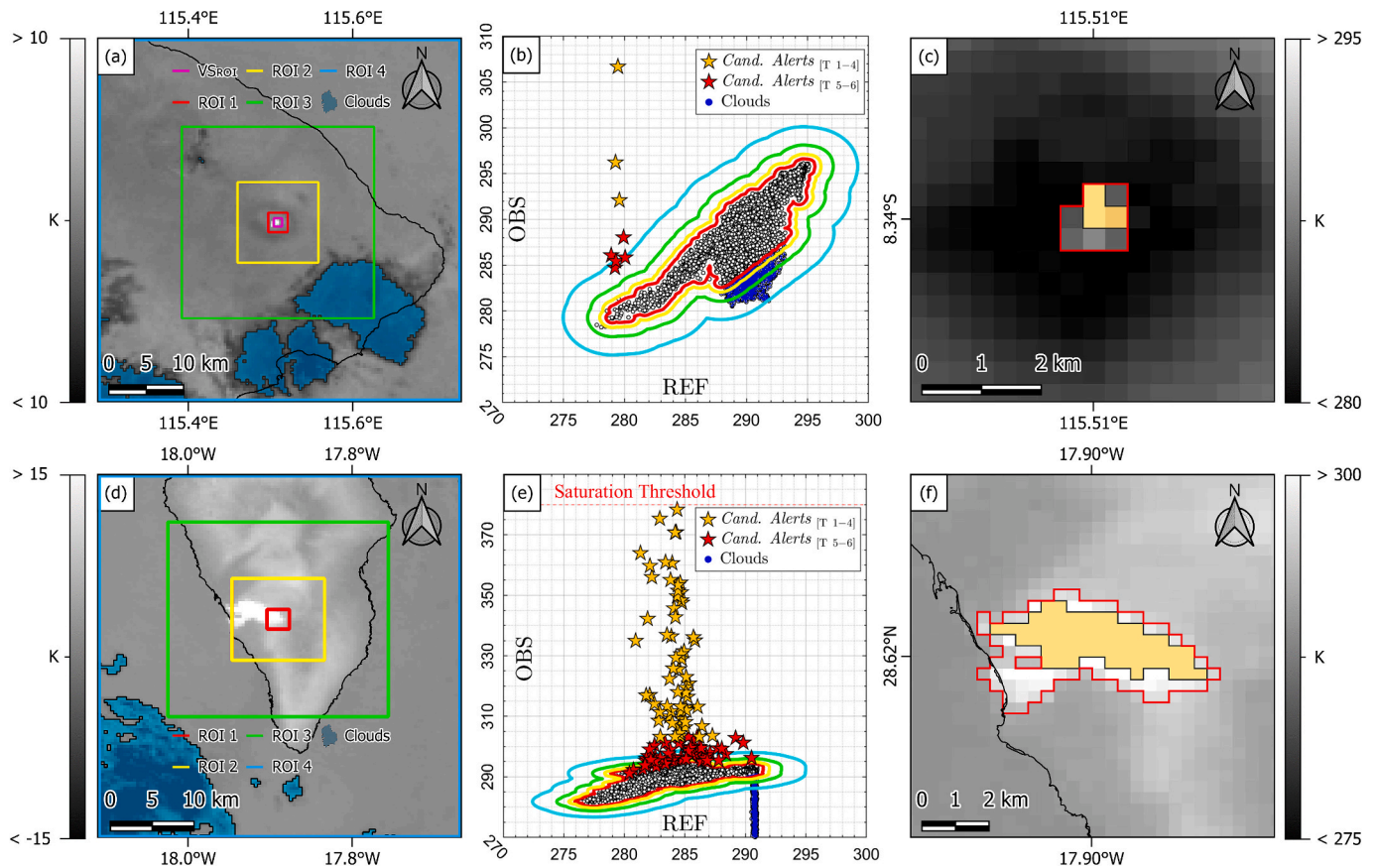
Fig. 7. a,d) Residual (RES) scenes of Mount Agung and La Palma, respectively, as seen in Fig. 5f,l with ROIs overimposed. Blue patches represent cloudy pixels (Test 3). **b,e**) ED-clustering. Orange stars represent Candidate Alerts identified with Test 1–4, red stars show Candidate Alerts detected with Test 5–6. Blue datapoints show the location of cloud-contaminated pixels. The horizontal red dotted line in (**e**) shows the I-5 channel saturation threshold (see Table 1). **c,f**) Zoom up over the eruptive scene of Agung and La Palma, respectively (for acquisition dates see Fig. 5). Filled orange patches show the pixels detected with tests 1–4. Red outlines show the Candidate Alerts detected after ED clustering and contextual analyses (Tests 5–6). Note, ROIs distortions (flattening) in (**d**) is a graphical artefact due to WGS84 projection. (For interpretation of the references to color in this figure legend, the reader is referred to the web version of this article.)

5. Algorithm performance

The efficiency of the algorithm was assessed on three case studies (Vulcano, Agung, La Palma), to evaluate its performance both on *land*- and *water-dominated* scenarios, as well as on low- (i.e., fumarolic) and high- (i.e., effusive) thermal regimes. Validation of the algorithm's outputs was conducted by visually inspecting the ~23,000 scenes acquired within the investigated period, labelling the outputs according to the criteria presented by Massimetti et al. (2020), namely:

(i) True Volcanic Alert (TVA): an anomaly detected by the algorithm explicitly related to volcanic activity (hot degassing, lava body exposed, hot eruptive materials exposed and possibly confirmed by literature or consistent with the background knowledge of volcano activity), showing a distinguishable thermal inconsistency with the surrounding environment;

(ii) Fires or Anthropogenic alert (FoA): an anomaly detected by the algorithm expressly and visually related to wildfire occurrence and/or located near human-settled areas;

(iii) False Positive Alert (FPA): an anomaly detected by the algorithm, visually related to cloud coverage and/or cloud edges, secondary cloud fringes, geometrical artefacts, or clearly not related to known or ongoing volcanic processes;

(iv) False Negative Alert (FNA): a visually distinguishable thermal anomaly undetected by the algorithm, clearly related to volcanic processes, having a ΔT, with respect to their surrounding pixels, higher than the thresholds outlined in Section 4.3.5.

Following Genzano et al. (2020), we define the False Positive Rate (*FPR*) as the ratio between the number of false detections (N_{FPA}), the latter resulting from the visual inspection, and the total number of scenes (N_{Scenes}) available for the two investigated regions:

$$FPR = \frac{N_{FPA}}{N_{Scenes}} \qquad (6)$$

From now on, we also name True Volcanic Alerts (*TVA*) the alerts confirmed to be of volcanogenic source via visual inspection, thus those not flagged as FPA as:

$$TVA = N_{Alerts} - N_{FPA} \qquad (7)$$

Finally, we provide the False Negative Rate (*FNR*) as the number of missed alerts (N_{FNA}) divided by the number of visually selected scenes displaying evidence of volcanogenic thermal anomalies (N_{Manual}) as:

$$FNR = \frac{N_{FNA}}{N_{Manual}} \qquad (8)$$

As evinced from Table 2, the algorithm well performs both on land and islands, with an intrinsic FPR of 1.77 %, 1.90 % and 1.79 % for Vulcano, Agung, and La Palma, respectively. A detailed investigation revealed that most of these false alerts (~85 %) are associated with cloud-edge effects, with the remaining due to geometric distortions (high satellite zenith resulting in a mismatch between REF and OBS) (see Supplementary Material S3). Nonetheless, as summarised in Table 2, the already-minimal occurrence of FPAs can be simply, yet drastically reduced to 0.47 % by applying distance (from the summit of the volcano,
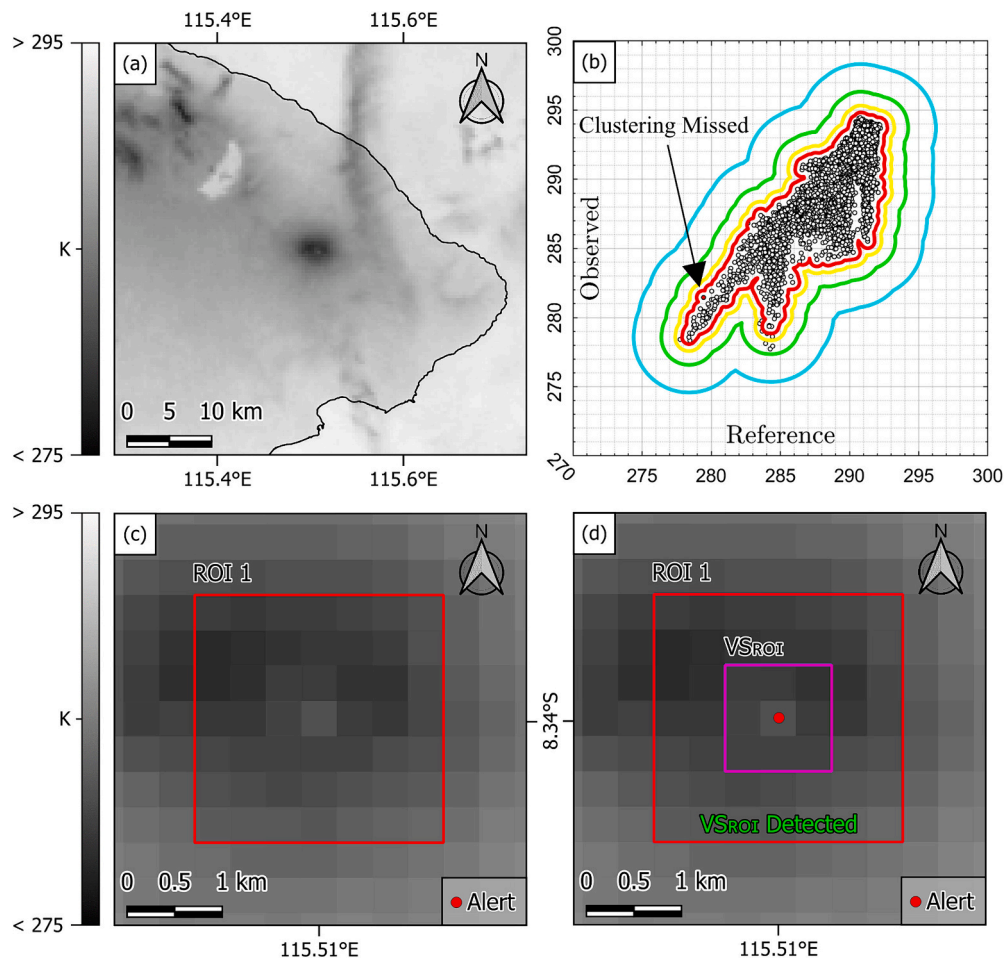
Fig. 8. Subtle thermal anomaly at Agung (February 10th, 2013, at 17:24 UTC) missed by initial fixed thresholds (**a**; Tests 1–4), ED clustering (**b**; Test 5) and ROI$_1$ contextual statistics (**c**; Test 6), but detcted applying a VS$_{ROI}$ (**d**; i.e., Tests 9–10). Note how the VS$_{ROI}$-detected Candidate Alert is indeed not anomalous in the cartesian domain, so that it gets embedded within the main cluster of data (red dot in **b**; indicated by the black arrow). However, when placed in a spatial domain, the thermally anomalous pixel stands out against its surrounding (**c**). (For interpretation of the references to colour in this figure legend, the reader is referred to the web version of this article.)

or from the thermally anomalous zone) and geometrical filtering, while avoiding removal of any relevant TVA (see Supplementary Material S4). These results are in excellent agreement with those reported for other hotspot detection systems, featuring FPR ranging from ≲1 % to >20 % (i. e., Kervyn et al., 2008, Steffke and Harris (2011), Massimetti et al., 2020, Coppola et al., 2014, Genzano et al., 2023, Marchese and Genzano, 2022, Lacava et al., 2018, Ramsey et al., 2023, Chu et al., 2020).

6. Thermal trends

6.1.1. Vulcano

Since the late 19th century, following the latest magmatic eruption (1888–1890; Selva et al. 2020), a fumarolic field established within Gran Cratere (see Fig. 1b; Diliberto, 2017 and Diliberto et al., 2021, Barberi et al., 1991, Capasso et al., 1994, Chiodini et al., 1995). Several studies provided estimates of the thermal outputs associated with the fumarolic activity, both collected via ground instruments and space-borne platforms. Amongst them, combining ASTER and ground truth data, Mannini et al. (2019) presented the results of a detailed investigation conducted between 2000 and 2019. These authors suggested that the average diffuse radiative power, at the time of sampling (see Mannini et al., 2019 for details), was 1.22 ± 0.39 MW (1σ). These values are

largely in agreement ($R^2 = 0.86$; Fig. 10c) with the VIIRS-derived average radiative power obtained proximally to Mannini et al. (2019) field surveys (Fig. 10a), namely 1.07 ± 0.37 MW (1σ). Extending the period of analysis, Pailot-Bonnétat et al. (2023) presented the ASTER-derived thermal outputs for 2021, thus including the beginning of the unrest period. These authors suggested that, between January and July 2021, the radiative power was comprised between ~3–8 MW, reaching ~16 MW at the beginning of October 2021 (see Pailot-Bonnétat et al. (2023) for details). These findings, as depicted in Fig. 10b, are consistent with our VIIRS-derived measurements, where values of ~2–8 MW were recorded until July 2021, to reach ~15.5 MW in the first week of October 2021.

In terms of overall trends, the baseline activity of Vulcano shows an average Φ_{Rad} of ~1.99 MW, characterised by a seasonal pattern with thermal maxima recurring within summer periods (Fig. 10a). This is consistent with the seasonal tendency observed by Corradino et al. (2023) who investigated the ~15-year-long thermal outputs of Vulcano through ASTER acquisitions. These authors further explored the causes of these seasonal fluctuations, finding a strong negative correlation between meteoric precipitations and areal expansion of the radiating source(s), in line with previous observations made by Gaudin et al. (2015) and de Bremond and Gibert (2022) in other hydrothermal settings. Noteworthy, during the summer of 2019, a transient increase in radiative power was recorded by our data, in concomitance with the highest pre-unrest H_2O flux value recorded at least since 1982
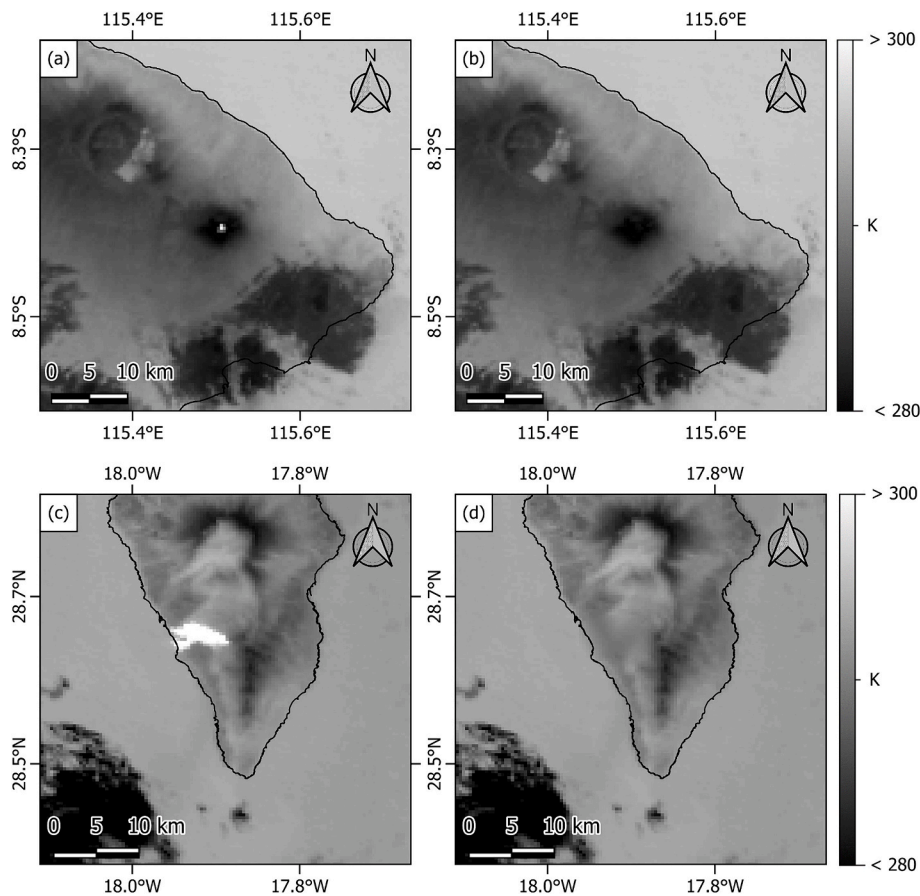
Fig. 9. a,c) Observed (OBS) scenes at Mount Agung and La Palma, respectively (for acquisition dates see Fig. 5). **c,d)** Theoretical background BT (BT$_{bg}$) for Agung and La Palma, respectively, obtained by first removing the Confirmed Alerts and then filling the gaps using a bi-cubic interpolation.

Table 2

Summary of TIRVolcH performance. *Raw FPA as obtained from TIRVolcH processing. **Residual FPA, namely the FPA remaining after applying geometrical and spatial filtering. In particular, we discarded all alerted scenes acquired with a zenith angle $>50°$ (see Section 7.5 for rationale). Furthermore, in agreement with the volcano-specific type of activity that occurred within the investigated period, we discarded scenes with thermal anomalies originating more than 0.75, 2, and 7 km away from the central coordinates of Vulcano, Agung, and La Palma, respectively.

	Vulcano	Agung	La Palma	Total
N_{Scenes}	8656	6849	7413	22,918
N_{Alerts} (%)	2179 (25.17)	2566 (37.47)	1173 (15.82)	5918 (25.82)
N_{Manual} (%)	2608 (30.13)	2863 (41.80)	1107 (14.93)	6578 (28.70)
TVA (%)	2026 (92.98)	2436 (94.93)	1054 (89.86)	5516 (93.21)
FoA	–	2	7	9
N_{FNA}	582	427	68	1077
FNR	22.32 %	14.91 %	6.14 %	16.37 %
Raw FPA*				
N_{FPA}	153	130	133	416
FPR	1.77 %	1.90 %	1.79 %	1.82 %
Residual FPA (after filtering)**				
N_{FPA}	45	34	29	108
FPR	0.52 %	0.50 %	0.39 %	0.47 %

(Inguaggiato et al., 2023), and consistent with increased thermal anomalies reported by Rabuffi et al. (2022) and Coppola et al. (2022).

In September 2021, ground instruments detected sudden variations in micro-seismicity and ground deformation, these associated with circulations of pressurised hydrothermal fluids (Inguaggiato et al., 2022a;

Federico et al., 2023). In the latter half of September 2021, the anomalous geophysical parameters were followed by increased fumarole temperatures and alteration in the geochemical composition of ground-exhaling gasses (Inguaggiato et al., 2022a; Di Traglia et al., 2023). The rapid escalation of the volcanic crisis prompted the DPC to raise the alert level from green to yellow on October 1st, 2021 (DPC, 2021; Fig. 10a,b).

The time series presented in Fig. 10a reveals that a sudden and marked increase of the radiative power was observed since August 2021, in agreement with in-situ observations (Inguaggiato et al., 2022a, Di Traglia et al., 2023). A peak of ~15 MW was recorded on October 4th, 2021, this being temporally consistent with the maximum Volcanic Radiative Power (VRP) value reported by Coppola et al. (2022) and Campus et al. (2024). Thereafter, a lowering of the radiative power was observed, in agreement with a reduction in seismicity, deformation, and ground exhaling CO_2 fluxes. The thermal activity reinvigorated in April 2022, concurrently with an anomalous degassing from underwater hydrothermal vents in the Baia di Levante (INGV, 2022a; Inguaggiato et al., 2022b; Gurrieri et al., 2023). By June 2022, measurements matched the previous peak of ~15 MW, consistently with a new increase in VRP values and SO_2 emissions (Coppola et al., 2022; INGV, 2022b). Thereafter, a steady decline was observed, with radiative power values returning below 8 MW by the end of August 2022.

6.1.2. Agung

After 53 years of quiescence, Mt. Agung underwent major unrest in late September-early October 2017, with variations in the equilibrium of the system reported since May 2017 (Syahbana et al., 2019). Despite the half-century-long quiescence, fumarolic and solfataric activity within the inner crater was reported since late 1980s by GVP (1989), while thermal evidence was distinguishable at least since ASTER acquisitions
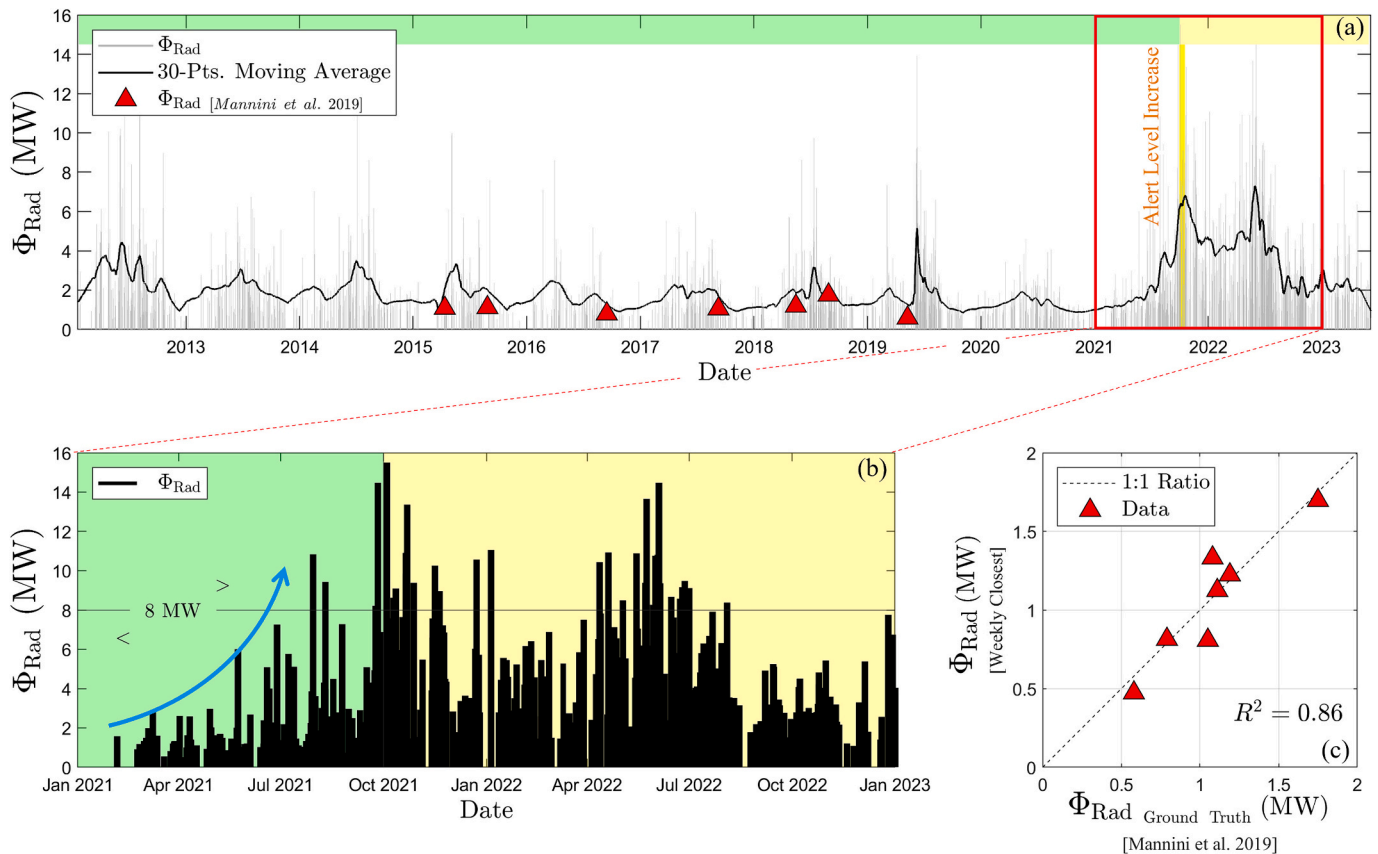
Fig. 10. **a)** Grey bars show the VIIRS-derived radiative power at Vulcano. The black line represents the 30-point moving average. Red triangles depict ground-truth observations reported by Mannini et al. (2019). Coloured bars at the top show the alert level timeline according to the DPC. The yellow vertical bar depicts the variation of the alert level (October 1st, 2021). The red box depicts the pre-unrest and (part of the) unrest period, as highlighted in **b**), where the horizontal black line shows the 8 MW transition discussed by Pailot-Bonnétat et al. (2023). **c)** Relationship between ground-truth data collected by Mannini et al. (2019), and the closest value obtained by TIRVolcH-processed imagery searched on a 7-day window centred on Mannini and co-authors survey dates (note, the 7-day search window was necessary to compensate for lack of information due to cloud coverage). To reduce seasonal noise, acquisitions <1 MW within the red box were discarded. **(For interpretation of the references to colour in this figure legend, the reader is referred to the web version of this article.)**

begun (Way et al., 2022; see ASTER Image Database for Volcanoes (Urai and Pieri, 2011a, 2011b, Way et al., 2022); https://gbank.gsj.jp/v sidb/image/Agung/volinfo.html) and throughout the first two decades of 2000s (i.e., Triyono and Khomarudin, 2020). Although remotely sensed data revealed the occurrence of thermally distinct volcanogenic activity, at the time of writing, no previous studies have attempted to quantify the thermal energy associated with these phenomena, likely discouraged by a lack of monitoring programs and ground instruments prior to the 2017 unrest (Syahbana et al., 2019).

To mitigate the lack of data, cross-validation with ASTER-retrieved radiative power was carried out (see Supplementary Material S5) to validate both trends and magnitudes of the time series presented in Fig. 11a. The average ASTER-retrieved radiative power for the whole period was 12.14 MW, closely matching the 11.78 MW computed from VIIRS measurements.

To statistically corroborate the visually remarkable association between ASTER and VIIRS time series (Fig. 11a,b), we identified 49 cloud-free scenes acquired concurrently from both sensors with a gap comprised between ±3 h. Statistical evaluation confirmed the strength and robustness of the association, returning $R^2 = 0.92$, m = 0.75, and ρ = 0.94 (p-value <0.001; Fig. 11c). The best-fit coefficient between the two variables suggests that a minor deviation between VIIRS- and ASTER-retrieved radiative power measurements exist. Nonetheless, the above analyses assume that no thermal variations occurred between acquisitions and that geometrical views and meteorological conditions remained unchanged between pairs of data. This, however, is seldom the case, especially in mountainous environments where acquisition

geometries play a major role in the correct quantification of thermal energy (Coppola et al., 2010), and where drastic variations in meteorological conditions can take place within minutes (Aveni and Blackett, 2022; Aveni et al., 2023). Nonetheless, assuming that these discrepancies were not related to geometrical artefacts and/or meteorological factors, this deviation remains consistent with that observed at Vulcano between the results of this work and those presented by Pailot-Bonnétat et al. (2023), suggesting that minor discrepancies between measurements are likely related to the coarser resolution of VIIRS pixels.

Further evaluation of the time series revealed an extraordinary parallel with the unrest timeline (Fig. 11a,b) which has been subdivided into coloured phases, according to the alert level raised by the Indonesian Center for Volcanology and Geological Hazard Mitigation (CVGHM). Accordingly, the average radiative power of the baseline thermal activity (i.e., the green alert period in Fig. 11a) was 4.21 MW and 3.94 MW, from ASTER and VIIRS, respectively (that is slightly higher than the baseline of Vulcano; see Section 6.1.1).

The pre-unrest maximum value $\lesssim 10$ MW was exceeded three days prior to the alert level being raised from green (Normal; Level I) to yellow (Waspada; Level II) in response to a sudden increase in ground deformation and seismic tremor amplitude that occurred on September 14th (Fig. 11a; Syahbana et al., 2019). Corroborating the veracity of these measurements, the same pattern was observed on the manually picked time series and, on September 12th, further validated by ASTER measurements returning a quasi-identical value, the latter exceeding for the first time the 10 MW threshold. Indeed, the empirically derived threshold was only reached once prior to the escalation of the unrest.
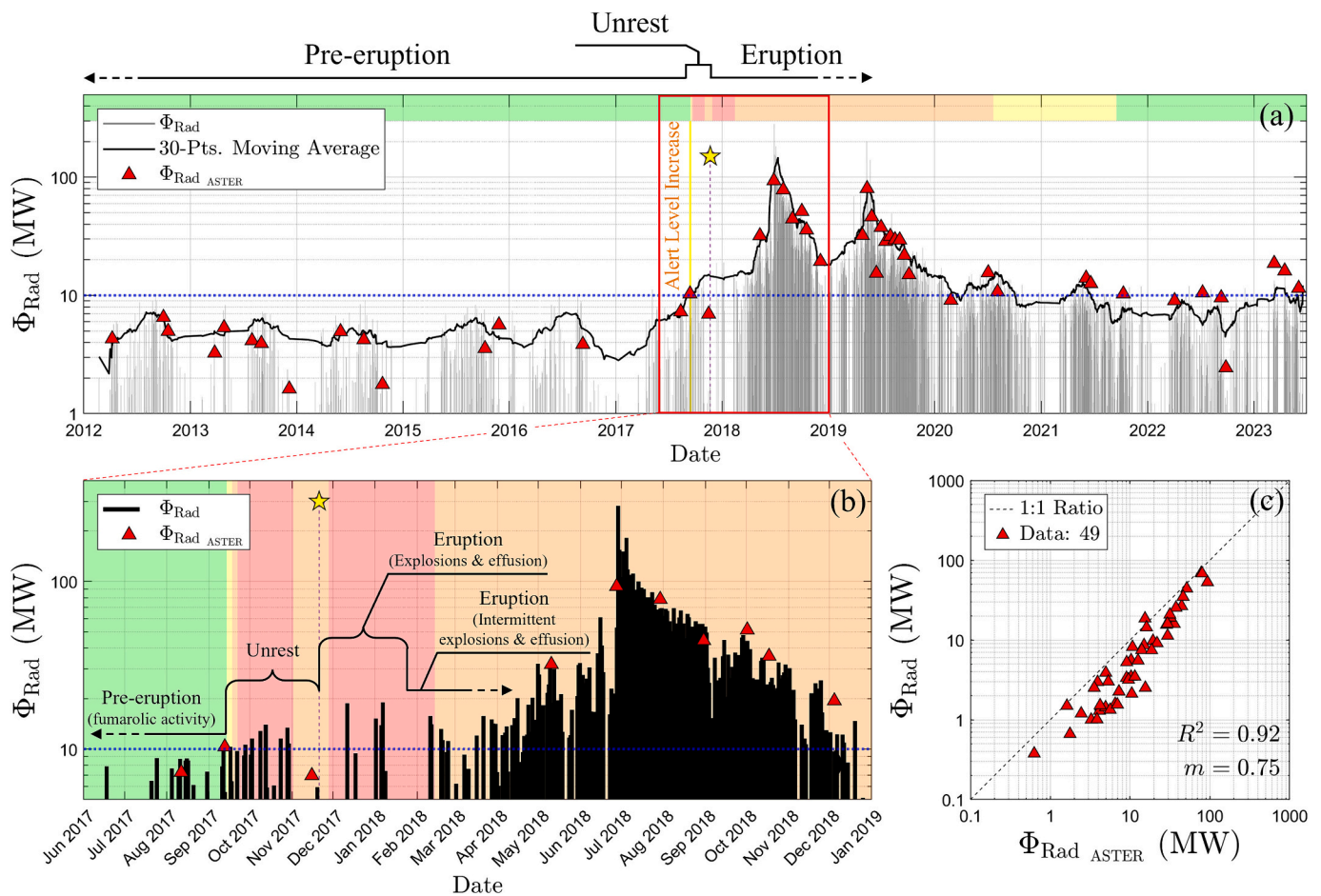
Fig. 11. a) Grey bars show the VIIRS-derived radiative power of Agung. The black line represents the 30-point moving average. Red triangles depict ASTER-derived radiative power values. Coloured bars at the top show the alert level timeline according to the CVGHM. The yellow vertical bar depicts the first variation of the alert level (September 14th, 2017). The blue dotted line depicts the pre-unrest maxima value of 10 MW. The yellow star marks the first phreatomagmatic explosion (November 21st, 2017). The red box depicts the pre-unrest into the unrest period, as highlighted in (**b**). **c**) Relationship between ASTER- and TIRVolcH-derived radiative power. (For interpretation of the references to colour in this figure legend, the reader is referred to the web version of this article.)

This was in mid-May 2017, in concomitance with the occurrence of the first seismic swarm associated with the volcanic unrest (Syahbana et al., 2019; Zulfakriza et al., 2020; Ardianto et al., 2021).

On September 18th and 22nd the alert level was raised to orange (Siaga; Level III) and red (Awas; Level IV), respectively, in response to an increase in seismicity and ground deformation (Syahbana et al., 2019). On October 29th a reduction in the geophysical parameter led the authorities to lower the alert level to orange again (Syahbana et al., 2019). Thermal anomalies recorded in this period oscillated between ~10 and ~13 MW (Fig. 11b). A series of phreatomagmatic explosions began on November 21st, leading, on the 25th of the same month, to the first magmatic event, as reported by Syahbana et al. (2019). The eruption was characterised by intense explosive activity coupled with the fast extrusion of lava inside the crater, prompting the authorities to raise the alert to the red level again (Syahbana et al., 2019). Although the detection frequency was largely affected by extreme cloud fraction, the latter exceeding 90 % during the Indonesian wet season (November–May; Hidayat et al., 2012, Tampubolon et al., 2020), the so far highest thermal anomalies reached 15–20 MW and persisted on this level until February 10th, 2018 when the alert level was lowered to orange due to a decrease of all the eruptive parameters (Syahbana et al., 2019).

Thereafter, the disbandment of cloud coverage permitted a better observation of the eruptive dynamics, revealing a gradual re-intensification of the thermal activity (Fig. 11b). The increasing thermal trend climaxed on June 28th, 2018, where a maximum value of

~280 MW was recorded, the latter associated with a new surge of lava into the summit crater, major explosive activity, and substantial SO_2 emissions (GVP, 2018; Syahbana et al., 2019; Andaru et al., 2021). Thereafter, a steady decline in thermal activity continued until January 2019, when a sudden shift in the thermal regime announced the beginning of a new phase, the latter characterised by the alternation of dome-growing episodes and eruptive events (Andaru et al., 2021). This phase led toward a second thermal peak, reaching its maxima on May 12th, 2019, punctuated by a radiative power of ~200 MW, recorded in concomitance with a major explosion that produced a significant fallout of incandescent ejecta along the volcano's slopes (GVP, 2019). The thermal signal gradually decreased and returned within a range of 10–20 MW in July 2020, in agreement with the lowering of the alert level from orange to yellow. Return to a green alert level was eventually declared in September 2021, consistently with further lowering of the radiative power output. Since 2022, the radiative power remained relatively stable, oscillating around the ~10 MW threshold with sporadic detections up to ~14 MW, still slightly higher than the values recorded prior to the unrest.

6.1.3. La Palma

At 14:10 UTC, on September 19th, 2021, a fissure opened along the Cumbre Vieja ridge, in La Palma, beginning a new eruption (Castro and Feisel, 2022). The eruption lasted 85 days, producing 177.6 ± 5.8 Mm³ of lava, the latter effused with a Mean Output Rate (MOR) of ~24.1 m³/s (Civico et al., 2022; Bonadonna et al., 2022; Plank et al., 2023).

Subaerial lava flows covered an area of ~11.8 km² and reached a maximum and average thickness of 65 m and 15.2 m, respectively (Civico et al., 2022; Bonadonna et al., 2022; Plank et al., 2023; JRC, 2021; Amonte et al., 2022). The thermal signal associated with the initial stage of the eruption (Fig. 12) shows a gradual increase, from 253 MW on September 20th to a first peak of ~2.7 GW on September 29th, consistently with the trend described by Plank et al. (2023). After the initial peak of September 29th, the thermal signal gradually decreased to reach ~1 GW on October 6th. On October 7th, a sudden shift in the thermal regime was evidenced by Φ_{Rad} values of ~2.2 GW, these remaining relatively stable until two peaks of ~3 GW were recorded between the 17th and 21st of October. These peaks coincide with the opening of a new vent located approximately 300 m SE from the base of Tajogaite cone (GVP, 2022) and, possibly, with the highest trade-off between maximum areal expansion of the still-active lava flow and the still relatively high temperature of the emplaced chilling lava field. Since October 21st, a new decline in the thermal activity was observed, this reaching a new minima at the beginning of November, with radiative power values approaching ~1.1 GW. Thereafter, gradual intensification of the thermal activity led to a new peak of ~2.4 GW, the latter recorded between the 27th and 28th of November, in concomitance with the opening of a new vent to the NE of Tajogaite edifice and with the widening of the furthest extending right branch of the lava field (GVP, 2022). Thereafter, the activity gradually decreased, until December 13th, 2021, when an evident drop in the thermal signal effectively marked the end of the eruption, in agreement with the observations made by the ground-based personnel (Benito et al., 2023).

It is worth it to note that values recorded throughout the eruption are one order of magnitude greater than that registered at Mount Agung, and two orders of magnitude greater than the values recorded during the unrest at Vulcano. Nonetheless, it must be acknowledged that the thermal energy measured during the mainly effusive stages of the eruption is likely underestimated. This intrinsically relates to the application of the Stefan-Boltzmann approach (Eq. 8) on the assumption that a mainly homogenous temperature distribution exists, this being seldom the case over an active lava flow (see Wright and Flynn, 2003, Wright et al., 2010, and Harris, 2013 for details).

Fig. 12 also reveals that, unlike other systems, the high sensitivity of TIRVolcH enables the retrieval of the long-term (>2 years) cooling curve of the emplaced lava. Although beyond the purpose of this work, cooling

curves have been used to comprehensively estimate emplaced volumes (Ganci et al., 2012b; Torrisi et al., 2022), understand post-emplacement dynamics (Wittmann et al., 2017; Beccaro et al., 2023), and numerically model lava cooling behaviours (Patrick et al., 2004; Patrick et al., 2005). In this regard, we envisage that future studies might explore the valuableness of this information for volcanological purposes.

Similarly to the quantification of radiated energy, accurate geospatial information on the extent and advancement rate of lava flows remains key information for stakeholders and competent bodies to timely evaluate eruptive phenomena and revise expected scenarios; these being essential requirements for hazard management and risk reduction applications (Tsang and Lindsay, 2020, Hyman et al., 2022, Martín-Raya et al., 2023). The so far unprecedented trade-off between spatial and temporal resolution offered by the VIIRS instruments enables TIRVolcH to timely provide accurate geospatial information on the evolution of the eruptive activity. Fig. 13 corroborates this claim, revealing the outstanding agreement between the cumulative number of alerted pixels and the superimposed lava field outline.

The remarkable agreement between the extent of the lava field and the one retrieved by TIRVolcH-processed imagery suggests that evaluation of VIIRS-derived geospatial information during the eruptive crisis can provide crucial information to assess the evolution of the eruptive phenomena.

In the first stages of a volcanic eruption, the likelihood of inundation can be provided by calculating the speed at which the front(s) move downslope (Marquez et al., 2022). For instance, at La Palma, the initial Average Flow Front Velocity (AFFV) was estimated to be ~700 m/h, prompting the Spanish authorities to issue an evacuation order to ~5500 people (GVP, 2021). The AFFV, according to field measures, was revised to ~400 m/h by 17:38 UTC of the same day, with the further reaching front extending for ~1.4 km from the Tajogaite cone (Fig. 14a, i,j). The advancement rate reduced to ~200 m/h by the end of the day (GVP, 2021). Shortly after, at 02:54 UTC on September 20th, 12 h and 44 min after the magma reached the surface, VIIRS acquired the first scene over the Canary Island (Fig. 14a). The TIRVolcH-processed image showed that lava flows travelled westward for 2.37 (± 0.375) km, resulting in an average flow rate of 202 (± 32) m/h, perfectly consistent with ground observations (~200 m/h; GVP, 2021) and with a steady advancement rate since last ground measures were available (Fig. 14j). Field observations made at 19:13 UTC on September 20th (Fig. 14i)
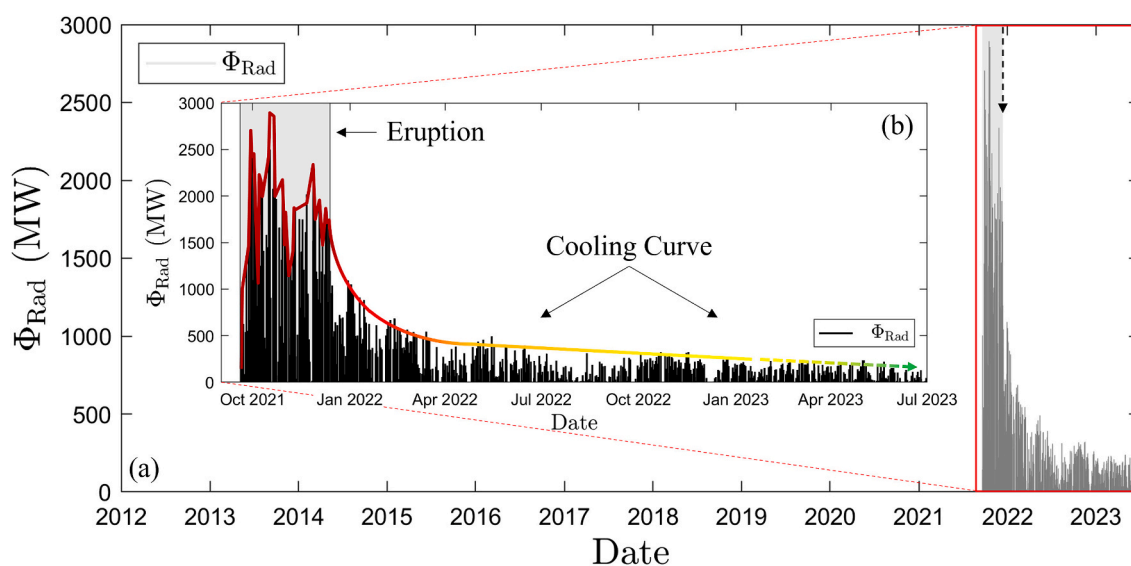

Fig. 12. a) VIIRS-derived radiative power recorded during the eruption of La Palma. The vertical dashed arrow depicts the end of the eruptive period. The red box highlights the period shown in **b**), where the grey shaded area shows the eruptive period. The red line within the eruptive period shows the thermal trends resulting from the visual inspection and selection of non-cloud-contaminated scenes. The red-to-green gradient-filled arrow represents the pluriannual cooling curve. **(For interpretation of the references to colour in this figure legend, the reader is referred to the web version of this article.)**
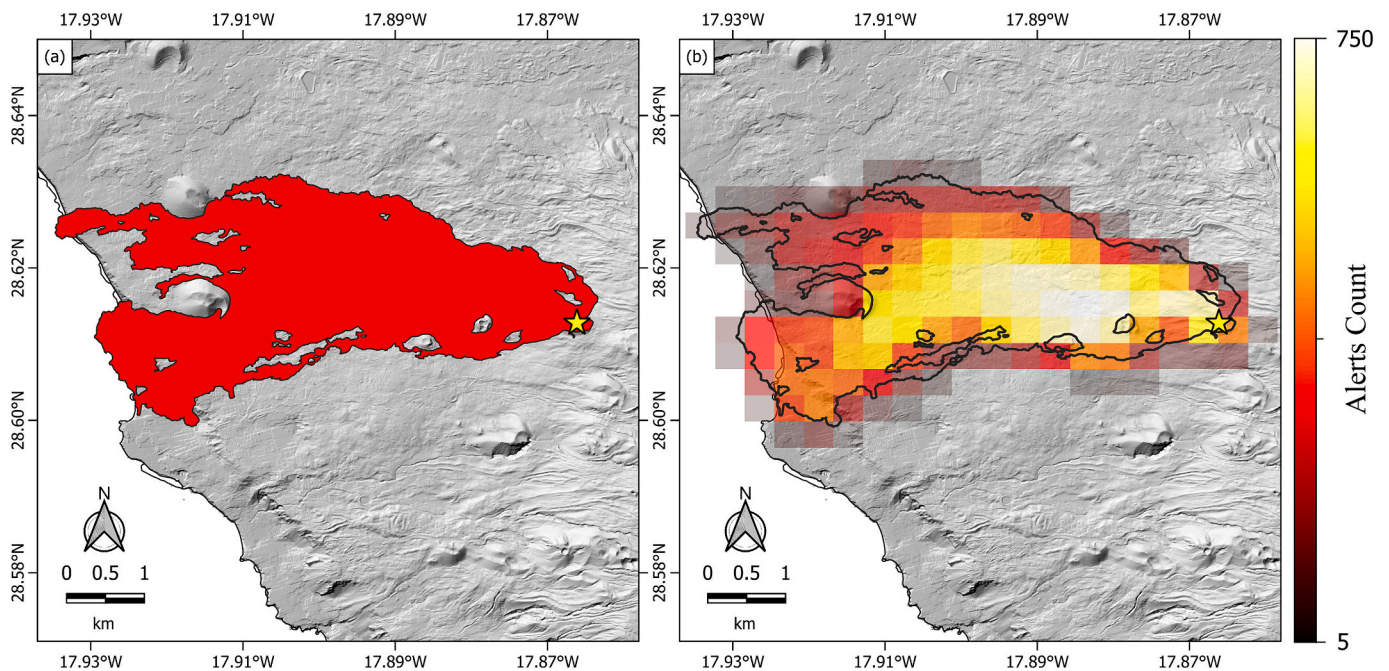
Fig. 13. a) Total extent of the lava flow as provided by Copernicus Emergency Management Service (2024). **b**) Outline of the lava flow extent, overlaid the cumulative number of alerts obtained from TIRVolcH-processed VIIRS imagery. The yellow star marks the location of the Tajogaite cone. (For interpretation of the references to colour in this figure legend, the reader is referred to the web version of this article.)

showed that the emplacement velocity further dropped to ~60 m/h. At that stage, lava flows reached ~3.22 km from the vent (Fig. 14j), covered an area of ~1 km^2 (Fig. 14i), and destroyed 166 buildings (GVP, 2021). At 02:30 UTC on September 21st, a new VIIRS acquisition suggested that the lava flow had reached 3.46 ($\pm$ 0.375) km, advancing at an average velocity of 46 ($\pm$ 16) m/h (Fig. 14b). Between September 21st and the early hours of the 26th, flows advancement was much slower. The further extending fronts advanced at a rate $\lesssim$ 5 m/h (GVP, 2021), moving from ~3.5 km to ~3.8 km from the vent (Fig. 14i). A consistent trend was inferred by VIIRS imagery, with lava flows confined at ~3.5 ($\pm$ 0.375) km from the vent (Fig. 14c,d,e). In the evening of September 26th, a transient shift in the eruptive regime let the AFFV reach ~100 m/h, this reducing to a relatively steady ~30 m/h shortly after. On September 27th at 03:12 UTC, a new VIIRS overpass (Fig. 14f) provided new estimates, with the further extending lava flow reaching 4.19 ($\pm$ 0.375) km from the vent, propagating with an AFFV of 31 ($\pm$ 16) m/h (Fig. 14j), perfectly in agreement with the latest ground-based observations. After ~9 days from the beginning of the eruption, the lava flows reached the coast, entering the sea on September 28th at 22:02 UTC (Fig. 14j), as clearly depicted from VIIRS imagery acquired in the early hours of September 29th (Fig. 14 g).

The excellent agreement between ground- and VIIRS-derived distances and velocities throughout the first two weeks of the eruption is shown in Fig. 14j, statistically corroborated by an R^2 = 0.94 and a ρ = 0.94 (Fig. 14k).

The remarkable consistency between ground truth and remotely sensed information confirms that the algorithm may effectively provide the location of the front(s) and its velocity with an accuracy of $\pm$1 pixel (375 m), to account for geolocation offsets and PSF-induced blurring effects. This information, especially at remote locations, might be essential to arrange evacuation plans, coordinate rescue operations, and timely locate affected areas and/or infrastructures (Coppola et al., 2016b).

7. Limits of TIRVolcH algorithm

As with all satellite-based systems, TIRVolcH faces a number of issues

that must be considered when interpreting the data. These are outlined below, together with steps that are planned to be implemented in the near future to enhance the quality and accuracy of the system.

7.1. False alerts

TIRVolcH algorithm has an intrinsic False Positive Rate (FPR) of ~1.8 %, largely within the range of other volcano monitoring systems. As detailed in Supplementary Material S3, ~95 % of these false alerts result either from severe temperature contrasts at cloud edges or mismatches between reference and observed scenes acquired at high zenith angles, due to geometrical distortions. The remaining ~5 % are generally related to anomalous surface temperature conditions (i.e., thermal inversions), wildfires, and/or anthropogenic factors (i.e., controlled fires, variations in land use, etc.). Although an initial screening attempts to discard clearly cloud-contaminated pixels (see Section 4.3.1) and, despite most false alerts can be identified and removed via spatial and geometrical filtering as demonstrated in Section 5, it must be noted that residual false alerts may generate spikes in the time series which, in turn, might erroneously be interpreted as occurrence of high-intensity thermal activity. To minimise the number of false alerts, current work is being conducted to develop a single-band cloud detection algorithm which can be fully integrated within the TIRVolcH workflow, without the need for adding external data and/or spectral bands.

7.2. Clouds and volcanic plumes

Clouds and volcanic plumes remain a major limitation in thermal remote sensing of volcanic activity and represent a major error source. During wet seasons, for instance, persistent cloud coverage may prevent observations of the eruptive phenomena for months. Similarly, clouds and volcanic plumes may partially or completely obscure the eruptive scene, leading to underestimation or miss detection of the thermal anomaly. Even if an alert is detected, thin cirrus may attenuate the thermal signal, resulting in an underestimation of the quantified radiative power. The above also applies to subpixel cloud contamination, affecting the overall pixel-integrated temperature, and in turn the
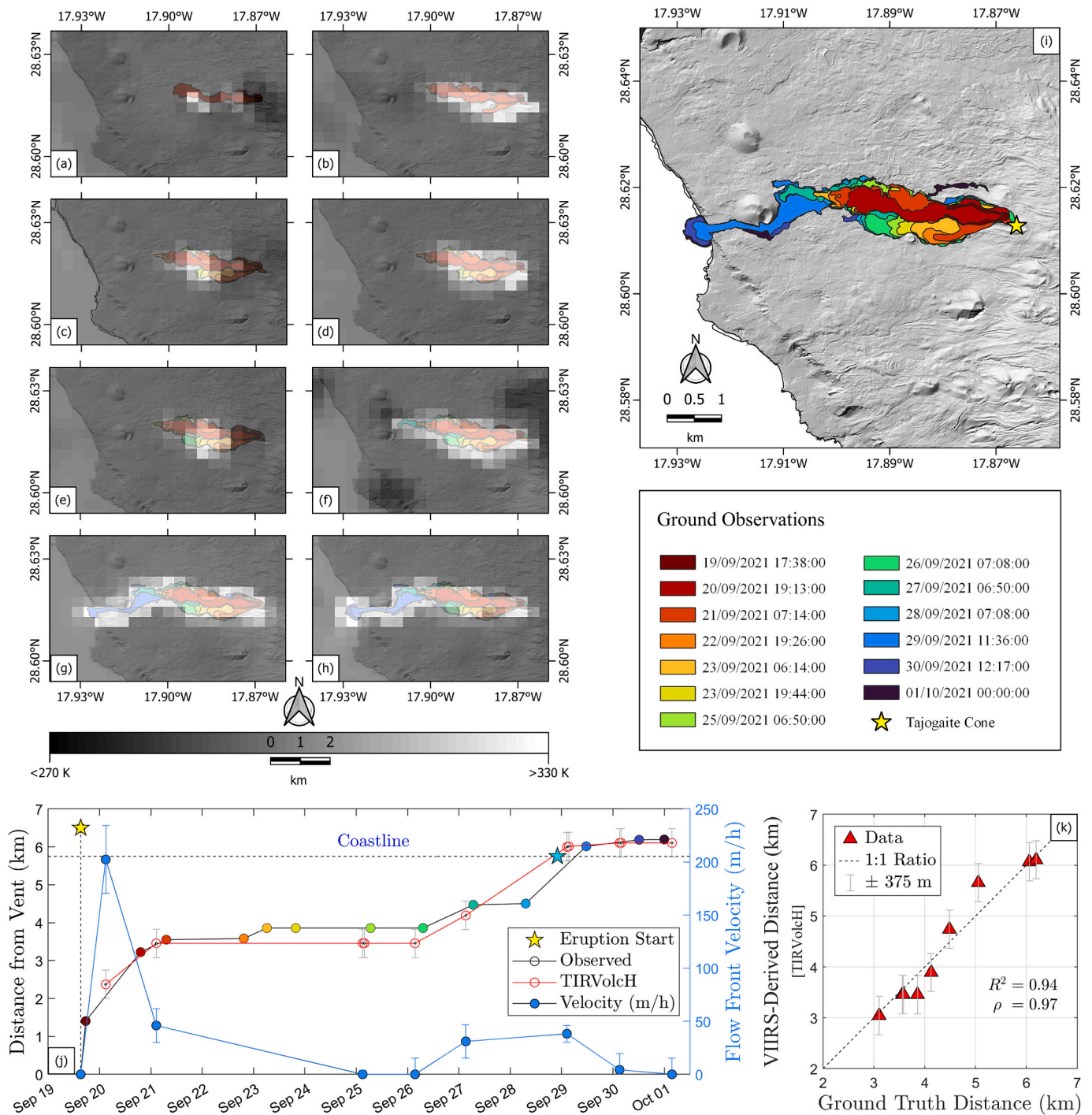
Fig. 14. a-h) Selection of mostly cloud-free VIIRS scenes acquired within the first 9 days of the eruption*, overlaid **i**) flow extent at different time intervals (digitalised from Gobierno de Canarias, 2023). The yellow star marks the location of the Tajogaite cone. **j**) Flow front distance (in red) and advancement velocity (in blue) as obtained from TIRVolcH. The black line (with coloured dots referring to inset **i**) shows the flow front distance calculated from (**i**) by taking the furthest vertex from the Tajogaite cone. The black dotted line represents the coastline. The cyan star marks when the lava first entered the sea. **k**) Scatterplot showing the consistency between hourly-interpolated ground truth and TIRVolcH retrieved flow distances. *Acquired on (all times are in UTC): **a**) 20/9/21 at 2:54; **b**) 21/9/21 at 2:30; **c**) 25/9/21 at 3:00; **d**) 25/9/21 at 3:48; **e**) 26/9/21 at 3:30; **f**) 27/9/21 at 3:12; **g**) 29/9/21 at 2:30; **h**) 30/9/21 at 3:06. (For interpretation of the references to color in this figure legend, the reader is referred to the web version of this article.)

radiative power. Moreover, cloud-contaminated pixels adjacent to alerted ones would be included in the interpolation of the theoretical background temperature, causing the background temperature to be lower than expected, thus affecting the estimation of the thermal energy. Hitherto, no robust methods exist capable of quantifying the amount of thermal radiation attenuated by clouds and/or volcanic plumes. As such, little can be done to assess the effect of clouds/plumes on remotely retrieved thermal information, leaving visual inspection as the only solution to assess the quality of the scene (Coppola et al., 2016b).

7.3. Satellite viewing geometry

Although drastic improvements have been made in the last decade, satellite viewing geometry still plays a major role in the quality of the

acquisitions and, in turn, in the accurate quantification of the radiated energy (Coppola et al., 2010; Aveni et al., 2023). The aggregation function implemented on VIIRS sensors (Cao et al., 2013a) allows improved accuracy even for scenes acquired with a zenith angle up to ~55° (Campus et al., 2022). Yet, scenes acquired with high zenith angles may prevent hotspot detection, depending on the incidence angle of the sensor with respect to that of the morphological features of the sensed region. For instance, thermal anomalies located inside steep crater rims, are likely masked at high zenith angles (Dehn et al., 2002; Coppola et al., 2015; Coppola et al., 2016b; Henderson et al., 2019). Besides, high scan angles produce distortions of the projected thermal anomaly, which may be spread over several adjacent pixels (Nishihama et al., 1997). The above is further exacerbated by a reduced pixel(s) geolocation accuracy, which compromises the correct identification of the eruptive vent(s) and/or the location of the lava front(s) (Coppola et al., 2012). That said, is common practice to discard scenes acquired with a zenith angle >50° (van Manen et al., 2006; Zakšek et al., 2015a, b; Marchese et al., 2019; Coppola et al., 2009), yet authors suggest that, especially in steep mountainous regions, scenes >30° should be rejected (i.e., Harris et al., 1997; Worden et al., 2014; Plank et al., 2019; Plank et al., 2021; Plank et al., 2023).

7.4. Atmospheric and emissivity corrections

At present, TIRVolcH does not apply atmospheric or emissivity corrections to the processed scenes. This choice is led by the will to operate a self-contained single-channel algorithm, capable of functioning without the addition of external data or bands. This implies that both in-scene atmospheric parameters and emissivity adjustments are impossible to estimate boasting a single TIR channel. Nonetheless, we might have followed the approach of previous authors who have assumed fixed emissivity values in the range of 0.90–0.98 (i.e., Lombardo et al., 2012; Blackett, 2013; Morgan et al., 2013; Blackett, 2014; Kaneko et al., 2019; Nádudvari et al., 2020), these being typical for basalts (Harris, 2013). Yet, in factual conditions, emissivity ranges from ~0.6 for molten rocks to ~0.995 for cooled basalt (Flynn et al., 1993; Ball and Pinkerton, 2006; Mia et al., 2014; Mia et al., 2017; Thompson and Ramsey, 2021; Ramsey et al., 2019). As such, accurate estimation of emissivity value to be applied to a pixel containing a mix of thermal components ranging from molten and cooling rocks to vegetated areas and water bodies remains unrealistic. As such, for the sake of simplicity, we followed the rationale of Pieri and Abrams (2005), assuming emissivity to be unity. Likewise, following the monoband rationale and, as previously adopted for other volcano hotspot detection systems (i.e., Kervyn et al., 2008), atmospheric corrections were not applied. Nonetheless, future studies will be conducted to assess the benefits introduced by applying standard atmospheric transmission models, which may be a good trade-off between data accuracy and minimal resources. Yet, cross-validation of our results against ground truth data confirms the overall accuracy of the presented radiative power measurements.

7.5. Reference scenes: Accuracy, availability, and limitations

Reference scenes are generated by applying a priori filtering and a number of statistical steps in the attempt to discard scenes contaminated by clouds and/or thermal anomalies (i.e., lava flows; see Section 4.2.2). At most locations, these steps are sufficient to generate uncontaminated reference images. However, for regions experiencing quasi-persistent cloud coverage, the quality of the reference scenes is considerably compromised. This is a combination of two factors: i) the reduced number of cloud-free scenes and ii) the inclusion of cloud-contaminated pixels in the generation of the reference images. Unless cloud detection is implemented a priori, little can be done to enhance the quality of these reference scenes, other than selecting scenes one-by-one and discarding contaminated pixels, one-by-one. Considering that the MIROVA VIIRS archive contains ~10,000 nighttime VIIRS acquisitions (2012–2023),

for a total of 1.7956×10^8 pixels, per volcano, the above consideration remains unrealistic. Besides, for regions where cloud fraction exceeds 90 % (i.e., Indonesia, see Section 6.1.2), even a manual inspection would return a small number of cloud-free imagery. However, as the archive continues to grow daily, and a higher number of scenes become available, the likelihood of acquiring uncontaminated scenes increases. Furthermore, on November 10th, 2022, the VIIRS-equipped NOAA's Joint Polar Satellite System-2 (JPSS-2) was launched (Román et al., 2024), further increasing the number of available scenes (although not available for download at the time of writing). As such, future revisions will attempt to improve the quality of the reference scenes for those regions mostly affected by cloud coverage

Is it worth it to mention that, at polar latitudes, Midnight Sun conditions cause i) fewer nighttime acquisitions in May and July (in the Northern hemisphere) and in November and January (in the Southern hemisphere), thus affecting the number of available scenes for these months, and ii) the total absence of nighttime scenes for the months between these intervals, namely June and December, in the Northern and Southern hemisphere, respectively, due to the presence of continuous daylight. Finally, discrepancies between observed and reference scenes may arise due to due to climate change effects.

8. Summary and future perspectives

In this work, we introduced a single-band TIR-based algorithm capable of detecting thermal anomalies in a variety of volcanic settings, from fumarolic fields and hydrothermal systems to high-temperature effusive events. By applying a set of temporal and contextual analyses, we were able to identify thermal anomalies for pixel-integrated temperatures as low as 0.5 K above the surrounding hot-spot-free background and as far as 25 km from the volcano's summit. In spite of its high sensitivity, TIRVolcH retains a false positive rate of just ~1.8 %. We also showed that the rate of false alerts can be further reduced to 0.47 % by applying geometrical and spatial filtering. Applying our algorithm to three case studies (Vulcano, Agung, and La Palma) – these diverging for i) type of activity (from hydrothermal to effusive), ii) thermal magnitude (~0.5 MW to ~3 GW), iii) topographic context (small islands to (mainly) land), and iv) climatological setting (from tropical and sub-tropical to Mediterranean) – we demonstrated the adaptability of TIRVolcH to a broad range of volcanic and geographical settings, and confirmed its capability to detect low-to-high thermal volcanic activity. The algorithm can be applied for detecting volcanic resurgence, tracking volcanic unrest, and monitoring the evolution of effusive events, thus also representing a useful tool for hazard management and risk reduction applications.

Assessing the long-term thermal signature at Vulcano Island, we identified an anomalous increase of the radiative power since August 2021, in large agreement with ground-based observations. These variations were detected weeks prior to the DPC raised the alert level from green to yellow. Radiant power trends were consistent with the unrest dynamics throughout the whole investigated period, highlighting the usefulness of our approach for tracking the evolution of volcanic unrests and measuring the heat sourced by hydrothermal systems. Similarly, by investigating the long-term thermal behaviour at Mt. Agung, we detected, in September 2017, an escalation in thermal activity three days prior to the Indonesian authorities raising the alert level from green to yellow. We also showed how the satellite-derived radiative power output was in remarkable agreement with the unrest and eruption timeline, and how variations in the thermal regime were consistent with both raising and lowering of the alert level throughout the whole investigated period. Furthermore, investigating the 2021 eruption at La Palma Island, we demonstrated the accuracy of TIRVolcH in locating the position of the further extending lava front(s), providing detailed measurements of the average flow front advancement velocity. Together, this information corroborates the applicability of the algorithm during major eruptive crises, providing, in a timely and accurate manner,

supporting information to competent bodies and stakeholders to respond to eruptive events.

Overall, the long-term cross-validation of VIIRS-derived radiative power, both in terms of trends and magnitude, as well as on geospatial accuracy, supports the veracity of our data. As such, we envisage that TIRVolcH-processed thermal information acquired at an unprecedented high temporal resolution will prove instrumental for detecting early signs of volcanic activity and for monitoring the evolution of thermal emissions, from unrest to eruption, at volcanoes worldwide.

At the time of writing, we continue to grow the number of monitored volcanoes. Current work is being conducted to assess the capabilities of TIRVolcH for quantifying thermal emissions at large and active crater lakes such as Poás (Costa Rica), Ruapehu (New Zealand), Ijen (Indonesia) (i.e., Aveni et al., 2024), and at large hydrothermal systems such as Campi Flegrei (Italy) and Yellowstone (USA).

Further studies are also being carried out to better interpret TIR thermal information, compiling statistically robust multidecadal thermal datasets, and assess this information against MIR-derived radiative power databases (i.e., Wright, 2016; Coppola et al., 2023), with the aim of providing novel insights and new perspectives into volcano monitoring. Finally, we envisage that the algorithm may be adapted, applied, and extended to present and forthcoming missions featuring high-resolution TIR instruments (see Supplementary Material S6 for a comprehensive list), such as the Global Change Observation Mission - Climate "SHIKISAI" (GCOM-C; Tanaka et al., 2010, Tanaka et al., 2014), the Surface Biology and Geology (SBG; Shreevastava et al., 2023, Thompson et al., 2023), the Thermal infraRed Imaging Satellite for High-resolution Natural resource Assessment (TRISHNA; Lagouarde et al., 2018, Buffet et al., 2021, Roujean et al., 2021, Vidal et al., 2022), and the VULCAIN mission (Buongiorno et al., 2023).

Funding

CRediT authorship contribution statement

S. Aveni: Writing – original draft, Visualization, Validation, Supervision, Software, Methodology, Investigation, Formal analysis, Data curation, Conceptualization. **M. Laiolo:** Writing – review & editing, Software, Resources, Conceptualization. **A. Campus:** Writing – review & editing, Software. **F. Massimetti:** Writing – review & editing. **D. Coppola:** Writing – review & editing, Validation, Supervision, Software, Resources, Project administration, Methodology, Formal analysis, Data curation, Conceptualization.

Declaration of competing interest

The authors declare no conflict of interest.

Data availability

Data will be made available on request.

Acknowledgments

Appendix A. Supplementary data

Supplementary data to this article can be found online at https://doi.org/10.1016/j.rse.2024.114388.

References

Amonte, C., Melián, G.V., Asensio-Ramos, M., Pérez, N.M., Padrón, E., Hernández, P.A., D'Auria, L., 2022. Hydrogeochemical temporal variations related to the recent volcanic eruption at the cumbre Vieja Volcano, La Palma, Canary Islands. Front. Earth Sci. 10, 1003890. https://doi.org/10.3389/feart.2022.1003890.

Andaru, R., Rau, J.Y., 2019. Lava dome changes detection at Agung mountain during high level of volcanic activity using UAV photogrammetry. Int. Arch. Photogramm. Remote. Sens. Spat. Inf. Sci. 42, 173–179. https://doi.org/10.5194/isprs-archives-XLII-2-W13-173-2019.

Andaru, et al., 2021. The use of UAV remote sensing for observing lava dome emplacement and areas of potential lahar hazards: An example from the 2017–2019 eruption crisis at Mount Agung in Bali Journal of Volcanology and Geothermal Research Volume 415, July 2021, 107255. https://doi.org/10.1016/j.jvolgeores.2021.107255.

Ardianto, A., Nugraha, A.D., Afif, H., Syahbana, D.K., Sahara, D.P., Zulfakriza, Z., Widiyantoro, S., Priyono, A., Rosalia, S., Saepuloh, A., Kasbani, K., Muttaqy, F., Rahsetyo, P.P., Priambodo, I.C., Martanto, M., 2021. Imaging the subsurface structure of Mount Agung in Bali (Indonesia) using volcano-tectonic (VT) earthquake tomography. Front. Earth Sci. 9, 619587. https://doi.org/10.3389/feart.2021.619587.

Auker, M.R., Sparks, R.S.J., Siebert, L., et al., 2013. A statistical analysis of the global historical volcanic fatalities record. J. Appl. Volcanol. 2, 2. https://doi.org/10.1186/2191-5040-2-2.

Aveni, S., Blackett, M., 2022. The first evaluation of the FY-3D/MERSI-2 sensor's thermal infrared capabilities for deriving land surface temperature in volcanic regions: a case study of Mount Etna. Int. J. Remote Sens. 43, 2777–2792. https://doi.org/10.1080/01431161.2022.2068360.

Aveni, S., Laiolo, M., Campus, A., Massimetti, F., Coppola, D., 2023. The capabilities of FY-3D/MERSI-II sensor to detect and quantify thermal volcanic activity: the 2020–2023 Mount Etna case study. Remote Sens. 15, 2528. https://doi.org/10.3390/rs15102528.

Aveni, S., Laiolo, M., Campus, A., Massimetti, F., Coppola, D., 2024. A single band TIR-based algorithm to detect low-to-high thermal anomalies in volcanic regions. In: EGU General Assembly 2024, Vienna, Austria, 14–19 Apr 2024, EGU24–9052, p. 2024. https://doi.org/10.5194/egusphere-egu24-9052.

Ball, M., Pinkerton, H., 2006. Factors affecting the accuracy of thermal imaging cameras in volcanology. J. Geophys. Res. Solid Earth 111 (2006), 1–14. https://doi.org/10.1029/2005JB003829.

Barberi, F., Neri, G., Valenza, M., Villari, L., 1991. 1987–1990 unrest at Vulcano. Acta Vulcanol. 1, 95–106.

Beccaro, L., Albano, M., Tolomei, C., Spinetti, C., Pezzo, G., Palano, M., Chiarabba, C., 2023. Insights into post-emplacement lava flow dynamics at Mt. Etna volcano from 2016 to 2021 by synthetic aperture radar and multispectral satellite data. Front. Earth Sci. 11, 1211450. https://doi.org/10.3389/feart.2023.1211450.

Bemelmans, M.J.W., Biggs, J., Poland, M., Wookey, J., Ebmeier, S.K., Diefenbach, A.K., Syahbana, D., 2023. High-resolution InSAR reveals localized pre-eruptive deformation inside the crater of Agung volcano, Indonesia. J. Geophys. Res. Solid Earth 128, e2022JB025669. https://doi.org/10.1029/2022JB025669.

Benito, M.B., Alvarado, G.E., Marchamalo, M., et al., 2023. Temporal and spatial evolution of the 2021 eruption in the Tajogaite volcano (cumbre Vieja rift zone, La Palma, Canary Islands) from geophysical and geodetic parameter analyses. Nat. Hazards 118, 2245–2284. https://doi.org/10.1007/s11069-023-06090-y.

Biggs, J., Ebmeier, S.K., Aspinall, W.P., Lu, Z., Pritchard, M.E., Sparks, R.S.J., Mather, T. A., 2014. Global link between deformation and volcanic eruption quantified by satellite imagery. Nat. Commun. 5, 3471. https://doi.org/10.1038/ncomms4471.

Bignami, C., Chini, M., Amici, S., Trasatti, E., 2020. Synergic use of multi-sensor satellite data for volcanic hazards monitoring: the Fogo (Cape Verde) 2014–2015 effusive eruption. Front. Earth Sci. 8, 22. https://doi.org/10.3389/feart.2020.00022.

Birnbaum, J., Lev, E., Hernandez, P.A., Barrancos, J., Padilla, G.D., Asensio-Ramos, M., Calvo, D., Rodríguez, F., Pérez, N.M., D'Auria, L., Calvari, S., 2023. Temporal variability of explosive activity at Tajogaite volcano, Cumbre Vieja (Canary Islands), 2021 eruption from ground-based infrared photography and videography. Front. Earth Sci. 11, 1193436. https://doi.org/10.3389/feart.2023.1193436.

Blackett, M., 2013. Review of the utility of infrared remote sensing for detecting and monitoring volcanic activity with the case study of shortwave infrared data for lascar volcano from 2001-2005. Geol. Soc. Lond. Spec. Publ. 380 (1), 107–135. https://doi.org/10.1144/SP380.10.

Blackett, M., 2014. Early analysis of Landsat-8 thermal infrared sensor imagery of volcanic activity. Remote Sens. 6, 2282–2295. https://doi.org/10.3390/rs6032282.

Blackett, M., 2017. An overview of infrared remote sensing of volcanic activity. J. Imaging 3, 13. https://doi.org/10.3390/jimaging3020013.

Blackett, M., Wooster, M.J., 2011. Evaluation of SWIR-based methods for quantifying active volcano radiant emissions using NASA EOS-ASTER data. Geomat. Nat. Haz. Risk 2 (1), 51–78. https://doi.org/10.1080/19475705.2010.541501.

Bonaccorso, A., Aloisi, M., 2021. Tracking magma storage: new perspectives from 40 years (1980–2020) of ground deformation source modeling on Etna volcano. Front. Earth Sci. 9, 638742. https://doi.org/10.3389/feart.2021.638742.

Bonadonna, C., Pistolesi, M., Biass, S., Voloschina, M., Romero, J., Coppola, D., et al., 2022. Physical characterization of long-lasting hybrid eruptions: the 2021 Tajogaite eruption of cumbre Vieja (La Palma, Canary Islands). J. Geophys. Res. Solid Earth 127, e2022JB025302. https://doi.org/10.1029/2022JB025302.

Braddock, M., Biggs, J., Watson, I.M., Hutchison, W., Pyle, D.M., Mather, T.A., 2017. Satellite observations of fumarole activity at Aluto volcano, Ethiopia: implications for geothermal monitoring and volcanic hazard. J. Volcanol. Geotherm. Res. 341, 70–83. https://doi.org/10.1016/j.jvolgeores.2017.05.006.

Briess, K., Jahn, H., Lorenz, E., Oertel, D., Skrbek, W., Zhukov, B., 2003. Fire recognition potential of the bi-spectral InfraRed detection (BIRD) satellite. Int. J. Remote Sens. 24 (4), 865–872. https://doi.org/10.1080/01431160210154010.

Brown, S.K., Auker, M.R., Sparks, R.S.J., 2015a. Global Volcanic Hazards and Risk, Populations around Holocene volcanoes and development of a Population Exposure Index. In: Loughlin, S.C., Sparks, S., Brown, S.K., Jenkins, S.F., Vye-Brown, C. (Eds.), Global Volcanic Hazards and Risk, Populations around Holocene volcanoes and development of a Population Exposure Index., pp. 223–232, 2015.

Brown, S.K., Loughlin, S., Sparks, R.S.J., Vye-Brown, C., 2015b. Global volcanic hazards and risk: Technical background paper for the Global Assessment Report on Disaster Risk Reduction 2015. United Nations Office for Disaster Risk Reduction.

Brown, S.K., Sparks, R.S.J., Mee, K., Vye-Brown, C., Ilyinskaya, E., Jenkins, S.F., and Loughlin, S.C.(2015c) Country and regional profiles of volcanic hazard and risk (Appendix B). In: S.C. Loughlin, R.S.J. Sparks, S.K.Brown, S.F. Jenkins & C. Vye-Brown (eds) Global Volcanic Hazards and Risk, Cambridge: CambridgeUniversity Press.

Buffet, L., Gamet, Philippe, Maisongrande, Philippe, Salcedo, Corinne, Crebassol, Philippe, 11 June 2021. The TIR instrument on TRISHNA satellite: a precursor of high resolution observation missions in the thermal infrared domain. In: Proc. SPIE 11852, International Conference on Space Optics — ICSO 2020, 118520Q. https://doi.org/10.1117/12.2599173.

Buongiorno, M.F., Lavagna, M.R., Labate, D., Tudor, S.V., Masini, A., De Carlo, P., Romaniello, V., Silvestri, M., Pirat, C., 2023. July. Vulcain: A Cubesat Mission for monitoring volcanoes and active thermal areas. In: IGARSS 2023–2023 IEEE International Geoscience and Remote Sensing Symposium. IEEE, pp. 265–267. https://doi.org/10.1109/IGARSS52108.2023.10282753.

Cabrera-Pérez, I., Soubestre, J., D'Auria, L., et al., 2023. Geothermal and structural features of La Palma island (Canary Islands) imaged by ambient noise tomography. Sci. Rep. 13, 12892. https://doi.org/10.1038/s41598-023-39910-z.

Calle, A., Casanova, J.-L., González-Alonso, F., 2009. Impact of point spread function of MSG-SEVIRI on active fire detection. Int. J. Remote Sens. 30 (17), 4567–4579. https://doi.org/10.1080/01431160802609726.

Calvari, S., Nunnari, G., 2022. Etna output rate during the last decade (2011−2022): insights for Hazard assessment. Remote Sens. 14, 6183. https://doi.org/10.3390/rs14236183.

Calvari, S., Di Traglia, F., Ganci, G., Giudicepietro, F., Macedonio, G., Cappello, A., Nolesini, T., Pecora, E., Bilotta, G., Centorrino, V., Corradino, C., Casagli, N., Del Negro, C., 2020. Overflows and pyroclastic density currents in March–April 2020 at Stromboli volcano detected by remote sensing and seismic monitoring data. Remote Sens. 12 (2020). https://doi.org/10.3390/RS12183010.

Campus, A., Laiolo, M., Massimetti, F., Coppola, D., 2022. The transition from MODIS to VIIRS for global volcano thermal monitoring. Sensors 22, 1713. https://doi.org/10.3390/s22051713.

Campus, A., Aveni, S., Laiolo, M., et al., 2024. Thermal unrest at La Fossa (Vulcano Island, Italy): the 2021–2023 VIIRS 375 m MIROVA-processed dataset. Bull. Volcanol. 86, 25. https://doi.org/10.1007/s00445-024-01721-z.

Cao, et al., 2014. Early on-orbit performance of the visible infrared imaging radiometer suite onboard the Suomi National Polar-Orbiting Partnership (S-NPP) satellite. In: IEEE Transactions on Geoscience and Remote Sensing, vol. 52. https://doi.org/10.1109/TGRS.2013.2247768. No. 2, February 2014.

Cao, C., Xiong, X., Wolfe, R., DeLuccia, F., Liu, Q., Blonski, S., Lin, G., Nishihama, M., Pogorzala, D., Oudrari, H., Hillger, D., 2013a. Visible infrared imaging radiometer suite (VIIRS) sensor data record (SDR) user's guide. Version 1.2 NOAA technical report NESDIS, 142. Available from: https://ncc.nesdis.noaa.gov/documents/documentation/viirs-users-guide-tech-report-142a-v1.2.pdf [Last accessed 30 November 2023].

Cao, C., Xiong, X., Wolfe, R., DeLuccia, F., Liu, Q., Blonski, S., Lin, G., Nishihama, M., Pogorzala, D., Oudrari, H., Hillger, D., 2013b. Visible infrared imaging radiometer suite (VIIRS) sensor data record (SDR) user's guide. Version 1.2 NOAA technical report NESDIS, 142. Available from: https://ncc.nesdis.noaa.gov/documents/documentation/viirs-users-guide-tech-report-142a-v1.2.pdf [Last accessed 30 November 2023].

Cao, C., Xiong, X., Wolfe, R., DeLuccia, F., Liu, Q., Blonski, S., Lin, G., Nishihama, M., Pogorzala, D., Oudrari, H., et al., 2017. (2017) Visible Infrared Imaging Radiometer Suite (VIIRS) Sensor Data Record (SDR) User's Guide, Version 1.3; NOAA Technical Report NESDIS. NESDIS, College Park, MD, USA. Available from: https://ncc.nesdis.noaa.gov/documents/documentation/viirs-users-guide-tech-report-142a-v1.3.pdf [Last accessed 30 November 2023].

Capasso, G., Inguaggiato, S., Nuccio, P.M., Pecoraino, G., Sortino, F., 1994. Chemical variations in the fumarolic gases of La Fossa di Vulcano crater. Acta Vulcanol. 4, 41–43.

Caputo, T., Bellucci Sessa, E., Silvestri, M., Buongiorno, M.F., Musacchio, M., Sansivero, F., Vilardo, G., 2019. Surface temperature multiscale monitoring by thermal infrared satellite and ground images at Campi Flegrei volcanic area (Italy). Remote Sens. 11, 1007. https://doi.org/10.3390/rs11091007.

Carn, S.A., Fioletov, V.E., McLinden, C.A., Li, C., Krotkov, N.A., 2017. A decade of global volcanic SO2 emissions measured from space. Sci. Rep. 7 (2017), 44095. https://doi.org/10.1038/srep44095.

Carracedo, J.C., Day, S., Guillou, H., Badiola, E.R., Cañas, J.A., Torrado, F.P., 1998. Hotspot volcanism close to a passive continental margin: the Canary Islands. Geol. Mag. 135 (5), 591–604. https://doi.org/10.1017/S0016756898001447.

Carracedo, J.C., Badiola, E.R., Guillou, H., de La Nuez, J., Torrado, F.P., 2001. Geology and volcanology of la Palma and el Hierro, western Canaries. Estudios Geol.-Madrid 57, 175–273. https://doi.org/10.3989/egeol.01575-6134.

Carracedo, J.C., Troll, V.R., Day, J.M.D., Geiger, H., Aulinas, M., Soler, V., Deegan, F.M., Perez-Torrado, F.J., Gisbert, G., Gazel, E., Rodriguez-Gonzalez, A., Albert, H., 2022. The 2021 eruption of the Cumbre Vieja volcanic ridge on La Palma, Canary Islands. Geology Today 38, 94–107. https://doi.org/10.1111/gto.12388.

Carter, A., Ramsey, M., 2010. Long-term volcanic activity at Shiveluch volcano: nine years of ASTER Spaceborne thermal infrared observations. Remote Sens. 2, 2571–2583. https://doi.org/10.3390/rs2112571.

Casillas Ruiz, R., Nuez Pestana, J.D.L., Fernández Rodríguez, C., Colmenero, J.R., Jourdan, F., Harangi, S., Lukács, M., 2020. Edad de las rocas volcánicas submarinas y plutónicas del Complejo Basal de La Palma: Implicaciones en la evolución geológica temprana de la isla. https://sge.usal.es/archivos/geogacetas/geo67/Geo67_p47_50.pdf.

Castro, J.M., Feisel, Y., 2022. Eruption of ultralow-viscosity basanite magma at cumbre Vieja, La Palma, Canary Islands. Nat. Commun. 13, 3174. https://doi.org/10.1038/s41467-022-30905-4.

Chalik, C.A., et al., 2019. Detection of ground thermal anomaly under dense vegetation based on ASTER TIR images. IOP Conf. Ser.: Earth Environ. Sci. 254 012001. https://doi.org/10.1088/1755-1315/254/1/012001.

Chiodini, G., Cioni, R., Marini, L., Panichi, C., 1995. Origin of the fumarolic fluids of Vulcano Island, Italy, and implication for volcanic surveillance. Bull. Volcanol. 57, 99–110. https://doi.org/10.1007/BF00301400.

Chiodini, G., Frondini, F., Raco, B., 1996. Diffuse emission of CO2 from the Fossa crater, Vulcano island (Italy). Bull. Volcanol. 58, 41–50. https://doi.org/10.1007/s004450050124.

Chu, S.S., Zhu, L., Sun, H.F., Li, Q.W., Zhang, X.R., Chen, T.T., Qiao, L., Zhu, W.R., Zhao, D.X., Zhang, Y.H., 2020. Automated volcanic hot-spot detection based on FY-4A/AGRI infrared data. Int. J. Remote Sens. 41 (6), 2410–2438. https://doi.org/10.1080/01431161.2019.1688887.

Civico, R., Ricci, T., Scarlato, P., Taddeucci, J., Andronico, D., Del Bello, E., D'Auria, L., Hernández, P.A., Pérez, N.M., 2022. High-resolution digital surface model of the 2021 eruption deposit of cumbre Vieja volcano, La Palma, Spain. Sci. Data 9 (1), 435. https://doi.org/10.1038/s41597-022-01551-8.

Copernicus Emergency Management Service, 2024. Directorate Space, Security and Migration, European Commission Joint Research Centre (EC JRC). Accessed April 27, 2024. https://emergency.copernicus.eu/.

Coppola, D., Staudacher, T., Cigolini, C., 2005. The may-July 2003 eruption at piton de la Fournaise (La Reunion): volume, effusion rates, and emplacement mechanisms inferred from thermal imaging and global positioning system (GPS) survey. Special Papers-Geol. Soc. Am. 396, 103. https://doi.org/10.1130/0-8137-2396-5.103.

Coppola, D., Piscopo, D., Staudacher, T., Cigolini, C., 1 July 2009. Lava discharge rate and effusive pattern at Piton de la Fournaise from MODIS data. J. Volcanol. Geotherm. Res. 184 (1–2), 174–192. https://doi.org/10.1016/j.jvolgeores.2008.11.031.

Coppola, D., James, M.R., Staudacher, T., Cigolini, C., 2010. A comparison of field-and satellite-derived thermal flux at piton de la Fournaise: implications for the calculation of lava discharge rate. Bull. Volcanol. 72, 341–356. https://doi.org/10.1007/s00445-009-0320-8.

Coppola, D.D., Piscopo, M., Laiolo, C., Cigolini, D., Donne, Delle, Ripepe, M., 2012. Radiative heat power at Stromboli Volcano during 2000–2011: twelve years of MODIS observations. J. Volcanol. Geotherm. Res. 215, 48–60. https://doi.org/10.1016/j.jvolgeores.2011.12.001.

Coppola, D., Laiolo, M., Delle Donne, D., Ripepe, M., Cigolini, C., 2014. Hot-spot detection and characterization of strombolian activity from MODIS infrared data. Int. J. Remote Sens. 35 (9), 3403–3426. https://doi.org/10.1080/01431161.2014.903354.

Coppola, D., Macedo, O., Ramos, D., Finizola, A., Delle Donne, D., Del Carpio, J., White, R., McCausland, W., Centeno, R., Rivera, M., Apaza, F., 2015. Magma extrusion during the Ubinas 2013–2014 eruptive crisis based on satellite thermal imaging (MIROVA) and ground-based monitoring. J. Volcanol. Geotherm. Res. 302, 199–210. https://doi.org/10.1016/j.jvolgeores.2015.07.005.

Coppola, D.M., Laiolo, C., Cigolini, D., Delle, D., Ripepe, M., 2016a. Enhanced volcanic hot-spot detection using MODIS IR data: results from the MIROVA system. Geol. Soc. Lond. Spec. Publ. 426, 181–205. https://doi.org/10.1144/sp426.5.

Coppola, D.M., Laiolo, C., Cigolini, D., Delle, D., Ripepe, M., 2016b. Enhanced volcanic hot-spot detection using MODIS IR data: results from the MIROVA system. Geol. Soc. Lond. Spec. Publ. 426, 181–205. https://doi.org/10.1144/sp426.5.

Coppola, D., Laiolo, M., Cigolini, C., Massimetti, F., Delle Donne, D., Ripepe, M., Arias, H., Barsotti, S., Parra, C.B., Centeno, R.G., Cevuard, S., Chigna, G., Chun, C., Garaebiti, E., Gonzales, D., Griswold, J., Juarez, J., Lara, L.E., López, C.M., Macedo, O., Mahinda, C., Ogburn, S., Prambada, O., Ramon, P., Ramos, D., Peltier, A., Saunders, S., de Zeeuw-van, Dalfsen E., Varley, N., William, R., 2020. Thermal remote sensing for global volcano monitoring: experiences from the MIROVA system. Front. Earth Sci. 7, 362. https://doi.org/10.3389/feart.2019.00362.

Coppola, D., Laiolo, M., Massimetti, F., et al., 2021. Thermal remote sensing reveals communication between volcanoes of the Klyuchevskoy Volcanic Group. Sci. Rep. 11, 13090. https://doi.org/10.1038/s41598-021-92542-z#.

Coppola, D., Laiolo, M., Campus, A., Massimetti, F., 2022. Thermal unrest of a fumarolic field tracked using VIIRS imaging bands: the case of La fossa crater (Vulcano Island, Italy). Front. Earth Sci. 10, 964372. https://doi.org/10.3389/feart.2022.964372.

Coppola, D., Cardone, D., Laiolo, M., Aveni, S., Campus, A., Massimetti, F., 2023. Global radiant flux from active volcanoes: the 2000–2019 MIROVA database. Front. Earth Sci. 11, 1240107. https://doi.org/10.3389/feart.2023.1240107.

Corradino, C., Ganci, G., Bilotta, G., Cappello, A., Del Negro, C., Fortuna, L., 2019. Smart decision support Systems for Volcanic Applications. Energies 12, 1216. https://doi.org/10.3390/en12071216.

Corradino, C., Ramsey, M.S., Pailot-Bonnétat, S., Harris, A.J.L., Negro, C.D., 2023. Detection of subtle thermal anomalies: deep learning applied to the ASTER global volcano dataset. IEEE Trans. Geosci. Remote Sens. 61, 1–15. https://doi.org/10.1109/TGRS.2023.3241085. Art no. 5000715.

D'Auria, L., Koulakov, I., Prudencio, J., Cabrera-Pérez, I., Ibáñez, J.M., Barrancos, J., García-Hernández, R., Martínez van Dorth, D., Padilla, G.D., Przeor, M., Ortega, V., 2022. Rapid magma ascent beneath La Palma revealed by seismic tomography. Sci. Rep. 12 (1), 17654. https://doi.org/10.1038/s41598-022-21818-9.

De Astis, G., Lucchi, F., Dellino, P., La Volpe, L., Tranne, C.A., Frezzotti, M.L., et al., 2013. Chapter 11 Geology, volcanic history and petrology of Vulcano (central Aeolian archipelago). Memoirs 37, 281–349. https://doi.org/10.1144/m37.11.

de Bremond, d'Ars J., Gibert, D., 2022. Low-temperature hydrothermal systems response to rainfall forcing: an example from temperature time series of fumaroles at La Soufrière de Guadeloupe volcano. Front. Earth Sci. 9, 772176. https://doi.org/10.3389/feart.2021.772176.

Dehn, J., Dean, K.G., Engle, K., Izbekov, P., 2002. Thermal precursors in satellite images of the 1999 eruption of Shishaldin Volcano. Bull. Volcanol. 64, 525–534. https://doi.org/10.1007/s00445-002-0227-0.

Delgado, F., Poland, M., Biggs, J., Ebmeier, S., Sansosti, E., Lundgren, P., et al., 2019. lessons learned from the ceos volcano pilot in latin american and the ongoing volcano demonstrator project. Geophys. Res. Abstr. 21. EGU2019-EGU14981. https://meetingorganizer.copernicus.org/EGU2019/EGU2019-14981.pdf.

Di Traglia, F., Bruno, V., Casu, F., Cocina, O., De Luca, C., Giudicepietro, F., et al., 2023. Multi-temporal InSAR, GNSS and seismic measurements reveal the origin of the 2021 Vulcano Island (Italy) unrest. Geophys. Res. Lett. 50, e2023GL104952. https://doi.org/10.1029/2023GL104952.

Diliberto, I.S., 2017. Long-term monitoring on a closed-conduit volcano: A 25 year long time-series of temperatures recorded at La Fossa cone (Vulcano island, Italy), ranging from 250 °C to 520 °C. J. Volcanol. Geotherm. Res. 346, 151–160. https://doi.org/10.1016/j.jvolgeores.2017.03.005.

Diliberto, I.S., Cangemi, M., Gagliano, A.L., Inguaggiato, S., Jacome Paz, Madonia, P., et al., 2021. Volcanic gas hazard assessment in the Baia di Levante area (Vulcano Island, Italy) inferred by geochemical investigation of passive fluid degassing. Geosciences 11 (11), 478. https://doi.org/10.3390/geosciences11110478.

Dipartimento della Protezione Civile (DPC), 2021. STATO DI ATTIVITÀ E LIVELLI DI ALLERTA DELL'ISOLA DI VULCANO Rapporto di sintesi della riunione tecnica straordinaria del 30/09/2021 Rapporto n. 9/2021. Issued: 01/10/2021. Available from: https://cme.ingv.it/images/rapporto-sintesi-del-30-settembre-2021-riunione-tecnica-vulcano-stato-attivita-e-livelli-allerta.pdf [Last accessed 19/01/2024].

Donovan, A., Oppenheimer, C., Bravo, M., 2012. Science at the policy interface: volcano-monitoring technologies and volcanic hazard management. Bull. Volcanol. 74, 1005–1022. https://doi.org/10.1007/s00445-012-0581-5.

Ebmeier, S.K., Andrews, B., Araya, M.C., Arnold, D.W.D., Biggs, J., Cooper, C., et al., 2018. Synthesis of global volcano deformation observations: implications for volcano monitoring and the lateral extent of magmatic systems. J. Appl. Volcanol. 7, 2. https://doi.org/10.1186/s13617-018-0071-3.

Ellam, R.M., Hawkesworth, C.J., Menzies, M.A., Rotgers, N.W., 1989. The volcanism of southern Italy: role of subduction and the relationship between potassic and sodic alkaline magmatism. J. Geophys. Res. 94, 4589–4601. https://doi.org/10.1029/JB094iB04p04589.

European Commission, Joint Research Centre (JRC), 2021. Volcano eruption in La Palma, Spain (2021-09-19). European Commission, Joint Research Centre (JRC) [Dataset] PID. http://data.europa.eu/89h/6fc2d36e-890c-47b8-9f5f-662816238678.

Federico, C., Cocina, O., Gambino, S., Paonita, A., Branca, S., Coltelli, M., Italiano, F., Bruno, V., Caltabiano, T., Camarda, M., et al., 2023. Inferences on the 2021 ongoing volcanic unrest at Vulcano Island (Italy) through a comprehensive multidisciplinary surveillance network. Remote Sens. 15, 1405. https://doi.org/10.3390/rs15051405.

Flynn, L.P., Mouginis-Mark, P.J., Gradie, J.C., Lucey, P.G., 1993. Radiative temperature measurements at Kupaianaha lava lake, Kilauea Volcano, Hawaii. J. Geophys. Res. Solid Earth 98 (B4), 6461–6476. https://doi.org/10.1029/92JB02698.

Ganci, G., Vicari, A., Cappello, A., Del Negro, C., 2012a. An emergent strategy for volcano hazard assessment: from thermal satellite monitoring to lava flow modeling. Remote Sens. Environ. 119, 197–207. https://doi.org/10.1016/j.rse.2011.12.021.

Ganci, G., Harris, A.J.L., Del Negro, C., Guehenneux, Y., Cappello, A., Labazuy, P., Calvari, S., Gouhier, M., 2012b. A year of lava fountaining at Etna: volumes from SEVIRI. Geophys. Res. Lett. 39, L06305. https://doi.org/10.1029/2012GL051026.

Ganci, G., Cappello, A., Bilotta, G., Del Negro, C., 2020. How the variety of satellite remote sensing data over volcanoes can assist hazard monitoring efforts: the 2011 eruption of Nabro volcano. Remote Sens. Environ. 236, 111426. https://doi.org/10.1016/j.rse.2019.111426.

Ganci, G., Bilotta, G., Zuccarello, F., Calvari, S., Cappello, A., 2023. A multi-sensor satellite approach to characterize the volcanic deposits emitted during Etna's lava fountaining: the 2020–2022 study case. Remote Sens. 15, 916. https://doi.org/10.3390/rs15040916.

Garcia, C., Fearnley, C.J., 2012. Evaluating critical links in early warning systems for natural hazards. Environ. Hazards 11 (2), 123–137. https://doi.org/10.1080/17477891.2011.609877.

Genzano, N., Pergola, N., Marchese, F., 2020. A (2020) Google earth engine tool to investigate, map and monitor volcanic thermal anomalies at global scale by means of mid-high spatial resolution satellite data. Remote Sens. 12, 3232. https://doi.org/10.3390/rs12193232.

Gaudin, D., Finizola, A., Delcher, E., Beauducel, F., Allemand, P., Delacourt, C., et al., 2015. Influence of Rainfalls on Heat and Steam Fluxes of Fumarolic Zones: Six Months Records along the Ty Fault (Soufrière of Guadeloupe, Lesser Antilles). J. Volcanology Geothermal Res. 302, 273–285. https://doi.org/10.1016/j.jvolgeores.2015.06.015.

Genzano, N., Marchese, F., Neri, M., Pergola, N., Tramutoli, V., 2021. (2021) implementation of robust satellite techniques for volcanoes on ASTER data under the Google earth engine platform. Appl. Sci. 11, 4201. https://doi.org/10.3390/app11094201.

Genzano, N., Marchese, F., Plank, S., Pergola, N., 2023. Monitoring the Mauna Loa (Hawaii) eruption of November–December 2022 from space: results from GOES-R, Sentinel-2 and Landsat-8/9 observations. Int. J. Appl. Earth Obs. Geoinf. 122 (August 2023), 103388. https://doi.org/10.1016/j.jag.2023.103388.

Global Volcanism Program, 1989. Report on Agung (Indonesia). In: McClelland, L. (Ed.), Scientific Event Alert Network Bulletin, 14:7. Smithsonian Institution. https://doi.org/10.5479/si.GVP.SEAN198907-264020.

Global Volcanism Program, 2018. Report on Agung (Indonesia). In: Crafford, A.E., Venzke, E. (Eds.), Bulletin of the Global Volcanism Network, 43:8. Smithsonian Institution. https://doi.org/10.5479/si.GVP.BGVN201808-264020.

Global Volcanism Program, 2019. Report on Agung (Indonesia). In: Crafford, A.E., Venzke, E. (Eds.), Bulletin of the Global Volcanism Network, 44:6. Smithsonian Institution. https://doi.org/10.5479/si.GVP.BGVN201906-264020.

Global Volcanism Program, 2021. Report on La Palma (Spain). In: Crafford, A.E., Venzke, E. (Eds.), Bulletin of the Global Volcanism Network, 46:10. Smithsonian Institution. https://doi.org/10.5479/si.GVP.BGVN202110-383010.

Global Volcanism Program, 2022. Report on La Palma (Spain). In: Bennis, K.L., Venzke, E. (Eds.), Bulletin of the Global Volcanism Network, 47:2. Smithsonian Institution. https://doi.org/10.5479/si.GVP.BGVN202202-383010.

Global Volcanism Program, 2023. (Database) Volcanoes of the World; v. 5.0.2; 23 January 2023. Smithsonian Institution, Washington, DC, USA. https://doi.org/10.5479/si.GVP.VOTW5-2024.5.2 compiled by Venzke, E.

Gobierno de Canarias, 2023. Erupción volcánica en la isla de la palma: Evolución de la colada de lava entre las días 19 de septiembre y 1 de Octubre. Available from. https://www.gobiernodecanarias.org/cmsweb/export/sites/infovolcanlapalma/galerias/documentos/evolucion-coladas/Evolucion_colada_Batimetria_1Oct.pdf [Last accessed 27 April 2024].

Goldberg, M., 2018. The joint polar satellite system overview. In: Proceedings of the IGARSS 2018–2018 IEEE International Geoscience and Remote Sensing Symposium, Valencia, Spain, 22–27 July 2018. https://doi.org/10.1109/IGARSS.2018.8518787.

Granieri, D., Avino, R., Carapezza, M.L., Chiodini, G., Ranaldi, M., Ricci, T., et al., 2006. Correlated increase in CO2 fumarolic content and diffuse emission from La Fossa crater (Vulcano, Italy): Evidence of volcanic unrest or increasing gas release from a stationary deep magma body? Geophys. Res. Lett. 33, L13316. https://doi.org/10.1029/2006GL026460.

Gray, D.M., Burton-Johnson, A., Fretwell, P.T., 2019. Evidence for a lava lake on Mt. Michael volcano, Saunders Island (South Sandwich Islands) from Landsat, Sentinel-2 and ASTER satellite imagery. J. Volcanol. Geotherm. Res. https://doi.org/10.1016/j.jvolgeores.2019.05.002.

Gudmundsson, G., 2011. 'Respiratory health effects of volcanic ash with special reference to Iceland'. A review. Clin. Resp. J. 5 (Issue 1), 2–9. https://doi.org/10.1111/j.1752-699X.2010.00231.x.

Guerrieri, L., Corradini, S., Theys, N., Stelitano, D., Merucci, L., 2023. Volcanic clouds characterization of the 2020–2022 sequence of Mt. Etna Lava Fountains using MSG-SEVIRI and products' cross-comparison. Remote Sens. (15), 2055. https://doi.org/10.3390/rs15082055.

Guillou, H., Carracedo, J.C., Day, S.J., 1998. Dating of the upper Pleistocene–Holocene volcanic activity of La Palma using the unspiked K–Ar technique. J. Volcanol. Geotherm. Res. 86 (1–4), 137–149. https://doi.org/10.1016/S0377-0273(98)00074-2.

Gunawan, M.T., Kusnandar, R., Supendi, P., et al., 2020. Analysis of swarm earthquakes around Mt. Agung Bali, Indonesia prior to November 2017 eruption using regional BMKG network. Geosci. Lett. 7 (14). https://doi.org/10.1186/s40562-020-00163-7.

Gurrieri, S., Di Martino, R.M.R., Camarda, M., Francofonte, V., 2023. Monitoring CO2 hazards of volcanic origin: a case study at the island of Vulcano (Italy) during 2021–2022. Geosciences 13, 266. https://doi.org/10.3390/geosciences13090266.

Hansell, A.L., Horwell, C.J., Oppenheimer, C., 2006. The health hazards of volcanoes and geothermal areas Occup. Environ. Med. 63 (Issue 2), 149–156. https://doi.org/10.1136/oem.2005.022459.

Harris, A.J.L., 1996. Low Spatial Resolution Thermal Monitoring of Volcanoes from Space. PhD thesis. Open University, Milton Keynes. https://doi.org/10.21954/ou.ro.0000f7b7.

Harris, A., 2013. Thermal Remote Sensing of Active Volcanoes: A User's Manual. Cambridge University Press, Cambridge, UK. https://doi.org/10.1017/CBO9781139029346.

Harris, A.J.L., Stevenson, D.S., 1997a. Thermal observations of degassing open conduits and fumaroles at Stromboli and Vulcano using remotely sensed data. J. Volcanol. Geotherm. Res. 76, 175–198. https://doi.org/10.1016/S0377-0273(96)00097-2.

Harris, A.J.L., Stevenson, D.S., 1997b. Magma budgets and steady-state activity of Vulcano and Stromboli. Geophys. Res. Lett. 24 (9), 1043–1046. https://doi.org/10.1029/97GL00861.

Harris, A.J.L., Blake, S., Rothery, D.A., Stevens, N.F., 1997. A chronology of the 1991 to 1993 Mount Etna eruption using advanced very high resolution radiometer data: implications for real-time thermal volcano monitoring. J. Geophys. Res. 102 (B4), 7985–8003. https://doi.org/10.1029/96JB03388.

Harris, A.J.L., Carn, S., Dehn, J., Del Negro, C., Guðmundsson, G., Cordonnier, B., et al., 2016. Conclusion: recommendations and findings of the red seed working group. Detecting, modelling and responding to effusive eruptions. Geol. Soc. Lond. Spec. Publ. 426, 567–648. https://doi.org/10.1144/SP426.11.

Harris, A.J., Villeneuve, N., Di Muro, A., Ferrazzini, V., Peltier, A., Coppola, D., Favalli, M., Bachèlery, P., Froger, J.L., Gurioli, L., Moune, S., 2017. Effusive crises at piton de la Fournaise 2014–2015: a review of a multi-national response model. J. Appl. Volcanol. 6 (1), 1–29. https://doi.org/10.1186/s13617-017-0062-9.

Harris, A.J.L., Chevrel, M.O., Coppola, D., Ramsey, M., Hrysiewicz, A., Thivet, S., et al., 2019. Validation of an integrated satellite-data-driven response to an effusive crisis: the April-May 2018 eruption of Piton de la fournaise. Ann. Geophys. 61, 2018. https://doi.org/10.4401/ag-7972.

Hellman, M.J., Ramsey, M., 2004. Analysis of hot springs and associated deposits in Yellowstone National Park using ASTER and AVIRIS remote sensing. J. Volcanol. Geotherm. Res. 135 (1–2), 195–219. https://doi.org/10.1016/j.jvolgeores.2003.12.012.

Henderson, S.T., Pritchard, M.E., Cooper, J.R., Aoki, Y., 2019. Remotely sensed deformation and thermal anomalies at mount pagan, Mariana Islands. Front. Earth Sci. 7, 238. https://doi.org/10.3389/feart.2019.00238.

Henney, L.A., 2012. Remote sensing of volcanic plumes using the Advanced Spaceborne Thermal Emission and Reflection Radiometer (ASTER), 2012. Dissertation, Michigan Technological University. https://doi.org/10.37099/mtu.dc.etds/323.

Hidayat, T., Mahasena, P., Dermawan, B., Hadi, T.W., Premadi, P.W., Herdiwijaya, D., December 2012. Clear sky fraction above Indonesia: an analysis for astronomical site selection. Mon. Not. R. Astron. Soc. 427 (3), 1903–1917. https://doi.org/10.1111/j.1365-2966.2012.22000.x.

Hilman, Z., Saepuloh, A., Susanto, V., 2020. Application of land surface temperature derived from ASTER TIR to identify volcanic gas emission around Bandung basin. Int. J. Remote Sens. Earth Sci. 16, 179. https://doi.org/10.30536/j.ijreses.2019.v16.a3254.

Horwell, C.J., Baxter, P.J., 2006. The respiratory health hazards of volcanic ash: a review for volcanic risk. Mitigation Bull. Volcanol. 69 (Issue 1), 1–24. https://doi.org/10.1007/s00445-006-0052-y.

Hyman, D.M.R., Dietterich, H.R., Patrick, M.R., 2022. Toward next-generation lava flow forecasting: development of a fast, physics-based lava propagation model. J. Geophys. Res. Solid Earth 127, e2022JB024998. https://doi.org/10.1029/2022JB024998.

Inguaggiato, S., Vita, F., Diliberto, I.S., Mazot, A., Calderone, L., Mastrolia, A., et al., 2022a. The extensive parameters as a tool to monitoring the volcanic activity: the case study of Vulcano island (Italy). Remote Sens. 14, 1283. https://doi.org/10.3390/rs14051283.

Inguaggiato, S., Vita, F., Diliberto, I.S., et al., 2022b. The volcanic activity changes occurred in the 2021–2022 at Vulcano island (Italy), inferred by the abrupt variations of soil CO2 output. Sci. Rep. 12 (2022), 21166. https://doi.org/10.1038/s41598-022-25435-4.

Inguaggiato, S., Liotta, M., Rouwet, D., Tassi, F., Vita, F., Schiavo, B., Ono, S., Keller, N. S., 2023. Sulfur origin and flux variations in fumarolic fluids of Vulcano Island, Italy. Front. Earth Sci. 11, 1197796. https://doi.org/10.3389/feart.2023.1197796.

INGV weekly Reports, 2022a. Bollettino settimanale Vulcano (20220531). Available at: https://cme.ingv.it/bollettini-e-comunicati/bollettini-settimanali-vulcano [Last accessed November 2023].

INGV weekly Reports, 2022b. Bollettino settimanale Vulcano (20220628). Available at: https://cme.ingv.it/bollettini-e-comunicati/bollettini-settimanali-vulcano [Last accessed November 2023].

Kaneko, T., Maeno, F., Yasuda, A., et al., 2019. (2019) the 2017 Nishinoshima eruption: combined analysis using Himawari-8 and multiple high-resolution satellite images. Earth Planets Space 71, 140. https://doi.org/10.1186/s40623-019-1121-8.

Keller, J., 1980. The island of Vulcano. Soc. Ital. Min. Petr. 36, 368–413. Available from: https://rruff.info/rdsmi/V36/RDSMI36_369.pdf [Last accessed November 2023].

Kervyn, M., Ernst, G.G.J., Harris, A.J.L., Belton, F., Mbede, E., Jacobs, P., 2008. Thermal remote sensing of the low-intensity carbonatite volcanism of Oldoinyo Lengai, Tanzania. Int. J. Remote Sens. 29 (22), 6467–6499. https://doi.org/10.1080/01431160802167105.

Klügel, A., Hoernle, K.A., Schmincke, H.U., White, J.D., 2000. The chemically zoned 1949 eruption on La Palma (Canary Islands): petrologic evolution and magma supply dynamics of a rift zone eruption. J. Geophys. Res. Solid Earth 105 (B3), 5997–6016. https://doi.org/10.1029/1999JB900334.

Kusumadinata, 1964. The eruption of the Agung volcano in Bali in 1963. In: Bull. Geol. Surv. Indonesia 1.1, (Notes), pp. 12–15.

Lacava, T., Kervyn, M., Liuzzi, M., Marchese, F., Pergola, N., Tramutoli, V., 2018. Assessing performance of the RSTVOLC multi-temporal algorithm in detecting subtle hot spots at Oldoinyo Lengai (Tanzania, Africa) for comparison with MODLEN. Remote Sens. 10, 1177. https://doi.org/10.3390/rs10081177.

Lagouarde, J.P., Bhattacharya, B.K., Crebassol, P., Gamet, P., Babu, S.S., Boulet, G., Briottet, X., Buddhiraju, K.M., Cherchali, S., Dadou, I., Dedieu, G., 2018. The Indian-French Trishna mission: earth observation in the thermal infrared with high spatio-temporal resolution. In: IGARSS 2018–2018 IEEE International Geoscience and Remote Sensing Symposium, Institute of Electrical and Electronics Engineers (IEEE). USA., Jul 2018, Valencia, Spain, pp. 4078–4081. https://doi.org/10.1109/IGARSS.2018.8518720.

Lara, L.E., Flores, F., Calderón, R., Cardona, C., 2021. Volcano hazards and risks in Chile Forecasting and Planning for Volcanic Hazards, Risks, and Disasters, pp. 617–633. https://doi.org/10.1016/b978-0-12-818082-2.00017-2.

Letourneur, L., 2008. Structure and Dynamics of Plumbing Systems of Oceanic Shield Volcanoes: An Example from Réunion Island. Unpublished PhD Thesis. Universität zu Göttingen, p. 145. Available from: http://hdl.handle.net/11858/00-1735-0000-0006-B273-3 [Last accessed November 2023].

Leys, C., Ley, C., Klein, O., Bernard, P., Licata, L., 2013. Detecting outliers: do not use standard deviation around the mean, use absolute deviation around the median. J. Exp. Soc. Psychol. 49 (4), 764–766. https://doi.org/10.1016/j.jesp.2013.03.013.

Lombardo, V., Musacchio, M., Buongiorno, M.F., 2012. Error analysis of subpixel lava temperature measurements using infrared remotely sensed data. Geophys. J. Int. 191 (1), 112–125. https://doi.org/10.1111/j.1365-246X.2012.05632.x. October 2012.

Loughlin, S.C., Vye-Brown, C., Sparks, R.S.J., et al., 2015. An introduction to global volcanic hazard and risk. In: Loughlin, S.C., Sparks, S., Brown, S.K., Jenkins, S.F., Vye-Brown, C. (Eds.), Volcanic Hazards and Risk. Cambridge University Press, pp. 1–80. https://doi.org/10.1017/CBO9781316276273.003.

Lowenstern, J.B., Ramsey, D.W., 2017. The volcano disaster assistance program—helping to save lives worldwide for more than 30 years. U.S. Geol. Survey Fact Sheet 6, 2017–3071. https://doi.org/10.3133/fs20173071.

Mannini, S., Harris, A.J.L., Jessop, D.E., Chevrel, M.O., Ramsey, M.S., 2019. Combining ground- and ASTER-based thermal measurements to constrain fumarole field heat budgets: the case of Vulcano Fossa 2000-2019. Geophys. Res. Lett. 46, 11868–11877. https://doi.org/10.1029/2019GL084013.

Marchese, F., Genzano, N., 2022. Global volcano monitoring through the normalized hotspot indices (NHI) system. J. Geol. Soc. Lond. 180. https://doi.org/10.1144/jgs2022-014.

Marchese, F., Genzano, N., Neri, M., Falconieri, A., Mazzeo, G., Pergola, N., 2019. A Multi-Channel algorithm for mapping volcanic thermal anomalies by means of Sentinel-2 MSI and Landsat-8 OLI data. Remote Sens. 11, 2876. https://doi.org/10.3390/rs11232876.

Markham, B.L., 1985. The Landsat sensors' spatial response. IEEE Trans. Geosci. Remote Sens. GE-23, 864–875. https://doi.org/10.1109/TGRS.1985.289472.

Marquez, M., Paredes, C., Llorente, M., 2022. Attempt to model lava flow faster than real time: an example of La Palma using VolcFlow. GeoHazards 3, 529–562. https://doi.org/10.3390/geohazards3040027.

Martín-Raya, N., Díaz-Pacheco, J., López-Díez, A., et al., 2023. A lava flow simulation experience oriented to disaster risk reduction, early warning systems and response during the 2021 volcanic eruption in Cumbre Vieja, La Palma. Nat. Hazards 117, 3331–3351. https://doi.org/10.1007/s11069-023-05989-w.

Massimetti, F., Coppola, D., Laiolo, M., Valade, S., Cigolini, C., Ripepe, M., 2020. Volcanic hot-spot detection using SENTINEL-2: a comparison with MODIS–MIROVA thermal data series. Remote Sens. 12, 820. https://doi.org/10.3390/rs12050820.

Mia, M.B., Nishijima, J., Fujimitsu, Y., 2014. Exploration and monitoring geothermal activity using Landsat ETM+ images: a case study at Aso volcanic area in Japan. J. Volcanol. Geotherm. Res. 275, 14–21. https://doi.org/10.1016/j.jvolgeores.2014.02.008.

Mia, M.B., Fujimitsu, Y., Nishijima, J., 2017. Thermal activity monitoring of an active volcano using Landsat 8/OLI-TIRS sensor images: a case study at the Aso volcanic area in Southwest Japan. Geosciences 7 (4), 118. https://doi.org/10.3390/geosciences7040118.

Mia, M.B., Fujimitsu, Y., Nishijima, J., 2018. Monitoring thermal activity of the Beppu geothermal area in Japan using multisource satellite thermal infrared data. Geosciences 8, 306. https://doi.org/10.3390/geosciences8080306.

Montalto, A., 1996. Signs of potential renewal of eruptive activity at La Fossa (Vulcano, Aeolian Islands). Bull. Volcanol. 57, 483–492. https://doi.org/10.1007/BF00304434.

Montesinos, F.G., Sainz-Maza, S., Gómez-Ortiz, D., Arnoso, J., Blanco-Montenegro, I., Benavent, M., Vélez, E., Sánchez, N., Martín-Crespo, T., 2023. Insights into the magmatic feeding system of the 2021 eruption at cumbre Vieja (La Palma, Canary Islands) inferred from gravity data modeling. Remote Sens. 15, 1936. https://doi.org/10.3390/rs15071936.

Morgan, H.A., Harris, A.J., Gurioli, L., 2013. Lava discharge rate estimates from thermal infrared satellite data for Pacaya volcano during 2004–2010. J. Volcanol. Geotherm. Res. 264, 1–11. https://doi.org/10.1016/j.jvolgeores.2013.07.008.

Murphy, S.M., de Souza Filho, C.R., Oppenheimer, C., 2011. Monitoring volcanic thermal anomalies from space: size matters. J. Volcanol. Geotherm. Res. 203, 48–61. https://doi.org/10.1016/j.jvolgeores.2011.04.008.

Nádudvari, Á., Abramowicz, A., Maniscalco, R., Viccaro, M., 2020. The estimation of lava flow temperatures using landsat night-time images: case studies from eruptions of Mt. Etna and Stromboli (Sicily, Italy), Kīlauea (Hawaii Island), and Eyjafjallajökull and Holuhraun (Iceland). Remote Sens. 12 (16), 2537. https://doi.org/10.3390/rs12162537.

Nishihama, M., Wolfe, R., Solomon, D., Patt, F., Blanchette, J., Fleig, A., Masuoka, E., 1997. MODIS level 1A earth location: Algorithm theoretical basis document, version 3.0. In: SDST-092. MODIS Science Data Support Team, Sioux Falls, SD, USA. Available from: https://modis.gsfc.nasa.gov/data/atbd/atbd_mod28_v3.pdf [Last accessed November 2023].

NOAA National Centers for Environmental Information, 2024. Monthly National Climate Report for Annual 2023. published online January 2024, retrieved on March 25, 2024 from. https://www.ncei.noaa.gov/access/monitoring/monthly-report/national/202313 [Last accessed March 2024].

Oudrari, H., McIntire, J., Xiong, X., Butler, J., Ji, Q., Schwarting, T., Lee, S., Efremova, B., 2016. JPSS-1 VIIRS radiometric characterization and calibration based on pre-launch testing. Remote Sens. 8, 41. https://doi.org/10.3390/rs8010041.

Padrón, E., Pérez, N.M., Melián, G.V., Sumino, H., Alonso, M., Recio, G., Asensio-Ramos, M., Rodríguez, F., D'Auria, L., 2021, April. Temporal evolution of 3He/4He isotopic ratio at Dos Aguas cold mineral spring, La Palma, Canary Islands. In: EGU General Assembly Conference Abstracts. (pp. EGU21-14994). https://doi.org/10.5194/egusphere-egu21-14994.

Pailot-Bonnétat, S., Rafflin, V., Harris, A., et al., 2023. Anatomy of thermal unrest at a hydrothermal system: case study of the 2021–2022 crisis at Vulcano. Earth Planets Space 75, 159. https://doi.org/10.1186/s40623-023-01913-5.

Pankhurst, M.J., Scarrow, J.H., Barbee, O.A., Hickey, J., Coldwell, B.C., Rollinson, G.K., Rodríguez-Losada, J.A., Lorenzo, A.M., Rodríguez, F., Hernández, W., Fernández, D. C., 2022. Rapid response petrology for the opening eruptive phase of the 2021 cumbre Vieja eruption, La Palma, Canary Islands. Volcanica 5 (1), 1–10. https://doi.org/10.30909/vol.05.01.0110.

Paonita, A., Federico, C., Bonfanti, P., Capasso, G., Inguaggiato, S., Italiano, F., et al., 2013. The episodic and abrupt geochemical changes at La Fossa fumaroles (Vulcano Island, Italy) and related constraints on the dynamics, structure, and compositions of the magmatic system. Geochim. Cosmochim. Acta 120, 158–178. https://doi.org/10.1016/j.gca.2013.06.015.

Patrick, M.R., Dehn, J., Dean, K., 2004. Numerical modeling of lava flow cooling applied to the 1997 Okmok eruption: approach and analysis. J. Geophys. Res. 109, B03202. https://doi.org/10.1029/2003JB002537.

Patrick, M.R., Dehn, J., Dean, K., 2005. Numerical modeling of lava flow cooling applied to the 1997 Okmok eruption: comparison with advanced very high resolution radiometer thermal imagery. J. Geophys. Res. 110, B02210. https://doi.org/10.1029/2003JB002538.

Pawlowicz, R., 2020. M_Map: A mapping package for MATLAB. version 1.4m, [Computer software] available online at www.eoas.ubc.ca/~rich/map.html [Last accessed November 2023].

Pieri, D., Abrams, M., 2004. (2004) ASTER watches the world's volcanoes: a new paradigm for volcanological observations from orbit. J. Volcanol. Geotherm. Res. 135 (1–2), 13–28. https://doi.org/10.1016/j.jvolgeores.2003.12.018.

Pieri, D., Abrams, M., 2005. ASTER observations of thermal anomalies preceding the April 2003 eruption of Chikurachki volcano, Kurile Islands. Russia. https://doi.org/10.1016/j.rse.2005.06.012.

Plank, S., Marchese, F., Filizzola, C., Pergola, N., Neri, M., Nolde, M., Martinis, S., 2019. The July/August 2019 Lava Flows at the Sciara del Fuoco, Stromboli–Analysis from Multi-Sensor Infrared Satellite Imagery. Remote Sens. 11 (23), 2879. https://doi.org/10.3390/rs11232879.

Plank, S., Massimetti, Francesco, Soldati, Arianna, Hess, Kai-Uwe, Nolde, Michael, Martinis, Sandro, Dingwell, Donald B., 2021. Estimates of lava discharge rate of 2018 Kīlauea volcano, Hawai'i eruption using multi-sensor satellite and laboratory measurements. Int. J. Remote Sens. 42 (4), 1492–1511. https://doi.org/10.1080/01431161.2020.1834165.

Plank, S., Shevchenko, A.V., d'Angelo, P., Gstaiger, V., González, P.J., Cesca, S., Martinis, S., Walter, T.R., 2023 Feb 4. Combining thermal, tri-stereo optical and bi-static InSAR satellite imagery for lava volume estimates: the 2021 cumbre Vieja eruption, La Palma. Sci. Rep. 13 (1), 2057. https://doi.org/10.1038/s41598-023-29061-6. PMID: 36739451; PMCID: PMC9899239.

Poland, Michael P., Anderson, K.R., 2020. Partly cloudy with a chance of lava flows: Forecasting volcanic eruptions in the twenty-first century. Journal of Geophysical Research: Solid Earth 125. https://doi.org/10.1029/2018JB016974 e2018JB016974.

Prata, A.J., 2009. Satellite detection of hazardous volcanic clouds and the risk to global air traffic. Nat. Hazards 51, 303–324. https://doi.org/10.1007/s11069-008-9273-z.

Pritchard, M.E., Simons, M., 2004a. Surveying volcanic arcs with satellite radar interferometry: the Central Andes, Kamchatka, and beyond. GSA Today 14 (8), 4–11. https://doi.org/10.1130/1052-5173(2004)014%3C4:svawsr%3E2.0.co;2.

Pritchard, M.E., Simons, M., 2004b. An InSAR-based survey of volcanic deformation in the Central Andes. Geochem. Geophys. Geosyst. 5, Q02002. https://doi.org/10.1029/2003GC000610.

Pritchard, M., Biggs, J., Wauthier, C., et al., 2018. Towards coordinated regional multi-satellite InSAR volcano observations: results from the Latin America pilot project. J. Appl. Volcanol. 7, 5. https://doi.org/10.1186/s13617-018-0074-0.

Proietti, C., De Beni, E., Cantarero, M., et al., 2023. Rapid provision of maps and volcanological parameters: quantification of the 2021 Etna volcano lava flows through the integration of multiple remote sensing techniques. Bull. Volcanol. 85, 58. https://doi.org/10.1007/s00445-023-01673-w.

Rabuffi, F., Silvestri, M., Musacchio, M., Romaniello, V., Buongiorno, M.F., 2022. A statistical approach to satellite time series analysis to detect changes in thermal activities: the Vulcano Island 2021 crisis. Remote Sens. 14, 3933. https://doi.org/10.3390/rs14163933.

Ramsey, M.S., 2016. Synergistic use of satellite thermal detection and science: a decadal perspective using ASTER. Geol. Soc. Lond. Spec. Publ. 426 (1), 115–136. https://doi.org/10.1144/sp426.23.

Ramsey, M., Dehn, J., 2004. Spaceborne observations of the 2000 Bezymianny, Kamchatka eruption: the integration of high-resolution ASTER data into near real-time monitoring using AVHRR. J. Volcanol. Geotherm. Res. 135 (2004), 127–146. https://doi.org/10.1016/j.jvolgeores.2003.12.014.

Ramsey, M.S., Flynn, I.T.W., 2020. The spatial and spectral resolution of ASTER infrared image data: a paradigm shift in Volcanological remote sensing. Remote Sens. 12, 738. https://doi.org/10.3390/rs12040738.

Ramsey, M.S., Harris, A.J., 2013. Volcanology 2020: how will thermal remote sensing of volcanic surface activity evolve over the next decade? J. Volcanol. Geotherm. Res. 249, 217–233. https://doi.org/10.1016/j.jvolgeores.2012.05.011.

Ramsey, M., Chevrel, M.O., Coppola, D., Harris, A.J., 2019. The influence of emissivity on the thermo-rheological modeling of the channelized lava flows at Tolbachik volcano. Ann. Geophys. 62 (2), VO222. https://doi.org/10.4401/ag-8077.

Ramsey, M.S., Corradino, C., Thompson, J.O., Leggett, T.N., 2023. Statistical retrieval of volcanic activity in long time series orbital data: implications for forecasting future activity. Remote Sens. Environ. 295, 113704. https://doi.org/10.1016/j.rse.2023.113704.

Reath, K.A., Ramsey, M.S., Dehn, J., Webley, P.W., 2016. Predicting eruptions from precursory activity using remote sensing data hybridization. J. Volcanol. Geotherm. Res. 321, 18–30. https://doi.org/10.1016/j.jvolgeores.2016.04.027.

Reath, K., Pritchard, M.E., Moruzzi, S., Alcott, A., Coppola, D., Pieri, D., 2019a. The AVTOD (ASTER volcanic thermal output database) Latin America archive. J. Volcanol. Geotherm. Res. 376, 62–74. https://doi.org/10.1016/j.jvolgeores.2019.03.019.

Reath, K., Pritchard, M., Poland, M., Delgado, F., Carn, S., Coppola, D., Andrews, B., Ebmeier, S.K., Rumpf, E., Henderson, S., Baker, S., 2019b. Thermal, deformation, and degassing remote sensing time series (CE 2000–2017) at the 47 most active volcanoes in Latin America: implications for volcanic systems. J. Geophys. Res. Solid Earth 124 (1), 195–218. https://doi.org/10.1029/2018JB016199.

Ricci, T., Finizola, A., Barde-Cabusson, S., Delcher, E., Alparone, S., Gambino, S., et al., 2015. Hydrothermal fluid flow disruptions evidenced by subsurface changes in heat transfer modality: The La Fossa cone of Vulcano (Italy) case study. Geology 43 (11), 959–962. https://doi.org/10.1130/G37015.1.

Román, M.O., Justice, C., Paynter, I., Boucher, P.B., Devadiga, S., Endsley, A., Erb, A., Friedl, M., Gao, H., Giglio, L., Gray, J.M., 2024. Continuity between NASA MODIS collection 6.1 and VIIRS collection 2 land products. Remote Sens. Environ. 302, 113963. https://doi.org/10.1016/j.rse.2023.113963.

Romero, J.E., Burton, M., Cáceres, F., Taddeucci, J., Civico, R., Ricci, T., Pankhurst, M.J., Hernández, P.A., Bonadonna, C., Llewellin, E.W., Pistolesi, M., 2022. The initial phase of the 2021 cumbre Vieja ridge eruption (Canary Islands): products and dynamics controlling edifice growth and collapse. J. Volcanol. Geotherm. Res. 431, 107642. https://doi.org/10.1016/j.jvolgeores.2022.107642.

Roujean, J.-L., et al., 2021. TRISHNA: An Indo-French Space mission to study the thermography of the earth at fine spatio-temporal resolution. In: 2021 IEEE International India Geoscience and Remote Sensing Symposium (InGARSS), Ahmedabad, India, pp. 49–52. https://doi.org/10.1109/InGARSS51564.2021.9791925.

Schowengerdt, R.A., 2007. Remote Sensing: Models and Methods for Image Processing. Academic Press, Burlington, p. 515. https://doi.org/10.1016/B978-0-12-369407-2.X5000-1.

Schroeder, W., Giglio, L., 2017. Visible Infrared Imaging Radiometer Suite (VIIRS) 375 m & 750 m Active Fire Detection Data Sets Based on Nasa VIIRS Land Science Investigator Processing System (SIPS) Reprocessed Data-Version 1. National Aeronautics and Space Administration (NASA). Product User's Guide Version 1.3. Available from: https://lpdaac.usgs.gov/documents/132/VNP14_User_Guide_v1.3.pdf [Last accessed 30 November 2023].

Self, S., Rampino, M.R., 2012. The 1963–1964 eruption of Agung volcano (Bali, Indonesia). Bull. Volcanol. 74 (6), 1521–1536. https://doi.org/10.1007/s00445-012-0615-z.

Selva, J., Bonadonna, C., Branca, S., De Astis, G., Gambino, S., Paonita, A., et al., 2020. Multiple hazards and paths to eruptions: A review of the volcanic system of Vulcano (aeolian islands, Italy). Earth. Sci. Rev. 207, 103186. https://doi.org/10.1016/j.earscirev.2020.103186.

Shreevastava, A., Hulley, G., Thompson, J., 2023. Algorithms for detecting sub-pixel elevated temperature features for the NASA surface biology and geology (SBG) designated observable. J. Geophys. Res. Biogeosci. 128, e2022JG007370. https://doi.org/10.1029/2022JG007370.

Silvestri, M., Rabuffi, F., Pisciotta, A., Musacchio, M., Diliberto, I.S., Spinetti, C., Lombardo, V., Colini, L., Buongiorno, M.F., 2019. Analysis of thermal anomalies in volcanic areas using multiscale and multitemporal monitoring: Vulcano Island test case. Remote Sens. 11, 134. https://doi.org/10.3390/rs11020134.

Small, C., Naumann, T., 2001. The global distribution of human population and recent volcanism. Global Environ. Change B. Environ. Hazard 3 (3), 93–109. https://doi.org/10.3763/ehaz.2001.0309.

Sparks, R.S.J., Biggs, J., Neuberg, J.W., 2012. Monitoring volcanoes. Science 335, 1310–1311. https://doi.org/10.1126/science.1219485.

Steffke, A.M., Harris, A.J., 2011. A review of algorithms for detecting volcanic hot spots in satellite infrared data. Bull. Volcanol. 73, 1109–1137. https://doi.org/10.1007/s00445-011-0487-7.

Surjo, I., 1965. Casualties of the latest activity of the Agung volcano. Bull. Geol. Surv. Indonesia 2 (1), 22–26.

Syafitri, A., et al., 2022. IOP Conf. Ser.: Earth Environ. Sci, 1047 012005. https://doi.org/10.1088/1755-1315/1047/1/012005.

Syahbana, D.K., Kasbani, K., Suantika, G., et al., 2019. The 2017–19 activity at Mount Agung in Bali (Indonesia): intense unrest, monitoring, crisis response, evacuation, and eruption. Sci. Rep. 9, 8848. https://doi.org/10.1038/s41598-019-45295-9.

Tampubolon, T., Yanti, J., Liu, C.Y., 2020. Spatial correlation between land surface properties and cloud characteristics in Indonesia. In: Journal of Physics: Conference Series, 1428, No. 1. IOP Publishing, p. 12044. https://doi.org/10.1088/1742-6596/1428/1/012044.

Tanaka, K., Okamura, Yoshihiko, Amano, Takahiro, Hiramatsu, Masaru, Shiratama, Koichi, 4 November 2010. Operation concept of the second-generation global imager (SGLI). In: Proc. SPIE 7862, Earth Observing Missions and Sensors: Development, Implementation, and Characterization, 786209. https://doi.org/10.1117/12.869398.

Tanaka, K., Okamura, Y., Amano, T., Hosokawa, T., Uchikata, T., 2014. The development status of Second Generation Global Imager (SGLI), Infrared Scanning Radiometer (SGLI-IRS). In: Proc SPIE 9264, Earth Observing Missions and Sensors: Development, Implementation, and Characterization III, 92640G, Beijing, China, 19 Nov 2014. https://doi.org/10.1117/12.2073597.

Taryn, L., Aguilera, Felipe, Tassi, Franco, Moor, J., Bobrowski, Nicole, Aiuppa, Alessandro, Tamburello, Giancarlo, Rizzo, Andrea, Liuzzo, Marco, Viveiros, Fatima, Cardellini, Carlo, Silva, Catarina, Fischer, Tobias, Jean-

Remote Sensing of Environment 315 (2024) 114388

Baptiste, Philippe, Kazayaha, Ryunosuke, Hidalgo, Silvana, Malowany, Kalina, Lucic, Gregor, Bagnato, Emanuela, Chiodini, Giovanni, 2018. New insights into the magmatic-hydrothermal system and volatile budget of Lastarria volcano, Chile: integrated results from the 2014 IAVCEI CCVG 12th Volcanic Gas Workshop. Geosphere 14. https://doi.org/10.1130/GES01495.1.

Thompson, J.O., Ramsey, M.S., 2021. The influence of variable emissivity on lava flow propagation modeling. Bull. Volcanol. 83, 41. https://doi.org/10.1007/s00445-021-01462-3.

Thompson, J.O., Contreras-Arratia, R., Befus, K.S., Ramsey, M.S., 2022. Thermal and seismic precursors to the explosive eruption at La Soufrière Volcano, St. Vincent in April 2021. Earth Planet. Sci. Lett. 592, 117621. https://doi.org/10.1016/j.epsl.2022.117621, 15 August 2022.

Thompson, J.O., Williams, D.B., Ramsey, M.S., 2023. The expectations and prospects for quantitative volcanology in the upcoming Surface Biology and Geology (SBG) era. Earth Space Sci. 10, e2022EA002817. https://doi.org/10.1029/2022EA002817.

Torres-González, P.A., Luengo-Oroz, N., Lamolda, H., D'Alessandro, W., Albert, H., Iribarren, I., Moure-García, D., Soler, V., 2020. Unrest signals after 46 years of quiescence at cumbre vieja, La Palma, Canary Islands. J. Volcanol. Geotherm. Res. 392, 106757. https://doi.org/10.1016/j.jvolgeores.2019.106757.

Torrisi, F., Amato, E., Corradino, C., Del Negro, C., 2022. The FastVRP automatic platform for the thermal monitoring of volcanic activity using VIIRS and SLSTR sensors: FastFRP to monitor volcanic radiative power. Ann. Geophys. 65 (6), RS642. https://doi.org/10.4401/ag-8823.

Tramutoli, V., 1998. Robust AVHRR Techniques (RAT) for environmental monitoring: theory and applications. In: Cecchi, G., Zilioli, E. (Eds.), Earth Surface Remote Sensing, 3496, pp. 101–113. https://doi.org/10.1117/12.332714. Proceedings of SPIE.

Tramutoli, V., 2005. Robust Satellite Techniques (RST) for natural and environmental hazards monitoring and mitigation: Ten year of successful applications. In: Liang, S., Liu, J., Li, X., Liu, R., Schaepman, M. (Eds.), 9th Int. Symp. Phys. Meas. Signatures Remote Sensing, IGSNRR, Beijing, China, XXXVI, pp. 792–795.

Triyono, D., Khomarudin, M.R., 2020, April. Surface temperature changes of the crater of Agung Volcano from Landsat-8 TIRS during 2017-2018 eruption. In: Journal of Physics: Conference Series, 1528, No. 1. IOP Publishing, p. 12052. https://doi.org/10.1088/1742-6596/1528/1/012052.

Tsang, S.W.R., Lindsay, J.M., 2020. Lava flow crises in inhabited areas part I: lessons learned and research gaps related to effusive, basaltic eruptions. J. Appl. Volcanol. 9, 9. https://doi.org/10.1186/s13617-020-00096-y.

Uchôa, J., Viveiros, F., Tiengo, R., Gil, A., 2023. Detection of geothermal anomalies in hydrothermal systems using ASTER data: the Caldeiras da Ribeira Grande case study (Azores, Portugal). Sensors 23, 2258. https://doi.org/10.3390/s23042258.

Urai, M., Pieri, D., 2011a. ASTER Applications in Volcanology. NASA's Earth Observing System and the Science of ASTER and MODIS, Land Remote Sensing and Global Environmental Change, 11. Springer, New York, NY, USA, pp. 245–272. https://doi.org/10.1007/978-1-4419-6749-7_12.

Urai, M., Pieri, D., 2011b. Volcano Observations with ASTER and ASTER Image Database for Volcanoes IEEE International Geoscience and Remote Sensing Symposium, Vancouver, BC, Canada, pp. 3661–3663. https://doi.org/10.1109/IGARSS.2011.6050018.

van Manen, S.M., Dehn, J., West, M.E., Blake, S., Rothery, D.A., 2006. The 2006 eruption of Augustine volcano—combined analyses of thermal satellite data and reduced displacement. The 553–567. https://doi.org/10.3133/pp176923.

Vaughan, R.G., Lowenstern, J.B., Keszthelyi, L.P., Jaworowski, C., Heasler, H., 2012a. Mapping temperature and radiant geothermal heat flux anomalies in the Yellowstone geothermal system using ASTER thermal infrared data. GRC Trans. 36, 1403–1410. https://pubs.usgs.gov/publication/70047415.

Vaughan, R.G., Keszthelyi, L.P., Lowenstern, J.B., Jaworowski, C., Heasler, H., 2012b. Use of ASTER and MODIS thermal infrared data to quantify heat flow and hydrothermal change at Yellowstone National Park. J. Volcanol. Geotherm. Res. 233, 72–89. https://doi.org/10.1016/j.jvolgeores.2012.04.022.

Vaughan, R.G., Hungerford, J.D.G., Keller, W., 2020. A newly emerging thermal area in Yellowstone. Front. Earth Sci. 8, 204. https://doi.org/10.3389/feart.2020.00204.

Verdurme, P., Carn, S., Harris, A.J., Coppola, D., Di Muro, A., Arellano, S., Gurioli, L., 2022. Lava volume from remote sensing data: comparisons with reverse petrological approaches for two types of effusive eruption. Remote Sens. 14 (2), 323. https://doi.org/10.3390/rs14020323.

Vidal, et al., 2022. Optimizing TRISHNA TIR channels configuration for improved land surface temperature and emissivity measurements. Remote Sens. Environ. https://doi.org/10.1016/j.rse.2022.112939.

Wang, Y., Pang, Z., 2023. Heat flux in volcanic and geothermal areas: methods, principles, applications and future directions. Gondwana Res. 122, 260–278. https://doi.org/10.1016/j.gr.2022.09.010.

Way, L., Pritchard, M.E., Wike, L., Reath, K., Gunawan, H., Prambada, O., Syahbana, D., 2022. Detection of thermal features from space at Indonesian volcanoes from 2000 to 2020 using ASTER. J. Volcanol. Geotherm. Res. 430, 107627. https://doi.org/10.1016/j.jvolgeores.2022.107627.

Waythomas, C.F., Haney, M.M., Wallace, K.L., Cameron, C.E., Schneider, D.J., 2017. The 2014 eruptions of Pavlof Volcano, Alaska. US Geol. Surv. Sci. Investig. Rep. 2017-5129, 27. https://doi.org/10.3133/sir20175129.

Werner, C., Kern, C., Coppola, D., Lyons, J.J., Kelly, P.J., Wallace, K.L., Schneider, D.J., Wessels, R.L., 2017. Magmatic degassing, lava dome extrusion, and explosions from Mount Cleveland volcano, Alaska, 2011–2015: insight into the continuous nature of volcanic activity over multi-year timescales. J. Volcanol. Geotherm. Res. 337, 98–110. https://doi.org/10.1016/j.jvolgeores.2017.03.001.

Wittmann, W., Sigmundsson, F., Dumont, S., Lavallée, Y., 2017. Post-emplacement cooling and contraction of lava flows: InSAR observations and a thermal model for lava fields at Hekla volcano, Iceland. J. Geophys. Res. Solid Earth 122, 946–965. https://doi.org/10.1002/2016JB013444.

Wooster, M.J., Zhukov, B., Oertel, D., 2003. Fire radiative energy for quantitative study of biomass burning: derivation from the BIRD experimental satellite and comparison to MODIS fire products. Remote Sens. Environ. 86, 83–107. https://doi.org/10.1016/S0034-4257(03)00070-1.

Worden, A., Dehn, J., Ripepe, M., Delle Donne, D., 2014. Frequency based detection and monitoring of small scale explosive activity by comparing satellite and ground based infrared observations at Stromboli Volcano, Italy. J. Volcanol. Geotherm. Res. 283, 159–171. https://doi.org/10.1016/j.jvolgeores.2014.07.007.

Wright, R., 2016. MODVOLC: 14 years of autonomous observations of effusive volcanism from space. Geol. Soc. Lond., Spec. Publ. 426 (1), 23–53. https://doi.org/10.1144/SP426.12.

Wright, R., Flynn, L.P., 2003. On the retrieval of lava-flow surface temperatures from infrared satellite data. Geology 31 (10), 893–896. https://doi.org/10.1130/G19645.1.

Wright, R., Flynn, L.P., Garbeil, H., Harris, A.J.L., Pilger, E., 2002. Automated volcanic eruption detection using MODIS. Remote Sens. Environ. 82, 135–155. https://doi.org/10.1016/S0034-4257(02)00030-5.

Wright, R., Flynn, L.P., Garbeil, H., Harris, A.J.L., Pilger, E., 2004. MODVOLC: near-real-time thermal monitoring of global volcanism. J. Volcanol. Geotherm. Res. 135, 29–49. https://doi.org/10.1016/j.jvolgeores.2003.12.008.

Wright, R., Garbeil, H., Davies, A.G., 2010. Cooling rate of some active lavas determined using an orbital imaging spectrometer. J. Geophys. Res. Solid Earth 115 (B6). https://doi.org/10.1029/2009JB006536.

Wright, R., Blackett, M., Hill-Butler, C., 2015. Some observations regarding the thermal flux from Earth's erupting volcanoes for the period of 2000 to 2014. Geophys. Res. Lett. 42, 282–289. https://doi.org/10.1002/2014GL061997.

Zakšek, K., Pick, L., Shirzaei, M., Hort, M., 2015. Thermal Monitoring of Volcanic Effusive Activity: The Uncertainties and Outlier Detection. Geological Society, London. https://doi.org/10.1144/sp426.2. Special Publications, (), SP426.2–.

Xiong, X., Oudrari, H., McIntire, J., Lei, N., Chiang, K., Angal, A., 2018. Initial calibration activities and performance assessments of NOAA-20 VIIRS. In: Proceedings of the Earth Observing Missions and Sensors: Development, Implementation, and Characterization V, SPIE Asia-Pacific Remote Sensing, Honolulu, HI, USA, 23 October 2018. https://doi.org/10.1117/12.2326897.

Zakšek, K., Hort, M., Lorenz, E., 2015a. Satellite and ground based thermal observation of the 2014 effusive eruption at Stromboli Volcano. Remote Sens. 7, 17190–17211. https://doi.org/10.3390/rs71215876.

Zen, M.T., Hadikusumo, D., 1964. Preliminary report on the 1963 eruption of Mt. Agung in Bali (Indonesia). Bull. Volcanol. 27, 269–300. https://doi.org/10.1007/BF02597526.

Zhukov, B., Oertel, D., 2001. Hot Spot Detection and Analysis Algorithm for the BIRD Mission. Algorithm Theoretical Basic Document, DLRBerlin.

Zulfakriza, Z., Nugraha, A.D., Widiyantoro, S., Cummins, P.R., Sahara, D.P., Rosalia, S., Priyono, A., Kasbani, K., Syahbana, D.K., Priambodo, I.C., Martanto, M., Ardianto, A., Husni, Y.M., Lesmana, A., Kusumawati, D., Prabowo, B.S., 2020. Tomographic imaging of the Agung-Batur volcano complex, Bali, Indonesia, from the ambient seismic noise field. Front. Earth Sci. 8, 43. https://doi.org/10.3389/feart.2020.00043.